國立臺灣大學電機資訊學院電機工程學系

碩士論文

Department of Electrical Engineering

College of Electrical Engineering and Computer Science

National Taiwan University

Master's Thesis

基於李亞普諾夫之定翼無人機群體控制器與滑動模式風觀測器設計於變動風場環境

Lyapunov-Based Formation Controller with Sliding Mode Wind Observer Design for Fixed-Wing UAV under Variant Wind Field Environment

武敬祥

Ching-Hsiang Wu

指導教授: 連豊力 博士

Advisor: Feng-Li Lian, Ph.D.

中華民國 114 年 2 月

February 2025

doi:10.6342/NTU202500345

國立臺灣大學碩士學位論文
口試委員會審定書

MASTER'S THESIS ACCEPTANCE CERTIFICATE
NATIONAL TAIWAN UNIVERSITY

基於李亞普諾夫之定翼無人機群體控制器與滑動模式風觀測器設計於變動風場環境

Lyapunov-Based Formation Controller with Sliding Mode Wind Observer Design for Fixed-Wing UAV under Variant Wind Field Environment

本論文係武敬祥（學號 R11921080）在國立臺灣大學電機工程學系完成之碩士學位論文，於民國一百一十四年一月十五日承下列考試委員審查通過及口試及格，特此證明。

The undersigned, appointed by the Department of Electrical Engineering on 15 Jan 2025 have examined a Master's thesis entitled above presented by Ching-Hsiang Wu (ID R11921080) candidate and hereby certify that it is worthy of acceptance.

口試委員 Oral examination committee:

連豐力 (指導教授 Advisor) 連豐力

李後燦 李後燦

黃正民 黃正民

江明理 江明理

系主任 Director 李建模 李建模

誌謝

算算在台大待的時間將近八年，相較之下在電機所自控組的時間稍縱即逝，能夠順利完成這一階段的任務要感謝的人事物太多了，族繁不及備載。

首先最要感謝的是指導教授**連豊力**博士，在實驗室人滿為患的時候仍願意收留我。在大學修老師的數位控制時就被老師教學的熱情所感染，進實驗室後老師對研究方法的要求讓我對研究又有了全新的認識。若把兩年的研究生涯當作一門課，並選出學到最重要、有意義的一件事，那肯定是「有所本」，這大概是老師最常說的話，這也改變我過去常憑直覺或印象做事的習慣，在做每一項研究乃至人生的選擇上都能時時審視是否能有所本，也成為我最終能順利完成這篇論文的關鍵。也要謝謝口試委員**李後燦**教授、**黃正民**教授，以及**江明理**教授，在口試時提出的各種建議才能使本篇論文變得更加完整。特別感謝**顏炳郎**教授，在大學時將我領入機器人與自動化的大門，在 RMML 的兩年紮實訓練也奠定了我在機器人領域的基礎，獲益良多。

另外不得不提 **Aiseed** 科技的夥伴們。謝謝 **Joe** 和 **Monica** ，一封信給我機會踏入無人機領域，在新創公司會遇到的各種問題與體驗到的活動也令我大開眼界，原來是有一群人在做這麼酷的事情; 在 Aiseed 實習的經驗也直接影響我整個碩士的研究方向。謝謝 **Ted** ，同高中、同系，後來還變成同事，因為當初我需要在工作時能有個討論的對象才問你要不要來實習，結果真的來了，當時一起做飛機、飛飛機、找飛機的日子真是有趣。謝謝 **Yuri** 、**Sofun** 、**Kayla** 、**Bruce** ，你們在實習中的各種幫助以及建議，無論是在技術或是人生層面上都深深影響著我。

再來要謝謝 **NCS Lab** 的戰友們。謝謝**有田**學長，剛來詢問實驗室時就被學長熱情且詳盡的解說震撼到了，一直到快要畢業的那學期也是多虧學長每天被我巴著問問題才可以讓我快速掌握到呈現與解釋數據的訣竅。謝謝**昱翔**，雖然學長大部分時間都不在實驗室，但是高水準的期刊報告仍是我們的標竿。謝謝**宜儒**，最後一學期的每個周末幸好有你跟我一起當實驗室地頭蛇，每次模擬不順利時看到實驗室同樣有人在戰鬥總能讓我打起精神；也幸虧有你能夠一起扛起每周報的艱鉅任務，分擔火力; 祝你之後的論文發表都能順利。謝謝**瑋恩**，身為唯一一起在春季入學的同梯，雖然你大部分的時間都在工研院，但是在我研究過程遇到瓶頸時，你卻是最常主動來跟我討論我研究上控制的問題，每每能讓我重新整理思緒釐清問題的關鍵。謝謝**凱正**，提供各種有趣的點子與梗圖讓實驗室一直充滿歡笑聲，NCS 無人機組的香火就由你來延續了。謝謝**冠宇**，雖然你不常出現，但也幸好你不常出現，才有你的座位讓我的無人機跟論文有地方放。謝謝**雁丞**與**晁維**，你們兩位讓我學習到身為研究生應該要具備什麼特質: 不斷對事情保持疑問，提出挑戰，找出解答，最重要的是能夠在過程中永遠保持熱情; 當初聽到你們自願多留半年想把研究做得完整，而且也真的都順利上了 IROS ，真的覺得帥呆了，祝你們之後在業界或學術界都能順利。謝謝**旅青**，總是能想出奇妙的活動活絡實驗室氣氛，這樣的創造力一定也是在研究路上不可少的能力，也是因為你還有雁丞晁維等人才讓我覺得投 paper 是件很酷的事情，讓我最終下定決心投稿 ICRA ，祝你之後美國讀博之路順利，期待美國相見。謝謝**芳源**，在畢業之後還被我一直打擾詢問畢業相關的問題，讓我減緩很多畢業焦慮，祝你在新竹生活順利。謝謝**芳緯**，生機系的學弟變學長，能夠在來到一個陌生環境中遇到熟悉的人就是值得感激的事，祝你之後在工研院的生涯能夠順遂、開心。謝謝**昀誠**、**昱彣**、**偉銘**，能夠有機會在實驗室一起度過這段時光真的很開心，希望你們之後的生活都能順利。**祐誠**、**勝凱**、**林靖**，希望你們能手牽手一起努力扛起實驗室招牌; 特別謝謝

祐誠，若沒你坐我後面一直問問題，最後半年的實驗室生活應該會無聊許多。**柏丞**、**銘政**、**冠倫**、**昭宇**，能跟你們一起唱歌真不錯，接下來美洲豹的任務就交給你們了。

最後要感謝**茂愷**以及 **351A** 的各位，讓我在一開始沒有實驗室座位時能收留我; 感謝**翠倫**，有你在的日子很開心，祝你在天上一切安好。感謝我的家人們，可以讓我任性的去做想做的事。感謝**思**，四年來總是無條件支持我，願彼此都能堅持自己想做的事，成為想成為的人。最後的最後，感謝我自己，選擇這條路，且從不後悔; Control is life ，希望自己能繼續秉持有所本的精神，對任何事不妄下定論，對自己不妄自菲薄; 在未來的路上有更多的 Exploitation 和 Exploration ，並透過不斷回授而收斂成更好的自己。

武敬祥 謹致

中華民國一百一十四年二月六日

doi:10.6342/NTU202500345

基於李亞普諾夫之定翼無人機群體控制器與滑動模式風觀測器設計於變動風場環境

研究生: 武敬祥　　指導教授: 連豊力 博士

國立臺灣大學　電機工程學系

摘要

旋翼無人機已被用於台灣的海防，例如海岸線監視和人員救援。但由於任務區域範圍廣，以及台灣海岸週邊強烈的季風，使得旋翼無人機有效執行任務的難度提高。本論文提出使用定翼無人機編隊飛行系統取代旋翼無人機來提高抗風能力和飛行航程。定翼無人機編隊飛行系統可以利用領導無人機 (leader UAV) 的渦流效應來延長飛行範圍。此外，本論文亦提出一風觀測器為編隊飛行系統提供預估風速和加速度的補償，以減輕變動風場的威脅。最後，透過理想的模型在環（MIL）模擬和更真實的軟體在環（SITL）模擬，成功驗證了帶風補償的定翼無人機編隊飛行系統的性能。兩種模擬結果表明，在兩種編隊飛行軌跡的不同風場環境下，透過風補償，編隊誤差可以顯著減少。所提出的系統在 SITL 模擬中的成功整合也顯示了其在實際應用中的可行性。

關鍵字：

定翼無人機、隊形控制、滑動模式觀測器

doi:10.6342/NTU202500345

doi:10.6342/NTU202500345

Lyapunov-Based Formation Controller with Sliding Mode Wind Observer Design for Fixed-Wing UAV under Variant Wind Field Environment

Student: Ching-Hsiang Wu Advisor: Feng-Li Lian, Ph.D.

Department of Electrical Engineering

National Taiwan University

ABSTRACT

In Taiwan, a rotorcraft UAV has been used for coastal defense such as the coastline surveillance and rescue of people. However, a wide-range missions area and the strong monsoon wind around Taiwan make it difficult to execute the missions effectively. This thesis proposes a fixed-wing UAVs formation flight system instead of rotorcraft UAVs to improve wind resistance and flight range. A fixed-wing UAVs formation flight system is expected to utilize the wake vortex effect from the leader UAV to extend the flight range. Additionally, a wind observer is proposed to provide the estimated wind velocity and acceleration compensating for the formation flight system to mitigate the threats posed by the variant wind field. Finally, the performance of the fixed-wing UAVs formation flight system with the wind compensation is successfully validated through an ideal model-in-the-loop (MIL) simulation and a more realistic software-in-the-loop (SITL) simulation. In both simulations, the result shows that the formation error is significantly reduced with the wind compensation under variant wind field environments in two formation flight trajectories. The successful integration of the proposed system with the SITL simulation also indicates the feasibility of real-world applications.

doi:10.6342/NTU202500345

Keywords:

Fixed-Wing UAV, Formation Control, Sliding Mode Observer

doi:10.6342/NTU202500345

CONTENTS

doi:10.6342/NTU202500345

doi:10.6342/NTU202500345

doi:10.6342/NTU202500345

doi:10.6342/NTU202500345

LIST OF FIGURES

doi:10.6342/NTU202500345

doi:10.6342/NTU202500345

doi:10.6342/NTU202500345

doi:10.6342/NTU202500345

LIST OF TABLES

doi:10.6342/NTU202500345

doi:10.6342/NTU202500345

Chapter 1

Introduction

In this chapter, the various applications of UAV and the motivation of this thesis are first mentioned. Then, according to the current problem to the current solutions fo the research scenario, the problem formulation is established. The contributions of the proposed method are then presented. Finally, the organization of the thesis is outlined.

1.1 Motivation

Unmanned aerial vehicle (UAV) has gained increasing attention in recent years due to its potential applications in various fields, such as inspection, delivery, search and rescue, and surveillance and reconnaissance [1: Zhou *et al.* 2020], [2: Shakhatreh *et al.* 2019].

Under the above-mentioned applications, different scenarios have adopted these applications to solve their problems. In agricultural field, the UAV has been used to monitor the growth of crops, provide the irrigation and watershed planning, and help to spray the pesticides [3: Skydio 2024]. In industrial field, to solve the last-mile delivery problem, lots of commercial drone deliveries have emerged by utilizing the properties of flexibility and dexterity of UAVs. They aim to deliver different kinds of household goods such as food, drinks and healthcare products [4: Koetsier 2023], [5: Zipline 2023], [6: Egypt 2023]. In the national defense field, the UAVs are used to fastly and efficiently surveil and reconnoiter the wide-range of naitonal territory, and to deliver the supplies to the soldiers in the battlefield [7: MiTAC 2019]. The relationshiop between the UAVs' applications and the working scenarios are shown in Figure 1.1.

doi:10.6342/NTU202500345

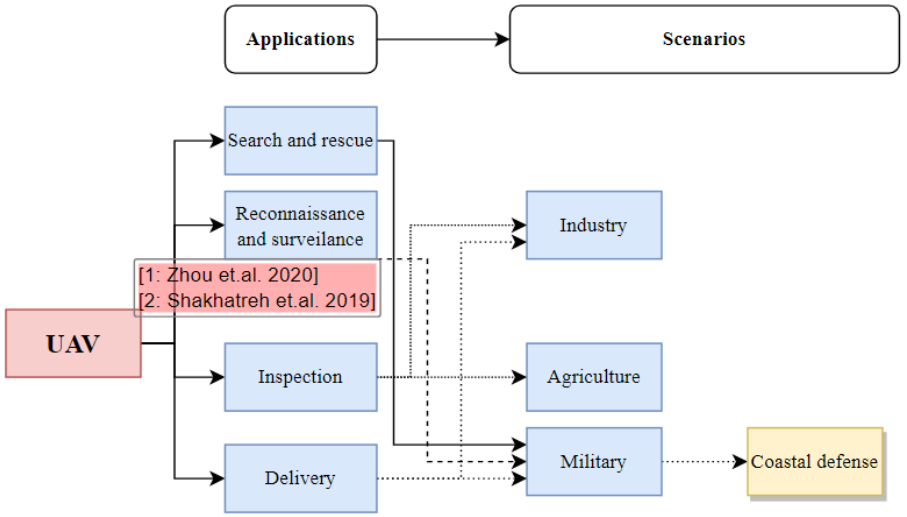

Figure 1.1: The relationship between the UAVs' applications and the working scenarios

In Taiwan, Coast Guard Administration is responsible for guarding the area ranging from up to 300 kilometers away from the coastline, furthermore, the basic-level manpower has declined tremendously since 2013, which has led to the difficulty of efficiently finishing the coast guard missions such as rescuing people from the shipwrecking or hunting down the illegal fishing boat [8: 李文正 2024].To deal with this problem, the rotorcraft UAVs, which is shown in Figure 1.2, has adopted to assist these coast guard missions since 2018 [9: NAO 2023].

Figure 1.2: The rotorcraft UAVs used in the coast guard missions. [9: NAO 2023]

doi:10.6342/NTU202500345

However, according to the report from National Audit Office R.O.C. (Taiwan) in 2023, several problems have been found in the current rotorcraft UAVs system,

- Coast Guard Administration cannot provide enough experienced and professional operators to control the rotorcraft UAVs, which leads to less usage of the UAVs.
- The strong monsoon in Taiwan posed a severe threat to the rotorcraft UAVs, which makes it hard to fly normally through the manuevering of human operators.
- The landing and takoff of the UAVs on the swing and moving ship caused the high risk of the crash of the UAVs.

To tackle the above-mentioned problems, fixed-wing UAV instead of rotorcraft UAVs are proposed to assist the coast guard missions. The fixed-wing UAVs are more suitable for the coast guard missions due to the following reasons. First, In comparison with rotorcraft UAVs, fixed-wing UAVs have the nature advantages such as better wind resistance, high-speed, and lower energy consumption because it can generate lift force by wings through aerodynamics, which also makes it have a larger flight range and longer flight time under a windy wide-range environment [10: Boon *et al.* 2017]. Secondly, study [11: Mirzaeinia *et al.* 2019] shows that fixed-wing forming a close formation flight can reduce the drag force and energy consumption by using the wake vortex induced by the leading UAV. [12: Zhang and Liu 2018] also shows that the energy savings can be up to 30% once the distance between the wingtips of the fixed-wing UAV is maintained at 10% of their wingspan. Furthermore, To deal with the strong monsoon wind influence while flying in formation, a wind estimation method should be proposed to estimate the time-variant wind field, which can be used to compensate the wind influence on the UAV's control system. Lastly, the landing and takeoff of the UAVs on the swing and moving ship can be solved by the pre-

doi:10.6342/NTU202500345

cision landing techniques and autonomous landing and takeoff system, which can make the UAVs system safer without he human operation. Figure 1.3 shows the summary of the proposed solutions and the current problems in the coast guard missions and Figure 1.4 depictes the coast guard working scenario with the proposed solutions.

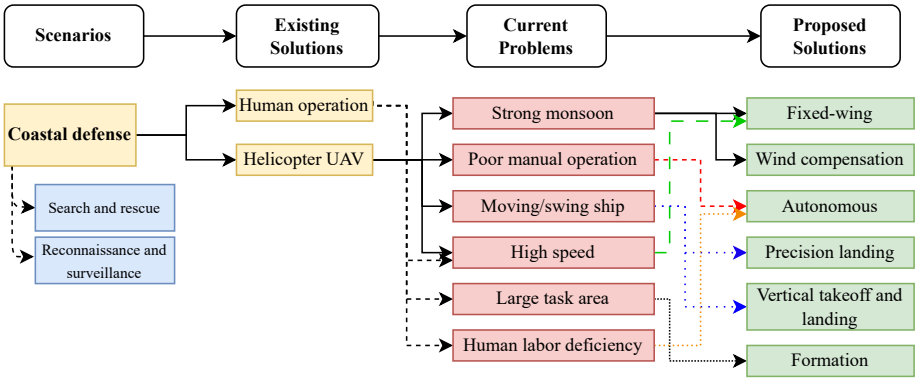

Figure 1.3: The proposed solutions and the current problems in the coast guard missions

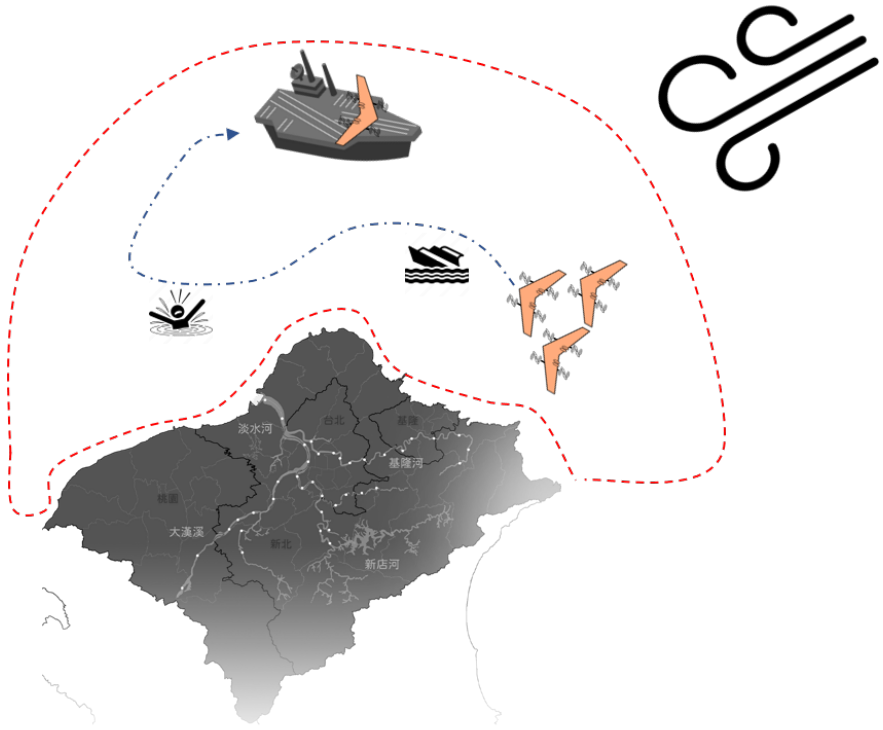

Figure 1.4: Coastal defense missions scenario.

The hybrid UAVs [13: Saeed *et al.* 2018], combine the advantages of the fixed-wing UAVs and the rotorcraft UAVs, have the ability to take off and land vertically like rotorcraft

doi:10.6342/NTU202500345

UAVs and fly in the air like fixed-wing UAVs, which provide more flexiblity to operate in the environment without the long runway - e.g. the deck of the ship, and better flying distance when conducting the surveillance and reconnaissance missions under large area. The close formation flight further lower the energy to extend the flying time and enlarge the working area.

The challenges of the proposed solutions can be divided into several subproblems as follows:

- **Formation control problem:** Maitaining a certain formation configuration of the fixed-wing UAVs to best utilizing the wake vortex from the leader UAV is the main problem to be solved.
- **Wind estimation problem:** The wind pose a severe threat to the UAVs system, especially for the close formation flight system. Designing a efficient and effective wind estimation and compensation method is critical for controlling a fixed-wing to form a close formation under the windy environment.
- **Precision landing problem:** The precision landing problem is to design the precision landing techniques to make the UAVs land vertically on the moving and swinging ship accurately.
- **Path planning problem:** Design a path planning algorithm to make the UAVs fly in the desired suitable path to finish the coast guard reconnaissance missions.
- **Inter-agent collision avoidance problem:** Avoid the collision between the UAVs while forming the close formation flight.

This thesis will focus on the formation control and wind estimation problems of the fixed-

doi:10.6342/NTU202500345

wing UAVs (not consider the vertical takeoff and landing situation) and the others will be left to be future works.

1.2 Problem Formulation

In this thesis, A fixed-wing UAVs formation flight system is proposed to fly under the variant wind field environment. 2 kinds of the formation trajectory are considered, the straight line and the circular orbit, which are shown in Figure 1.5.

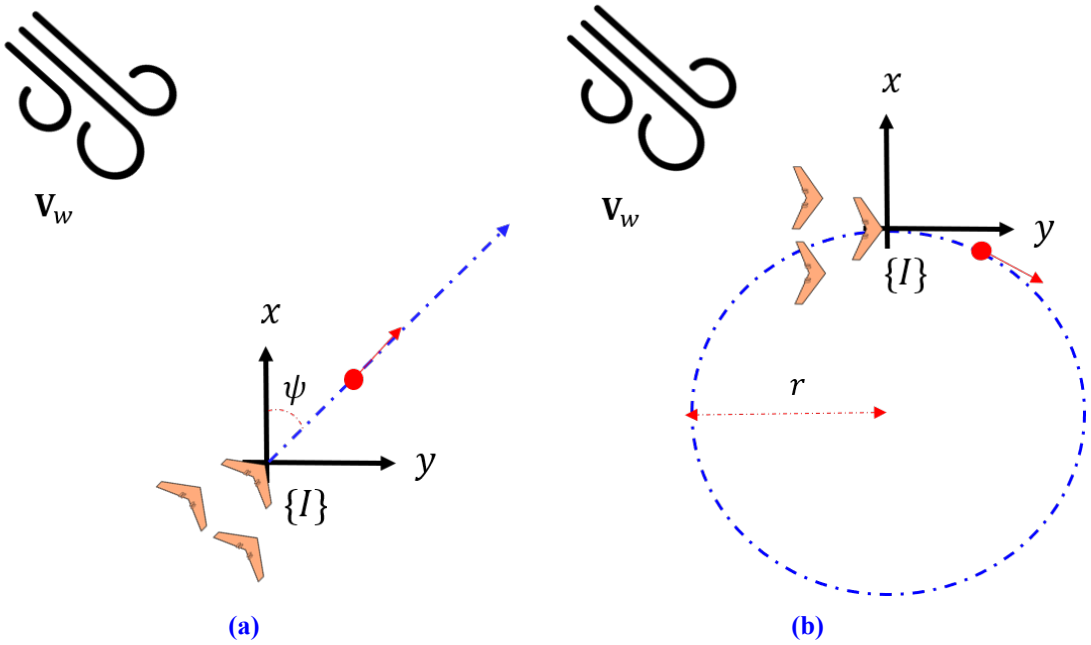

Figure 1.5: The top view of the formation trajectories: (a) straight line, (b) circular orbit. The red dot is the virtual leader UAV, the blue dotted-dashed line is the ideal trajecotry of the leader UAV, and the three fixed-wing UAVs are the follower UAVs.

Each follower UAV tries to maintain a certain distance with the leader UAV to form a formation flight. Through these two formation trajectories, other kinds of trajectory can be decomposed into several pieces of the two basic trajectories [14: Nelson *et al.* 2007] [15: Anderson *et al.* 2005]. The necessary information for this system, such as the 3D position, ground speed, airspeed, attitude and angular velocity, can be obtained from the global positioning system (GPS), pitote tube, and inertial measurement unit (IMU)

doi:10.6342/NTU202500345

sensors. To formulate the proposed system, the following assumptions are first presented:

Assumption 1. The angle of attack (α) and the side-slip angle (β) are assumed to be zero, which means that the UAV airspeed is aligned with the x axis of the UAV body frame.

Assumption 2. Each turn of the UAV is considered as a coordinated turn, which can be expressed as $\dot{\psi} = \frac{g}{V_a} \tan\phi$ [16: Beard and McLain 2012], where ψ represents the heading angle, g is the acceleration of the gravity, and V_a means the airspeed of the UAV.

Assumption 3. An innerloop controller has been existed and responsible for stabilizing the UAVs attitude (ϕ, θ, ψ) and airspeed (V_a).

Assumption 4. The wind magnitude only affects the behavior of the UAVs by the wind triangle [16: Beard and McLain 2012] and not exceeds the physical limitation of the UAVs.

Assumption 5. The maximum pitch angle and flight path angle will not exceed 30 degrees.

Assumption 6. The linear acceleration, angular acceleration and the pitch rate of the leader UAV is zero.

Assumption 7. The desired distance between the leader and the follower will be invariant.

Assumption 8. The wind velocity $\mathbf{V}_w$ is a combination of a constant value and a sinusoidal wave.

The proposed control architecture for the follower UAV is shown in Figure 1.6. From

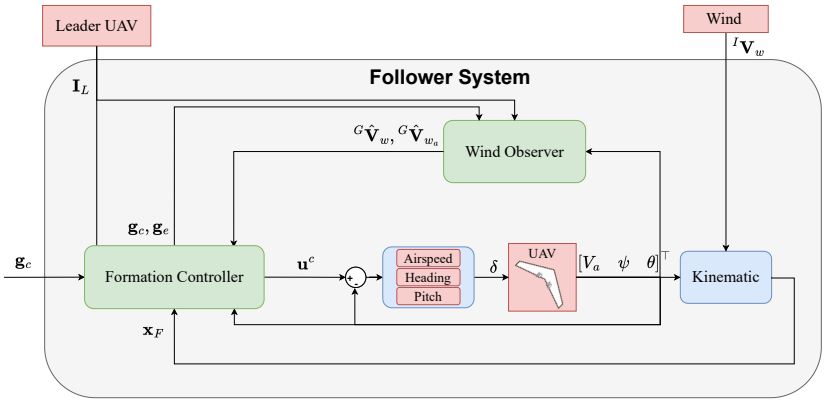

Figure 1.6: The proposed control architecture for the follower UAV system.

doi:10.6342/NTU202500345

Figure 1.6, the control objectives can be briefly stated as : *Given a desired formation configuration,* $\mathbf{g}_c \in \mathbb{R}^3$*, the formation controller will output the control command* $\mathbf{u}^c$ *to the follower UAV such that the formation flight achieved asymptotically even under the variant wind field environment.* The more rigourous control objectives expression will be left to chapter 4.

1.3 Contributions

This thesis aims to solve the fixed-wing UAVs formation flight under variant wind field problems and there are two main contributions to solve the problem in this thesis. The first one is proposing a Lyapunov-based formation controller to stabilize the follower UAVs in the desired formation configuration. The second one is designing a sliding mode wind observer to estimate the time-variant wind velocity and wind acceleration.

1.3.1 Lyapunov-Based Formation Controller

The contributions of the proposed Lyapunov-based formation controller are as follows,

- Compared to the existing works [17: Yu *et al.* 2018], [18: Zhang *et al.* 2021], the proposed controller can not only handle the 2D planar formation but also the 3D space formation case.
- By utilizing the property of the proposed sliding mode wind observer, the proposed controller can achieve the formation flight not only under the constant wind field but also under the variant wind field.
- The cascaded controller structure makes it easier to be combined into the off-the-shelf commercial autopilot,i.e., PX4 Autopilot [19: Meier *et al.* 2015].

doi:10.6342/NTU202500345

1.3.2 Sliding Mode Wind Observer

The contributions of the proposed sliding mode wind observer are as follows,

- Unlike the existing nonlinear sliding mode observer estimates the disturbance in inertial frame [20: Yang *et al.* 2021], the proposed observer estimates the wind velocity and acceleration in the geometry frame by utilizing the first order differentiator [21: Shtessel *et al.* 2014] to better incorporating the esitmations into the formation controller.

1.4 Organization of the Thesis

The rest of this paper is organized as follows. In Chapter 2, existing works about formation control and wind compensation will be discussed. Chapter 3 presents the domain knowledge of the fixed-wing UAVs, simulation, and the sliding mode control and observer theory. The system architecture including the coordinate system definition, the used fixed-wing UAV model and wind model, the formation geometry, and the control objective are illustated on Chapter 4. The detailed proposed Lyapunov-based formation controller and sliding mode wind observer derivations are elaborated on Chapter 5. In Chapter 6, the model-in-the-loop (MIL) simulation and the software-in-the-loop (SITL) simulation is conducted by Matlab/Simulink and PX4 autopilot along with Gazebo sim simulator to evaluate the effectiveness of the proposed controller by RMSE and IAE performance indices. Finally, the conclusion is drawn and the future works are discussed in Chapter 7.

doi:10.6342/NTU202500345

doi:10.6342/NTU202500345

Chapter 2

Literature Survey

In this chapter, the related works of the proposed fixed-wing UAVs formation flight system are comprehensively reviewed. The proposed system can be divided into two main parts: formation control and wind compensation, which are illustrated in Figure 2.1.

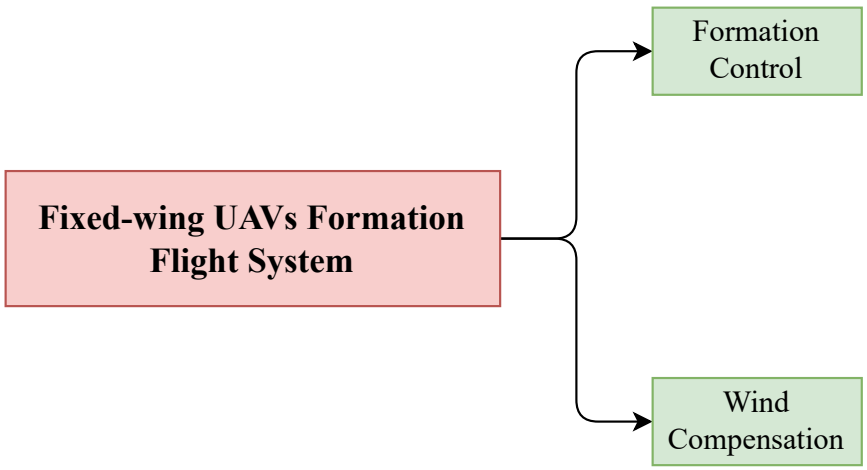

Figure 2.1: The related works of the proposed system

2.1 Formation Control

The UAV formation control problem has been studied for decades, and the comprehensive overview of formation control is illustrated in Figure 2.2. Basically, the formation control problem can be analyzed from three aspects[22: Ouyang *et al.* 2023], [23: Do *et al.* 2021],

- Formation scheme
- Formation mechanism

doi:10.6342/NTU202500345

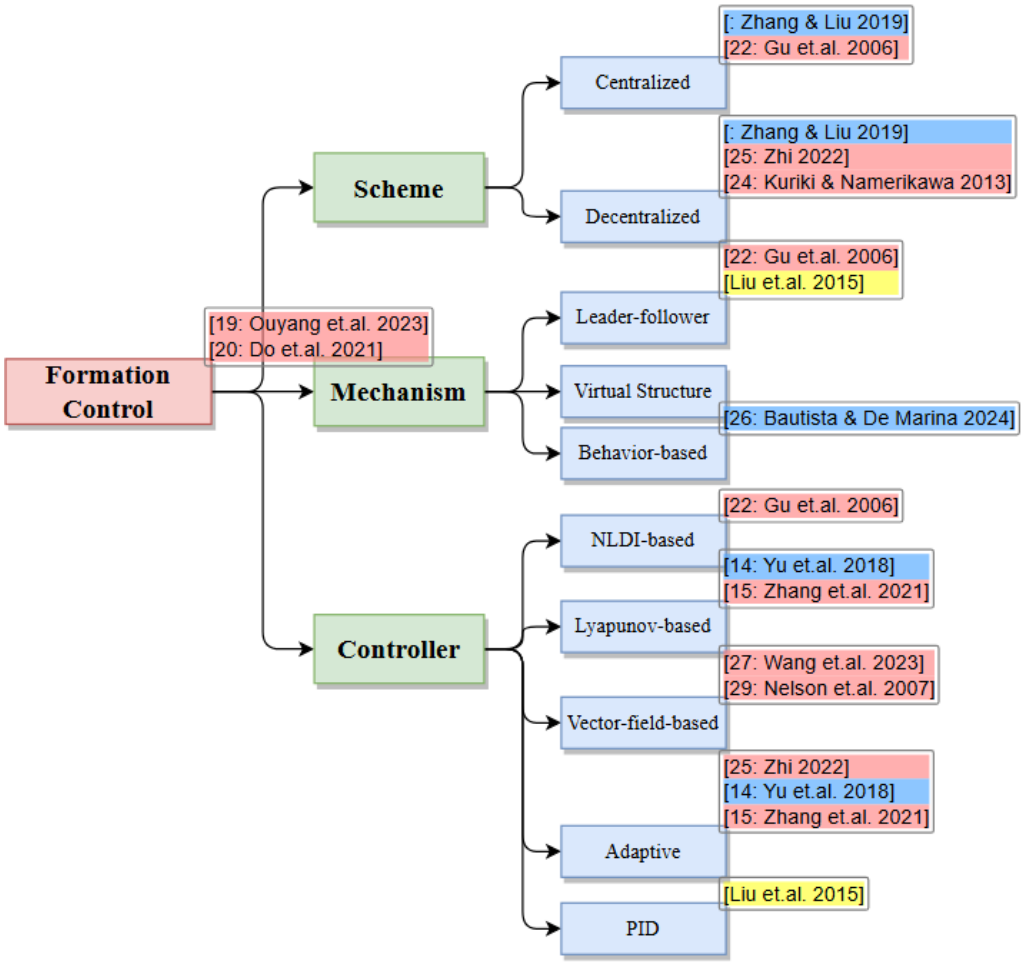

Figure 2.2: Overview of the formation control

doi:10.6342/NTU202500345

- Formation controller design

According to the sharing method of the information or the control signal within team UAVs, the formation scheme can be classified into centralized control [24: Liu *et al.* 2015] [25: Gu *et al.* 2006] and decentralized control [26: Zhang and Liu 2019] [27: Kuriki and Namerikawa 2013] [28: Zhi *et al.* 2022]. In centralized control, the core unit, such as the ground station or a leader UAV, is responsible for collecting the information of all UAVs and calculating the control signal for each UAV. The advantage of the centralized control is easy to implement and with high control performance because it can obtain the global optimization solution, on the other hand, the disadvantage is the formation might be in danger once the core unit fails; in decentralized control, no core unit exists, which means that each UAV is responsible for calculating its own control signal based on the information of its neighbors. The advantage of decentralized control is the robustness and high fault-tolerance cause it can still maintain the formation even if some UAVs are lost, but the disadvantage is the control performance might be worse than the centralized control because it can only obtain the local optimization solution.

Additionally, according to the different control strategy to form a formation, the formation mechanism can be classified into leader-follower, virtual structure, and behavior-based. In leader-follower strategy [25: Gu *et al.* 2006] [24: Liu *et al.* 2015], one UAV will be nominated as a leader and the others are nominated as followers. The control objective is to make the followers to maintain certain distance relative with the leader. In virtual structure strategy, the concept is to fit the physical position of the UAVs into virtual positions [26: Zhang and Liu 2019]. In behavior-based strategy [29: Bautista and De Marina 2024], by designing certain rules, the UAVs will form a certain pattern by following these rules.

doi:10.6342/NTU202500345

Furthermore, Lots of approaches to design the formation controller for fixed-wing UAV have also been proposed in recent years, such as the vector-field-based [30: Wang *et al.* 2023], vision-based [31: Wilson *et al.* 2014], PID control [24: Liu *et al.* 2015], adaptive control [28: Zhi *et al.* 2022], Lyapunov-based [17: Yu *et al.* 2018], [18: Zhang *et al.* 2021],and nonlinear dynamic inversion method [25: Gu *et al.* 2006].

The vector-field is orignally proposed for solving path following problem[14: Nelson *et al.* 2007]. And [30: Wang *et al.* 2023] extend it to solve the fixed-wing formation control problem. A non-uniform vector field, which determines the course angle and the groundspeed meanwhile, along with the leader UAV is designed to guide the follower UAV to the desired position related to the leader. However, this method can only be applied to the 2D formation flight case.

In [24: Liu *et al.* 2015], the faulat tolerance and collision avoidance problems in the formation flight are considered. A classical PID controller is first applied to the outer-loop control, and an extra virtual repulsive force is generated by mechanical impedance principle when two UAVs are too close.

To solve the uncertainty problem while forming the formation flight, the Lyapunov-based controller combined with the adaptive control method to estimate the constant unknown trail vortex effect from the leader UAV is designed in [17: Yu *et al.* 2018] and [18: Zhang *et al.* 2021]. On the other hand, [28: Zhi *et al.* 2022] proposed a distributed robust adaptive controller (DMRRAC) to deal with the formation flight under the parametric uncertainty and bounded disturbances, but the g-load n cannot be controlled in the most off-the-shelf autopilot.

The nonlinear dynamic inversion method (NLDI) is proposed in [25: Gu *et al.* 2006].

doi:10.6342/NTU202500345

By taking second derivative of the formation error equation, the control inputs show up in the error equation and the typical linear control can be applied, however, the wind effect is still not considered in this method.

The summary of all above-mentioned formation controller design methods is shown in Table 2.1.

Table 2.1: Summary of formation controller design methods.

Controller	Dimension	Control Inputs	Drawbacks	References
Vector-field	2D	χ, V_g	No wind consideration, Only 2D	[30: Wang *et al.* 2023]
PID	2D	V_a, ω		[24: Liu *et al.* 2015]
Lyapunov	2D	ψ	No velocity control, Constant wind consideration	[17: Yu *et al.* 2018]
Lyapunov	3D	ψ		[18: Zhang *et al.* 2021]
MRAC	3D	T, ϕ, n	n cannot be controlled in off-the-shelf autopilot	[28: Zhi *et al.* 2022]
NLDI + altitude control	2+1D	ϕ, T	No wind consideration	[25: Gu *et al.* 2006]
Lyapunov	3D	V_a, ψ, θ	-	This thesis

In this thesis, we adopt the centralized leader-follower formation control strategy because we need accurate control performance in terms of the distance between the leader and the follower UAV; the leader can be either a virtual leader or a real leader UAV. Furthermore, based on the works in [17: Yu *et al.* 2018] and [18: Zhang *et al.* 2021], we design a Lyapunov-based formation controller to guarantee the formation flight under 3D space by controlling airspeed (V_a), heading angle (ψ), and pitch angle (θ). The bounded time-variant wind compensation is also considered in the controller design, which will be left to the next section to discuss the wind compensation problem in detail.

2.2 Wind Compensation

doi:10.6342/NTU202500345

At the beginning of this section, the wind compensation problem can be decomposed into two categories, the one is the kinds of the wind field we are facing and another is the methods to estimate the targeted wind field. The overview of the wind compensation problem is illustrated in Figure 2.3.

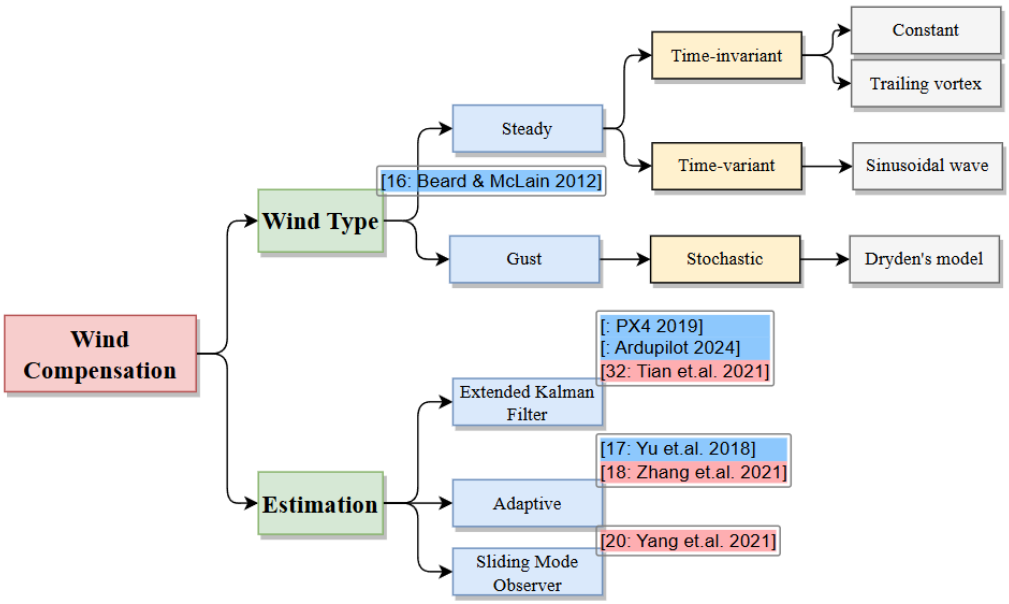

Figure 2.3: Overview of the wind compensation

According to [16: Beard and McLain 2012], the wind field $\mathbf{V}_w$ can represented as follows,

$$\mathbf{V}_w = \mathbf{V}_{w_s} + \mathbf{V}_{w_g}, \tag{2.1}$$

where $\mathbf{V}_{w_s}$ is a steady wind vector representing a time-invariant wind field (e.g., constant wind $\mathbf{V}_{w_{sc}}$) or time-variant wind field (e.g., a sinusoidal wave $\mathbf{V}_{w_{ss}}$). It is worth mentioning that the trailing vortex effect induced from the leader UAV can be formulated by a function of the relative position between leader and follower UAV [12: Zhang and Liu 2018]. As a result, trailing vortex effect can be considered as a time-invariant wind effect. On the other hand, $\mathbf{V}_{w_g}$ is a gust wind vector representing the stochastic wind field (e.g., Dryden's wind model). The Dryden's wind model simulates the stochastic effects when a constant

doi:10.6342/NTU202500345

steady wind pass through the UAV by passing a white noises signal through the Dryden's transfer functions [16: Beard and McLain 2012].

When it comes to estimating the unknown wind field, the extended Kalman filter (EKF) is widely used to estimate the wind velocity in small fixed-wing UAVs [32: Tian *et al.* 2021] and has been incorporated into the open-source autopilot system such as Ardupilot [33: Ardupilot 2024] and PX4 Autopilot [34: PX4 2019]. The merit of using EKF is the ability to handle the uncertain noise.

On the other hand, [17: Yu *et al.* 2018] and [18: Zhang *et al.* 2021] adopt the adaptive control method to estimate the trail vortex effect from the leader UAV. They incorporate the adaptive control formulation into the proposed Lyapunov-based formation controller to guarantee the stability of the formation flight with wind compensation. However, this method only works for estimateing the time-invariant wind field.

As comparison with the adaptive control method, [20: Yang *et al.* 2021] designed a nonlinear sliding mode observer (SMO) to estimate the wind velocity in 3 dimensional space for enhancing the performance of path following under wind disturbances. The property of the sliding mode observer is the finite time convergence when the signal is noise-free and the estimation error would be bounded even if the noise exists [21: Shtessel *et al.* 2014]. This property make it suitable to be applied to estimate the uncertain bounded variant wind field. Table 2.2 summarizes the wind estimation method in the literature.

This thesis adopts the sliding mode observer to estimate the variant wind field as in [20: Yang *et al.* 2021] because SMO has the finite time convergence property and can be generalized in 3D space. The difference is in order to be incorporated into the proposed Lyapunov-based formation controller, the sliding mode observer is designed in geometry

doi:10.6342/NTU202500345

Table 2.2: Summary of wind estimation methods.

Estimation Method	Dimension	Task	Wind Type	References
EKF	2D	Path following	$\mathbf{V}_{w_{sc}}, \mathbf{V}_{w_{ss}}, \mathbf{V}_{w_g}$	[34: PX4 2019] [33: Ardupilot 2024]
Adaptive	2D	Formation flight	$\mathbf{V}_{w_{sc}}$	[17: Yu *et al.* 2018]
Adaptive	3D	Formation flight		[18: Zhang *et al.* 2021]
SMO	3D	Path following	$\mathbf{V}_{w_{sc}}, \mathbf{V}_{w_{ss}}, \mathbf{V}_{w_g}$	[20: Yang *et al.* 2021]
SMO	3D	Formation flight	$\mathbf{V}_{w_{sc}}, \mathbf{V}_{w_{ss}}, \mathbf{V}_{w_g}$	This thesis

frame directly instead of inertial frame.

doi:10.6342/NTU202500345

Chapter 3

Preliminaries

3.1 Basics of Fixed-Wing UAV

This section provides some basic domain knowledges and terminologies about the fixed-wing UAVs.

3.1.1 Coordinate Definitions

There are two coordinate frames that are commonly used in the fixed-wing UAVs: the inertial frame and the body frame [16: Beard and McLain 2012]. The inertial frame follows the North-East-Down (NED) convention, where the basis are $(\mathbf{i}^i, \mathbf{j}^i, \mathbf{k}^i)$ and the origin is located at the home location. The body frame follows the Forward-Right-Down (FRD) convention, where the basis are $(\mathbf{i}^b, \mathbf{j}^b, \mathbf{k}^b)$ and the origin is located at the center of mass of the UAV.

3.1.2 Wind Triangle

The wind traingle is composed of three vectors [16: Beard and McLain 2012]:

- Airspeed vector $(\mathbf{V}_a)$: The UAV volocity with respect to the surrounding air. The airspeed can be divided into indicated airspeed (IAS), calibrated airspeed (CAS), and true airspeed (TAS) [35: AviationHunt 2024]. In this thesis, $\mathbf{V}_a$ means the true airspeed (TAS).
- Ground speed vector $(\mathbf{V}_g)$: The UAV velocity with respect to the inertial frame.

doi:10.6342/NTU202500345

- Wind speed vector $(\mathbf{V}_w)$: The wind velocity with respect to the inertial frame.

The relationship between these three vectors can be expressed as follows (Eqn. (2.6) in [16: Beard and McLain 2012]):

$$\mathbf{V}_g = \mathbf{V}_a + \mathbf{V}_w \tag{3.1}$$

Figure 3.1 visualizes the wind triangle relationship in the 3 dimensional space from the top view and side view.

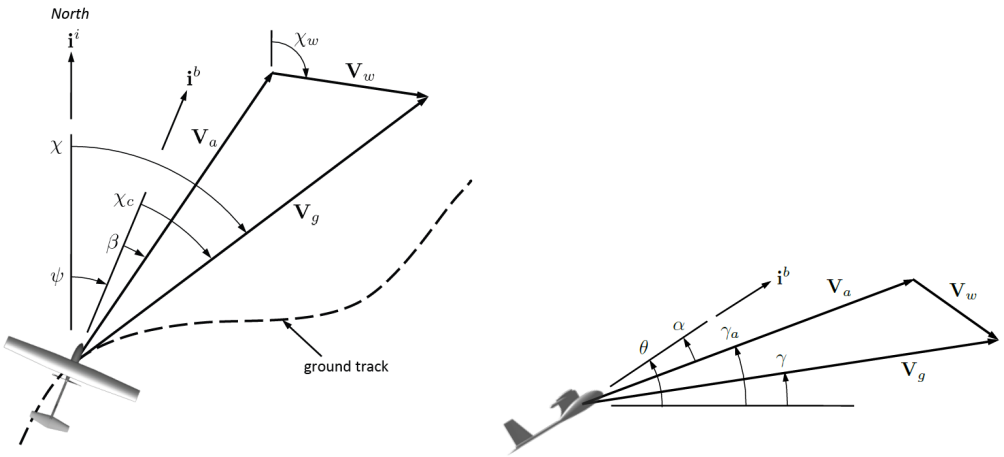

(a) The top view of the wind triangle illustration. **(b) The side view of the wind triangle illustration.**

Figure 3.1: The wind traingle illustration in 3D space [16: Beard and McLain 2012].

In Figure 3.1(a), the ground track is the trajectory where the UAV is following on the ground. Where β is the sideslip angle, which is the angle between the $\mathbf{V}_a$ and the $\mathbf{i}^b - \mathbf{k}^b$ plane, ψ is the heading angle(yaw angle), which is the angle between the $\mathbf{i}^b$ and the $\mathbf{i}^i$, and χ is the course angle, which is the angle between the $\mathbf{i}^i$ and the $\mathbf{V}_g$. The χ_c means the crab angle, which is the difference between the heading angle and the course angle.

In Figure 3.1(b), where α is the angle of attack(AOA), which is used to generate the lift force and defined as the angle between the $\mathbf{V}_a$ and the $\mathbf{i}^b - \mathbf{j}^b$ plane, θ is the pitch angle, which is the angle between the $\mathbf{i}^b$ and the $\mathbf{i}^i - \mathbf{j}^i$ plane, and γ is the flight path angle, which is the angle between the $\mathbf{V}_g$ and the $\mathbf{i}^i - \mathbf{j}^i$ plane. The γ_a means the air-mass flight path

doi:10.6342/NTU202500345

angle, which is the angle between the $\mathbf{V}_a$ and the $\mathbf{i}^i - \mathbf{j}^i$ plane.

Additionally, ϕ, it is not shown in Figure 3.1, is the bank angle (roll angle), which is angle of rotation around the $\mathbf{i}^b$. Under the condition of the absence of the wind, $\mathbf{V}_w = \mathbf{0}$, and Assumption 1, the following relations are trivially established [16: Beard and McLain 2012],

- $\mathbf{V}_g = \mathbf{V}_a$,
- $\chi = \psi$, which means that $\chi_c = 0$,
- $\gamma = \gamma_a = \theta$.

All the fixed-wing UAV's terminologies are summarized in Table 3.1

Table 3.1: The summary of the terminologies used in fixed-wing UAV.

Term	Name	Term	Name
$\mathbf{V}_a$	Airspeed vector	α	Angle of attack
$\mathbf{V}_g$	Ground speed vector	β	Sideslip angle
$\mathbf{V}_w$	Wind speed vector	γ	Flight path angle
ϕ	Bank angle	χ	Course angle
θ	Pitch angle	γ_a	Air-mass flight path angle
ψ	Heading angle	χ_c	Crab angle

3.1.3 Coordinated Turn

When the fixed-wing trying to make a turn, it is intuitive that a strong relation exists between the bank angle, heading angle rate and the turning radius. If the UAV is making a turn without the lateral acceleration in the body frame of the UAV, the UAV is said to be under a coordinated turn (Chapter 5.2 in [16: Beard and McLain 2012]). The free body diagram of the UAV under the coordinated turn with wind effect is shown in Figure 3.2,

During the coordinated turn, the component of the lift force F_{lift} will balance the

doi:10.6342/NTU202500345

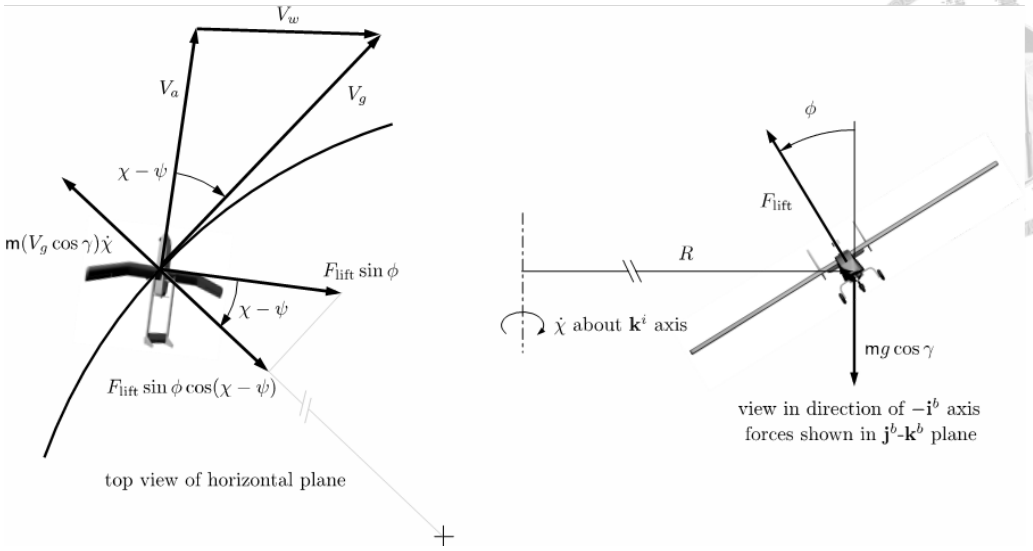

Figure 3.2: The free body diagram of the UAV during the coordinated turn with wind effect [36: Beard 2024]. The left and right figure show the top view and front view, respectively.

centrifugal force and gravitational force g working on the UAV, which can be repsented as [16: Beard and McLain 2012]

$$\begin{aligned} F_{lift} \sin\phi \cos(\chi - \psi) &= m\frac{(V_g \cos\gamma)^2}{R} = m(V_g \cos\gamma)\dot{\chi}, \\ F_{lift} \cos\phi &= mg \cos\gamma, \end{aligned} \tag{3.2}$$

from the Equation (3.2), the course angle rate $\dot{\chi}$ and the turning radius R can be expressed as [16: Beard and McLain 2012]

$$\begin{aligned} \dot{\chi} &= \frac{g}{V_g} \tan\phi \cos(\chi - \psi), \\ R &= \frac{V_g^2 \cos\gamma}{g \tan\phi \cos(\chi - \psi)}. \end{aligned} \tag{3.3}$$

If consider the absence of the wind, the Equation (3.3) can be simplified as a more common expression [16: Beard and McLain 2012]

$$\begin{aligned} \dot{\psi} &= \frac{g}{V_a} \tan\phi, \\ R &= \frac{V_a^2 \cos\gamma}{g \tan\phi}. \end{aligned} \tag{3.4}$$

doi:10.6342/NTU202500345

3.2 Sliding Mode Control/Observer

The modern control, i.e. linear state feedback control, only guarantee the system stability and asymptotical convergence while the extra disturbance is zero [21: Shtessel *et al.* 2014]. One control strategy to handle the bounded disturbances is called *Sliding mode control (SMC)*. The advantage of SMC is not only handling the external bounded disturbances but also providing the finite-time convergence property for system. By applying the concept of SMC, the *Sliding mode observer (SMO)* also provides the same property for the state estimation.

This section, which is constructed by a main reference, [21: Shtessel *et al.* 2014] and my personal understandings, will briefly present the basic knowledges behind the derivation of SMO techniques, including the relative degree, first-order sliding mode, second-order sliding mode, super-twisting controller, and first-order differentiator. The section is

.

3.2.1 Relative Degree

Consider the following system:

$$\begin{aligned} \dot{x} &= a(x,t) + b(x,t)u, \\ \sigma &= \sigma(x,t). \end{aligned} \tag{3.5}$$

Definition 1. [37: MAFarooqi 2022] The relative degree (R.D.) of the system Equation (3.5) is ρ in domain D if

$$\begin{aligned} &L_b L_a^{i-1}\sigma(x,t) = 0, i = 1,2,...,\rho-1, \\ &L_b L_a^{\rho-1}\sigma(x,t) \neq 0, \quad \forall x \in D, \end{aligned} \tag{3.6}$$

doi:10.6342/NTU202500345

where σ is the output and L_a, L_b are the standard *Lie derivative* notations.

In plain words, R.D. is ρ if the control input u does not appear in the $\sigma, \dot{\sigma}, ..., \sigma^{\rho-1}$, and appear in σ^{ρ}. Here gives two examples to elaborate the concepts of R.D.

Example 1. [37: MAFarooqi 2022] Consider the following system:

$$\begin{aligned} \dot{x} &= 2 + u, \\ \sigma &= x. \end{aligned} \tag{3.7}$$

The R.D. is equal to 1 because the control input appear in the first order derivative of σ, i.e. $\dot{\sigma} = \dot{x} = 2 + u$.

Example 1 raise an example about the case of R.D = 1. Next, a special case of non-defined R.D. will be presented.

Example 2. [37: MAFarooqi 2022] Consider the following system:

$$\begin{aligned} \dot{x_1} &= x_1 \\ \dot{x_2} &= x_2 + u \\ \sigma &= x_1 \end{aligned} \tag{3.8}$$

The R.D. is not defined in this sytem because the control input will not appear no matter we do how many time derivaties of the σ, i.e. $\sigma^n = x_1, \forall n \in \mathbb{N}$.

3.2.2 First-Order Sliding Mode

(In [21: Shtessel *et al.* 2014], p.43)The first-order sliding mode is also called the conventional sliding mode or the 1-sliding mode. Consider the following gerneral state-

doi:10.6342/NTU202500345

space system (Eqn. (2.1) in [21: Shtessel *et al.* 2014]):

$$\dot{x} = f(x, u, d), \tag{3.9}$$

where $x \in \mathbb{R}^n$ is the state vector, $u \in \mathbb{R}^m$ is the control input, and $d \in \mathbb{R}^p$ is the bounded disturbances. A sliding surface is defined as (Eqn. (2.2) in [21: Shtessel *et al.* 2014])

$$\mathcal{S} = \{x : \sigma(x) = 0\}, \tag{3.10}$$

where σ is the sliding variable (Definition 1.1 in [21: Shtessel *et al.* 2014]).

Definition 2. (Definition 2.1 in [21: Shtessel *et al.* 2014]) An first-order sliding mode take place on sliding surface $\mathcal{S}$ if $\sigma(x(t)) = 0, \quad \forall t > t_r$, where $t_r \in \mathbb{R}^+$ is the reaching time.

If the control input, u, in the Equation (3.9) is discontinuous, e.g. $u = \text{sign}(x)$, the closed-loop system can be written as (Eqn. (2.3) in [21: Shtessel *et al.* 2014]),

$$\dot{x} = f^c(x, d), \tag{3.11}$$

where f^c is discountinuous with respect to the $x(t)$; therefore, the existence of the unique solution cannot be guaranteed in this closed loop system because the Lipschitz condition [38: Khalil 2002] cannot be applied. As a result, a solution concept called Fillipov's solution [39: Filippov 1988] is used to handle the differential equations with discontinuous right-hand side.

Definition 3. (Definition 1.3 in [21: Shtessel *et al.* 2014]) The control input u that drives the state variable x to the sliding surface $\mathcal{S}$ in finite time t_r, and keeps the state variable on the sliding surface thereafter in the presence of the bounded disturbances d, is called the first-order sliding mode controller.

doi:10.6342/NTU202500345

Example 3. (Eqn. (1.1) in [21: Shtessel *et al.* 2014]) Consider the following 1-dimensional motin of a unit mass system:

$$\begin{cases} \dot{x_1} = x_2 & x_1(0) = x_{10} \\ \dot{x_2} = u + f(x_1, x_2, t) & x_2(0) = x_{20} \end{cases}, \tag{3.12}$$

where u is the control input, x_1, x_2 are the state variables, position and velocity, saperately, and $f(x_1, x_2, t)$ is the bounded disturbances term, i.e., $0 < |f(x_1, x_2, t)| < L$. The control objective is to design a control input, u, and sliding variable, σ, such that the state variable, x_1 and x_2, converge to the sliding surface in finite time and stay on the surface thereafter. The final control input and sliding variable are designed as

$$\begin{aligned} \sigma(x, t) &= x_2 + cx_1, \\ u &= -cx_2 - \rho \text{sign}(\sigma), \end{aligned} \tag{3.13}$$

where c, α and ρ are the positive constants. The effect of the sliding mode controller is shown in the following schematic diagram, Figure 3.3.

Figure 3.3 tells us that no matter where the initial state is, the state variable will converge to the sliding surface in finite time, stay in the sliding surface thereafter and converge to the origin asymptotically.

Theorem 1. The first-order sliding mode only exists iff the relative degree of the system is equal to 1 [41: Perruquetti 2010].

3.2.3 Second-Order Sliding Mode

[21: Shtessel *et al.* 2014] The second-order sliding mode is also called the 2-sliding

doi:10.6342/NTU202500345

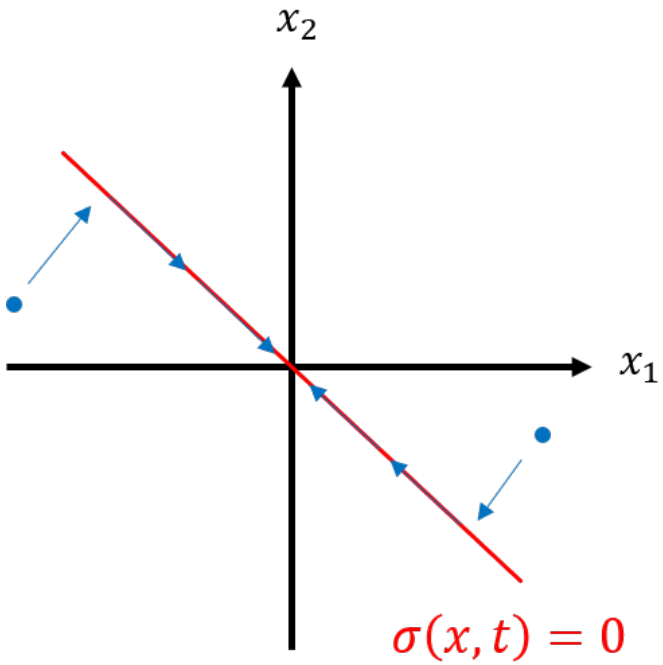

Figure 3.3: The schematic diagram of the close-loop system phase portrait. The blue dot means the initial state, the red line represents the sliding surface, and the blue arrow shows the phase portraits [40: MAFarooqi 2023].

mode. Consider the following system:

$$\begin{aligned} \dot{x} &= a(t,x) + b(t,x)u, \\ \sigma &= \sigma(t,x), \end{aligned} \tag{3.14}$$

where $x \in \mathbb{R}^n$ is the state variables, $u \in \mathbb{R}$ is the control input, and σ is the measured output. Provided that the R.D. of the system Equation (3.14) is equal to 2, then the second time derivative of the output function $\sigma(x,t)$ is

$$\ddot{\sigma} = h(x,t) + g(x,t)u, \tag{3.15}$$

where $h(x,t)$ and $g(x,t)$ are the smooth functions. Suppose that the following inequalities hold globally (Eqn. (4.10) in [21: Shtessel *et al.* 2014]):

$$0 < K_m \leq g \leq K_M, |h| \leq C, \tag{3.16}$$

doi:10.6342/NTU202500345

where K_m, K_M, C are the positive constants. Equation (3.16) implies the following differential inclusion (Eqn. (4.11) in [21: Shtessel *et al.* 2014]):

$$\ddot{\sigma} \in [-C, C] + [K_m, K_M]u. \tag{3.17}$$

Definition 4. (Definition 4.1 in [21: Shtessel *et al.* 2014]) Consider a discontinuous differential equation, $\dot{x} = f(x)$ with a smooth ouput function, $\sigma = \sigma(x)$, and let the diffential equation be in the Filippov sense. Assumed that:

1. σ and the time derivative $\dot{\sigma} = \sigma_x^{'}(x)f(x)$ are continuous functions of x.
2. The set $\sigma = \dot{\sigma} = 0$ is a nonempty integral set.
3. The Filippov set of admissible velocities at the set $\sigma = \dot{\sigma} = 0$ contains more than one vector.

A second-order sliding mode takes place on the set $\sigma = \dot{\sigma} = 0$ and the set is called a 2-sliding set.

The third point means that the set $\sigma = \dot{\sigma} = 0$ is a discontinuous set. That 2-sliding mode can be illustrated in Figure 3.4.

Definition 5. [21: Shtessel *et al.* 2014] The control input $u = \phi(\sigma, \dot{\sigma})$, that drives all the trajectories to the set $\sigma = \dot{\sigma} = 0$ in finite time t_r, and keeps the trajectories on the set thereafter is called the second-order sliding mode controller.

3.2.4 Super-Twisting Controller

doi:10.6342/NTU202500345

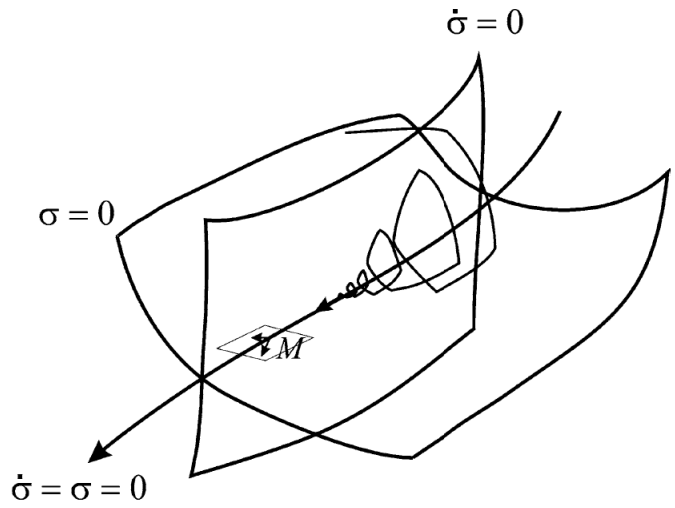

Figure 3.4: The schematic diagram of the 2-sliding mode. M is a point on the 2-sliding mode, and the two vectors on the M represents the 2 velocities in the Filippov set at the set $\dot{\sigma} = \sigma = 0$ (Fig. 4.2 in [21: Shtessel *et al.* 2014]).

Unlike the twisting controller (Chaper 4.2.1 in [21: Shtessel *et al.* 2014]), the super-twisting controller is a second-order sliding mode controller only requiring the dynamic system of relative degree 1. Reconsider the system Equation (3.14), which has R.D. equal to 1; then the first time derivative of the output function $\sigma(x,t)$ is (Eqn. (4.34) in [21: Shtessel *et al.* 2014])

$$\dot{\sigma} = h(x,t) + g(x,t)u. \tag{3.18}$$

Assume that the following inequalities hold (Eqn. (4.35) in [21: Shtessel *et al.* 2014]):

$$0 < K_m \leq g \leq K_M, \quad |\dot{h}| + U_M|\dot{g}| \leq C, \quad |\frac{h}{g}| \leq qU_M, \quad 0 < q < 1, \tag{3.19}$$

for some positive constants K_m, K_M, C, U_M, q. A super-twisting controller is defined as

$$u = -\lambda|\sigma|^{\frac{1}{2}}\text{sign}(\sigma) + u_1, \quad \dot{u_1} = \begin{cases} -u, & |u| > U_M \\ -\alpha\text{sign}(\sigma), & |u| \leq U_M \end{cases} \tag{3.20}$$

doi:10.6342/NTU202500345

Theorem 2. (Theorem 4.5 in [21: Shtessel *et al.* 2014]) With $K_m\alpha > C$ and λ large enough, the super-twisting controller Equation (3.20) guarantees a 2-sliding mode in finite time t_r. The control input u enters the segment $[-U_M, U_m]$ and stays there for all time $t > t_r$.

Remark 1. (Remark 4.5 in [21: Shtessel *et al.* 2014]) The super-twisitng controller Equation (3.20) does not need $\dot{\sigma}$ measurement.

A schematic to illustrate the super-twisting controller phase portrait are shown in Figure 3.5.

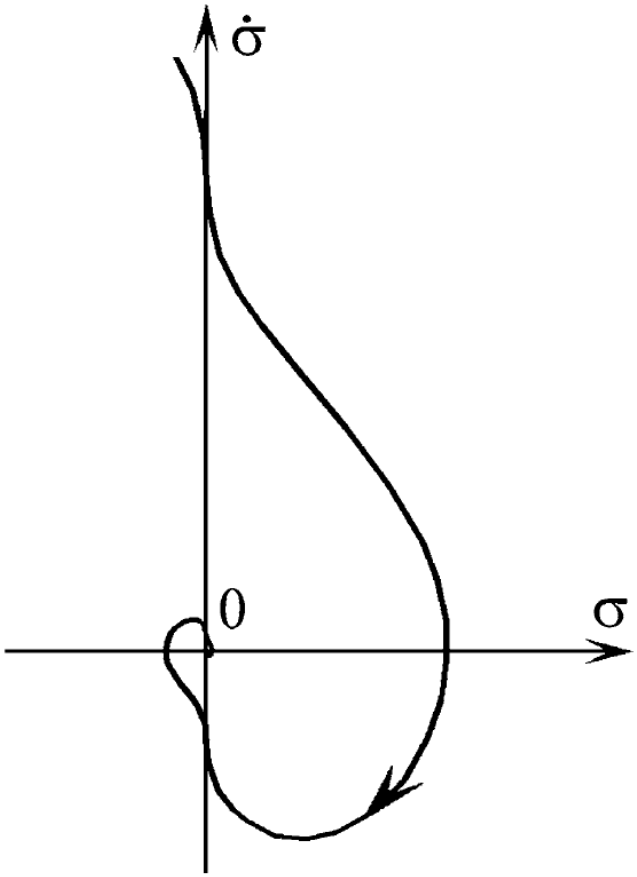

Figure 3.5: The schematic diagram of the super-twisting controller phase portrait (Fig. 4.8 in [21: Shtessel *et al.* 2014]).

3.2.5 First-Order Differentiator

doi:10.6342/NTU202500345

(Chapter 4.3.2 in [21: Shtessel *et al.* 2014]) A differentiator is also called an observer. Consider an input signal $f(t)$ consisting of a bounded measurable noise and an unknown base signal $f_0(t)$ where $\dot{f}_0(t)$ has a known global Lipschitz constant $L > 0$. The problem is to find the estimations of $f_0(t)$ and $\dot{f}_0(t)$ when the noise is absent. To obtain the estimations, consider the following auxiliary system:

$$\dot{z}_0 = \nu, \tag{3.21}$$

where ν is the control input. Let the output function be

$$\sigma_0 = z_0 - f_0(t), \tag{3.22}$$

and the first order derivative of the output function is [21: Shtessel *et al.* 2014]

$$\dot{\sigma}_0 = -\dot{f}_0(t) + \nu, \quad |\ddot{f}_0| \leq L. \tag{3.23}$$

Obviously, the R.D. of the system Equation (3.21) is 1 because the control input ν shows up in the Equation (3.23). The problem becomes designing a 2-sliding mode controller to keep a system Equation (3.21) with R.D. equals 1 in a 2-sliding mode, i.e., $\sigma_0 = \dot{\sigma}_0 = 0$, which also means that the following equations will be held:

$$\begin{aligned} f_0(t) &= z_0, \\ \dot{f}_0(t) &= \nu. \end{aligned} \tag{3.24}$$

A super-twisting controller mentioned in Section 3.2.4 can be applied here and the first

doi:10.6342/NTU202500345

order differentiator is designed as (Eqn. (4.39) in [21: Shtessel *et al.* 2014])

$$\begin{aligned} \nu &= -\lambda_1 |\sigma_0|^{\frac{1}{2}} \text{sign}(\sigma_0) + z_1, \\ \dot{z}_1 &= -\lambda_0 \text{sign}(\sigma_0), \end{aligned} \tag{3.25}$$

where ν and z_1 can be taken as the differentiator outputs.

Theorem 3. (Theorem 4.6 in [21: Shtessel *et al.* 2014]) If the noises are absent for any $\lambda_0 > L$ and for any λ_1 large enough, z_0 converges to $f_0(t)$ and ν converges to $\dot{f}_0(t)$ in finite time.

For satifying Theorem 3, the following two choices of the λ_0 and λ_1 are valid ([21: Shtessel *et al.* 2014], p. 161):

$$\begin{cases} \lambda_0 = 1.1L \\ \lambda_1 = 1.5L^{\frac{1}{2}} \end{cases} \quad \text{and} \quad \begin{cases} \lambda_0 = 2L \\ \lambda_1 = L^{\frac{1}{2}} \end{cases}. \tag{3.26}$$

Theorem 4. (Theorem 4.7 in [21: Shtessel *et al.* 2014]) Let the noises satisfy the inequality $|f(t) - f_0(t)| \leq \epsilon$, where ϵ is a positive constant. Then, the estimation errors will be bounded in the finite time for positive constants μ_1 and μ_2, i.e.,

$$\begin{aligned} |z_0 - f_0(t)| &\leq \mu_1 \epsilon, \\ |\nu - \dot{f}_0(t)| &\leq \mu_2 \epsilon^{\frac{1}{2}}. \end{aligned} \tag{3.27}$$

doi:10.6342/NTU202500345

Chapter 4

System Overview

In this chapter, the coordinate system used in this thesis will be first presented, then the fixed-wing UAV model, wind model, the formation geometry and the error dynamics will be presented under these coordinate systems.

4.1 Coordinate System

The coordinate systems used in this thesis are shown in Figure 4.1.

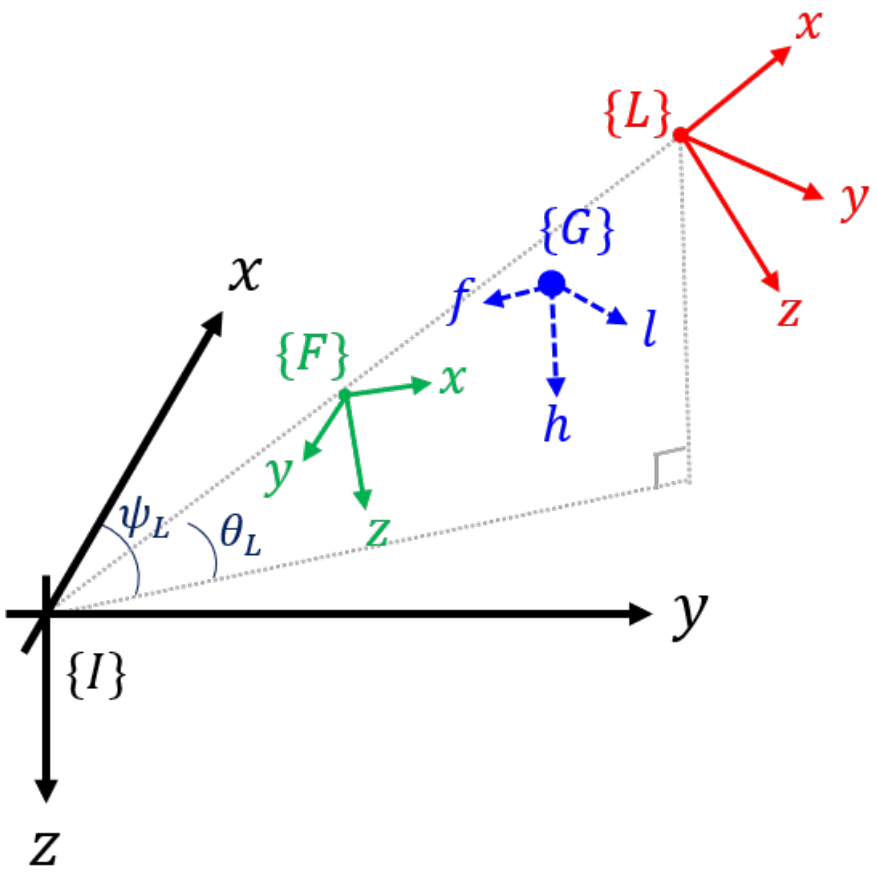

Figure 4.1: The coordinate system of inertial frame $\{I\}$, geometry frame $\{G\}$, leader's and follower's body frame $\{L\}$ and $\{F\}$.

The $\{I\}$ represents the inertial frame, which follows the North-East-Down (NED)

doi:10.6342/NTU202500345

convention, and the $\{L\}$ and $\{F\}$ represent leader's and follower's body frame, respectively, which follow the front-right-down (FRD) convention. The body frame of the UAV is shown in Figure 4.2. The $\{G\}$ is the geometry frame, where the formation geometry will be defined in this frame and the origin of the geometry frame represents the desired formation position for the follower UAV. It is worth mentioning that although the l axis of the $\{G\}$ is parallel to the y axis of the $\{L\}$, the h axis of the $\{G\}$ is parallel to the z axis of the $\{I\}$ instead. The transformation between the $\{I\}$, $\{G\}$, and $\{L\}$ can be represented as follows:

$$\begin{aligned} {}^{I}_{L}\mathbf{R} &= \mathbf{R}_z(\psi_L)\mathbf{R}_y(\theta_L)\mathbf{R}_x(\phi_L), \\ {}^{I}_{G}\mathbf{R} &= \mathbf{R}_z(\psi_L)\mathbf{R}_z(\frac{\pi}{2}) = \mathbf{R}_z(\frac{\pi}{2} + \psi_L), \end{aligned} \tag{4.1}$$

where ${}^{I}_{L}\mathbf{R}$ and ${}^{I}_{G}\mathbf{R}$ are the rotation matrix between $\{I\}$, $\{L\}$, and $\{I\}$, $\{G\}$. The $\mathbf{R}_x$, $\mathbf{R}_y$, and $\mathbf{R}_z$ represent the rotation matrix around the x, y, and z axis, respectively.

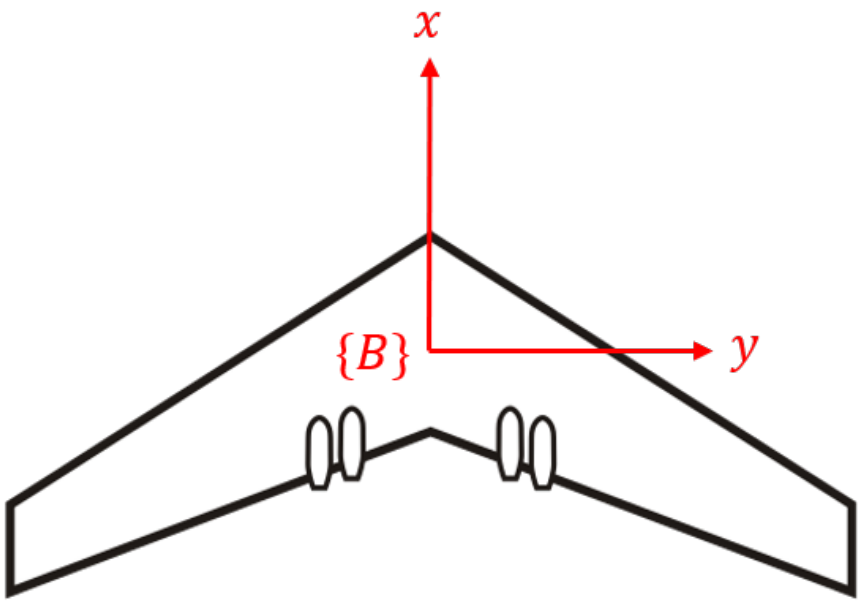

Figure 4.2: The top view of the UAV body frame $\{B\}$.

doi:10.6342/NTU202500345

4.2 Wind Model

From the wind field definition in Equation (2.1), the wind model in frame $\{I\}$ can be modified as

$$
\begin{aligned}
{}^{I}\mathbf{V}_{w} = \begin{bmatrix} w_x \\ w_y \\ w_z \end{bmatrix} &= {}^{I}\mathbf{V}_{w_s} + {}^{I}\mathbf{V}_{w_g} \\
&= {}^{I}\mathbf{V}_{w_{sc}} + {}^{I}\mathbf{V}_{w_{ss}} + {}^{I}\mathbf{V}_{w_g},
\end{aligned}
\tag{4.2}
$$

where ${}^{I}\mathbf{V}_{w_{sc}}$ and ${}^{I}\mathbf{V}_{w_{ss}}$ are the constant and sinusoidal steady wind velocity, respectively. In this thesis, although the wind is spawned in inertial frame $\{I\}$, the proposed formation controller and wind observer will be designed in the geometry frame $\{G\}$. The Equation (4.2) can be transformed into the geometry frame by using the rotation matrix in Equation (4.1) and becomes

$$
{}^{G}\mathbf{V}_{w} = \begin{bmatrix} w_l \\ w_f \\ w_h \end{bmatrix} = {}^{G}_{I}\mathbf{R}\,{}^{I}\mathbf{V}_{w}. \tag{4.3}
$$

4.3 Fixed-Wing UAV Model

The fixed-wing UAV kinematic model described in $\{I\}$ can be represented as follows (Eqn. (2.10) in [16: Beard and McLain 2012]):

$$
\begin{cases}
\dot{x} = V_g \cos\chi \cos\gamma \\
\dot{y} = V_g \sin\chi \cos\gamma \\
\dot{z} = -V_g \sin\gamma
\end{cases}, \tag{4.4}
$$

where x, y, and z denote the position of the UAV, V_g represents the ground speed, χ is the

doi:10.6342/NTU202500345

course angle, and γ is the flight path angle. According to the wind triangle from Equation (3.1), Equation (4.4) can be rewritten as follows:

$$\begin{cases} \dot{x} = V_a \cos\psi \cos\theta + w_x \\ \dot{y} = V_a \sin\psi \cos\theta + w_y \\ \dot{z} = -V_a \sin\theta + w_z \end{cases}, \tag{4.5}$$

where θ is the pitch angle of the UAV, w_x, w_y, and w_z are the wind velocity along the three axes. In this thesis, with the Assumption 3, a workable and robust innerloop controller has been existed and V_a, ψ, and θ hold loop systems are assumed to be first order systems as shown in Equation (4.6) [30: Wang *et al.* 2023]

$$\begin{cases} \dot{V}_a = \tau_{V_a}(V_a^c - V_a) \\ \dot{\psi} = \tau_{\psi}(\psi^c - \psi) \\ \dot{\theta} = \tau_{\theta}(\theta^c - \theta) \end{cases}, \tag{4.6}$$

where V_a^c, ψ^c, and θ^c are airspeed, heading angle, and pitch angle command of the UAV. τ_{V_a}, τ_{ψ}, and τ_{θ} are inverse time constant of the V_a, ψ, and θ hold loop systems, respectively.

4.4 Formation Geometry

In this section, the subscript L and F are first denoted as the symbol of the leader's and the follower's UAV. The relative position and the desired position between a follower and a leader can be described by the formation geometry, which is shown in Figure 4.3.

Where $\mathbf{V} \in \mathbb{R}^3$ are the ground speed vector, $\mathbf{V}_a \in \mathbb{R}^3$ is the airspeed vector, and $\mathbf{V}_w \in \mathbb{R}^3$ is the wind speed vector. It is obvious to see that these three vectors constructed the wind triangle; $\mathbf{p}$ represents the UAV position; (l_e, f_e, h_e) are the forward, lateral, and vertical formation error and (l_c, f_c, h_c) are the desired forward, lateral, and vertical dis-

doi:10.6342/NTU202500345

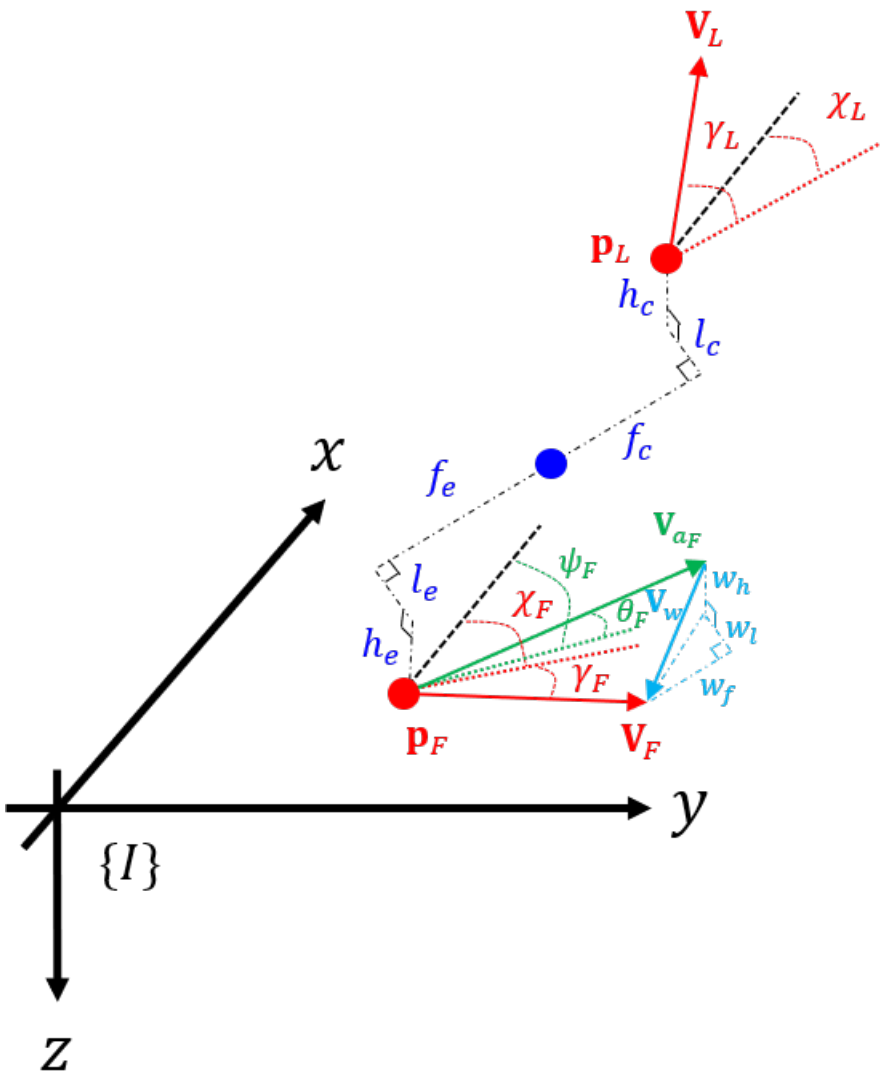

Figure 4.3: The 3-dimensional formation geometry. The blue dot shows the desired formation position for the follower UAV.

doi:10.6342/NTU202500345

tance relative to the leader. From Figure 4.3, the formation error can also be represented as following equation [17: Yu *et al.* 2018], [25: Gu *et al.* 2006],

$$\begin{bmatrix} l_e \\ f_e \\ h_e \end{bmatrix} = \begin{bmatrix} \sin\chi_L & -\cos\chi_L & 0 \\ \cos\chi_L & \sin\chi_L & 0 \\ 0 & 0 & -1 \end{bmatrix} \begin{bmatrix} x_L - x_F \\ y_L - y_F \\ z_L - z_F \end{bmatrix} - \begin{bmatrix} l_c \\ f_c \\ h_c \end{bmatrix} , \tag{4.7}$$

then the formation error dynamics $\dot{l}_e$, $\dot{f}_e$ and $\dot{h}_e$ can be derived by taking the time derivative of Equation (4.7). The derivation is conducted below,

for $\dot{l}_e$:

$$\begin{aligned} l_e &= (x_L - x_F)\sin\chi_L - (y_L - y_F)\cos\chi_L - l_c \\ &\Downarrow \\ \dot{l}_e &= (\dot{x}_L - \dot{x}_F)\sin\chi_L + (x_L - x_F)\dot{\chi}_L\cos\chi_L - (\dot{y}_L - \dot{y}_F)\cos\chi_L + (y_L - y_F)\dot{\chi}_L\sin\chi_L - \dot{l}_c \\ &= (V_{Lx} - V_{Fx})\sin\chi_L - (V_{Ly} - V_{Fy})\cos\chi_L + \dot{\chi}_L\left[(x_L - x_F)\cos\chi_L + (y_L - y_F)\sin\chi_L\right] , \\ &= V_L\cos\chi_L\sin\chi_L\cos\gamma_L - V_F\cos\chi_F\sin\chi_L\cos\gamma_F - V_L\sin\chi_L\cos\chi_L\cos\gamma_L \\ &\quad + V_F\sin\chi_F\cos\chi_L\cos\gamma_F + \dot{\chi}_L(f_e + f_c) \\ &= V_F\sin(\chi_F - \chi_L)\cos\gamma_F + \dot{\chi}_L(f_e + f_c) \end{aligned} \tag{4.8}$$

doi:10.6342/NTU202500345

for $\dot{f}_e$:

$$
\begin{aligned}
f_e &= (x_L - x_F)\cos\chi_L + (y_L - y_F)\sin\chi_L - f_c \\
&\Downarrow \\
\dot{f}_e &= (\dot{x}_L - \dot{x}_F)\cos\chi_L - (x_L - x_F)\dot{\chi}_L\sin\chi_L + (\dot{y}_L - \dot{y}_F)\sin\chi_L + (y_L - y_F)\dot{\chi}_L\cos\chi_L - \dot{f}_c \\
&= (V_{Lx} - V_{Fx})\cos\chi_L + (V_{Ly} - V_{Fy})\sin\chi_L - \dot{\chi}_L\left[(x_L - x_F)\sin\chi_L - (y_L - y_F)\cos\chi_L\right] \\
&= V_L\cos\chi_L\cos\chi_L\cos\gamma_L - V_F\cos\chi_F\cos\chi_L\cos\gamma_F + V_L\sin\chi_L\sin\chi_L\cos\gamma_L \\
&\quad - V_F\sin\chi_F\sin\chi_L\cos\gamma_F - \dot{\chi}_L(l_e + l_c) \\
&= V_L\cos\gamma_L - V_F\cos(\chi_F - \chi_L)\cos\gamma_F + \dot{\chi}_L(-l_e - l_c)
\end{aligned}
\tag{4.9}
$$

for $\dot{h}_e$:

$$
\begin{aligned}
h_e &= -(z_L - z_F) - h_c \\
&\Downarrow \\
\dot{h}_e &= -\dot{z}_L + \dot{z}_F - \dot{h}_c \\
&= V_L\sin\gamma_L - V_F\sin\gamma_F
\end{aligned}
\quad , \tag{4.10}
$$

where $\dot{l}_c$, $\dot{f}_c$, and $\dot{h}_c$ are equal to zero based on Assumption 7. V_x and V_y are the ground speed components along with the x and y axis in $\{I\}$. The overall formation error dynamics is expressed in Equation (4.11).

$$
\begin{bmatrix} \dot{l}_e \\ \dot{f}_e \\ \dot{h}_e \end{bmatrix} = \begin{bmatrix} V_F\sin(\chi_F - \chi_L)\cos\gamma_F \\ V_L\cos\gamma_L - V_F\cos(\chi_F - \chi_L)\cos\gamma_F \\ V_L\sin\gamma_L - V_F\sin\gamma_F \end{bmatrix} + \dot{\chi}_L \begin{bmatrix} f_e + f_c \\ -l_e - l_c \\ 0 \end{bmatrix} . \tag{4.11}
$$

Based on the Assumption 5, $\cos\gamma_F \approx 1$ and $\cos\gamma_L \approx 1$ can be considered and discarded in the later equation. Then the wind triangle is applied to Equation (4.11) and Equation

doi:10.6342/NTU202500345

(4.11) becomes

$$\begin{bmatrix} \dot{l}_e \\ \dot{f}_e \\ \dot{h}_e \end{bmatrix} = \begin{bmatrix} V_{aF}\sin(\psi_F - \chi_L) \\ V_L - V_{aF}\cos(\psi_F - \chi_L) \\ V_L \sin\gamma_L - V_{aF}\sin\theta_F \end{bmatrix} + \dot{\chi}_L \begin{bmatrix} f_e + f_c \\ -l_e - l_c \\ 0 \end{bmatrix} + \begin{bmatrix} w_l \\ w_f \\ w_h \end{bmatrix}. \tag{4.12}$$

4.5 Control Objective

The more rigorous control objective can be reiterated as : *Given a desired formation configuration,* $\mathbf{g}_c := \begin{bmatrix} l_c & f_c & h_c \end{bmatrix}^\top \in \mathbb{R}^3$*, the formation controller will output the control command,* $\mathbf{u}^c := \begin{bmatrix} V_a^c & \psi^c & \theta^c \end{bmatrix}^\top \in \mathbb{R}^3$ *to the follower UAV such that the formation error,* $\mathbf{g}_e := \begin{bmatrix} l_e & f_e & h_e \end{bmatrix}^\top \in \mathbb{R}^3$ *converge to zero asymptotically even under the variant wind field* ${}^I\mathbf{V}_w$. That is to say,

$$\lim_{t\to\infty} \mathbf{g}_e(t) \to \mathbf{0}. \tag{4.13}$$

The control architecture of the proposed follower system is shown in Figure 4.4.

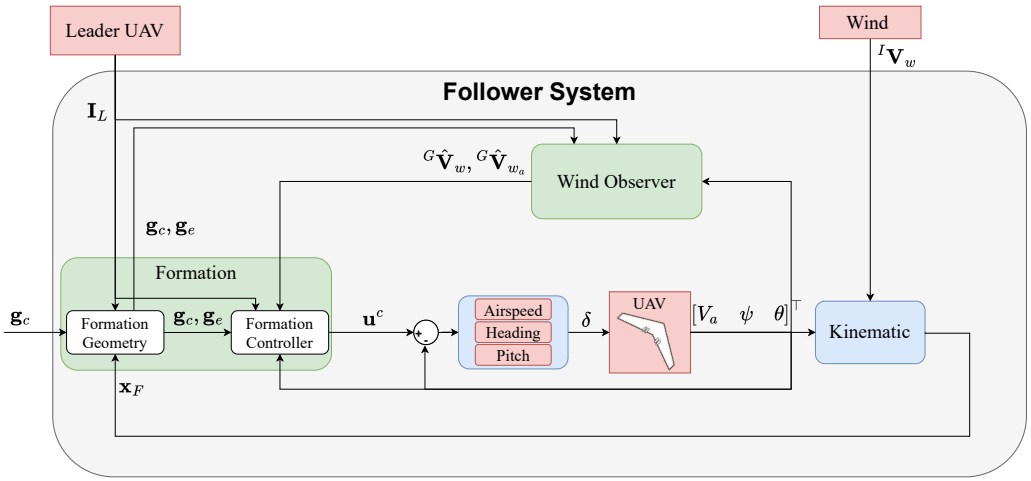

Figure 4.4: The proposed control architecture for the follower UAV.

doi:10.6342/NTU202500345

Chapter 5

Proposed Method

In this chapter, a Lyapunov-based formation controller (LBFC) with a sliding mode wind observer (SMWO) is proposed for the fixed-wing UAVs formation flight under variant wind field. In Section 5.1, a LBFC based on the known wind information will be first derived. Then, in Section 5.2, a SMWO will be designed to estimate the wind velocity and wind acceleration. Finally, the wind estimation information is incorporated into the formation controller to obtain the practical Lyapunov-based formation controller, which is named as Lyapunov-based formation controller with sliding mode wind observer (LBFC-SMWO).

5.1 Lyapunov-Based Formation Controller

The control objective is to design control commands $\mathbf{u}^c$ such that the formation error $\mathbf{g}_e$ approaches zero asymptotically. In this section, a 2-step controller design is proposed to achieve the control objective assumed that the wind information is known.

The first step is to design desired follower UAV states, $\mathbf{x}^d := \begin{bmatrix} V_{aF}^d & \psi_F^d & \theta_F^d \end{bmatrix}^\top \in \mathbb{R}^3$ and prove that when the follower UAV follows the desired states, the $\mathbf{g}_e$ will converges to zero.

The second step is to design the control commands $\mathbf{u}^c$ to guarantee the follower UAV track the desired states. The formation controller diagram is shown in Figure 5.1. Where $\mathbf{I}_L := \begin{bmatrix} \mathbf{p}_L^\top & \chi_L & \dot{\chi}_L & \dot{z}_L & V_L \end{bmatrix}^\top$ is the required leader's information for the formation controller.

doi:10.6342/NTU202500345

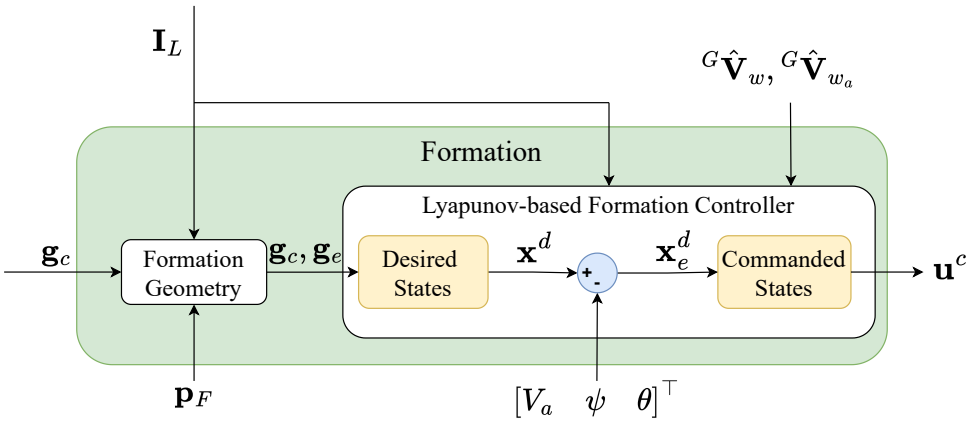

Figure 5.1: The proposed Lyapunov-based formation controller diagram.

5.1.1 Desired Follower UAV States Design

To derive the desired follower UAV states $\mathbf{x}^d$, the following Lyapunov candidate is defined as

$$W_1(\mathbf{g}_e) = \frac{1}{2}\|\mathbf{g}_e\|_2^2. \tag{5.1}$$

The time derivative of Equation (5.1) is

$$\begin{aligned} \dot{W}_1 &= \mathbf{g}_e^\top \dot{\mathbf{g}}_e \\ &= l_e\dot{l}_e + f_e\dot{f}_e + h_e\dot{h}_e, \end{aligned} \tag{5.2}$$

then the formation error dynamics in Equation (4.12) can be substituted into Equation (5.2) and the time derivative of W_1 can be rewritten as

$$\begin{aligned} \dot{W}_1 =& l_e(V_{aF}\sin(\psi_F - \chi_L) + \dot{\chi}_L f_c + w_l) + \\ & f_e(V_L - V_{aF}\cos(\psi_F - \chi_L) - \dot{\chi}_L l_c + w_f) + \\ & h_e(V_L \sin\gamma_L - V_{aF}\sin\theta_F + w_h). \end{aligned} \tag{5.3}$$

In order to satisfy the requirement of the Lyapunov's stability theorem [38: Khalil 2002],

doi:10.6342/NTU202500345

the following relations are constructed:

$$V_{aF}\sin\left(\psi_F-\chi_L\right)+\dot{\chi}_L f_c+w_l=-c_1 l_e, \tag{5.4}$$

$$V_L-V_{aF}\cos\left(\psi_F-\chi_L\right)-\dot{\chi}_L l_c+w_f=-c_2 f_e, \tag{5.5}$$

$$V_L\sin\gamma_L-V_{aF}\sin\theta_F+w_h=-c_3 h_e, \tag{5.6}$$

where c_1, c_2, c_3 are positive constants. By substituting Equation (5.4), Equation (5.5), and Equation (5.6) into Equation (5.3), $\dot{W}_1$ can be further represented as

$$\dot{W}_1=-c_1 l_e^2-c_2 f_e^2-c_3 h_e^2<0. \tag{5.7}$$

Because $W_1>0$ and is radially unbounded, and $\dot{W}_1<0$ in $\mathbb{R}^3-\{\mathbf{0}\}$, which satisfy the requirement of Lyapunov's stability theorem [38: Khalil 2002]. As a result, $\mathbf{g}_e=\mathbf{0}$ is globally asymptotically stable (G.A.S).

In order to meet the relation in Equation (5.4), Equation (5.5), and Equation (5.6), V_{aF}^d can be designed by taking Equation (5.4) and Equation (5.5) squared on both sides then sum them up,

$$\begin{aligned}
\left(V_{aF}^d\sin\left(\psi_F-\chi_L\right)\right)^2&=\left(-c_1 l_e-\dot{\chi}_L f_c-w_l\right)^2\\
\left(V_{aF}^d\cos\left(\psi_F-\chi_L\right)\right)^2&=\left(c_2 f_e-\dot{\chi}_L l_c+V_L+w_f\right)^2\\
&\Downarrow\\
\left(V_{aF}^d\right)^2&=\left(-c_1 l_e-\dot{\chi}_L f_c-w_l\right)^2+\left(c_2 f_e-\dot{\chi}_L l_c+V_L+w_f\right)^2\\
V_{aF}^d&=\sqrt{\left(c_1 l_e+\dot{\chi}_L f_c+w_l\right)^2+\left(c_2 f_e-\dot{\chi}_L l_c+V_L+w_f\right)^2}.
\end{aligned} \tag{5.8}$$

Similarly, ψ_F^d can be designed by dividing Equation (5.4) by Equation (5.5) [17: Yu *et al.*

doi:10.6342/NTU202500345

2018], [18: Zhang *et al.* 2021],

$$
\begin{aligned}
V_{aF}\sin\left(\psi_F^d-\chi_L\right) &= -c_1 l_e-\dot{\chi}_L f_c-w_l \\
V_{aF}\cos\left(\psi_F^d-\chi_L\right) &= c_2 f_e-\dot{\chi}_L l_c+V_L+w_f \\
&\Downarrow \\
\tan\left(\psi_F^d-\chi_L\right) &= \frac{-c_1 l_e-\dot{\chi}_L f_c-w_l}{c_2 f_e-\dot{\chi}_L l_c+V_L+w_f} \\
\psi_F^d &= \arctan\left\{\frac{-c_1 l_e-\dot{\chi}_L f_c-w_l}{c_2 f_e-\dot{\chi}_L l_c+V_L+w_f}\right\}+\chi_L.
\end{aligned}
\tag{5.9}
$$

Lastly, θ_F^d can be designed by simply taking the mathematical operation of Equation (5.6),

$$
\begin{aligned}
V_L\sin\gamma_L-V_{aF}\sin\theta_F^d+w_h &= -c_3 h_e \\
&\Downarrow \\
\theta_F^d &= \arcsin\left(\frac{c_3 h_e+V_L\sin\gamma_L+w_h}{V_{aF}^d}\right).
\end{aligned}
\tag{5.10}
$$

Finally, the desired follower UAV states can be summarized in Equation (5.11).

$$
\begin{aligned}
V_{aF}^d &= \sqrt{(c_1 l_e+\dot{\chi}_L f_c+w_l)^2+(c_2 f_e-\dot{\chi}_L l_c+V_L+w_f)^2} \\
\psi_F^d &= \arctan\left\{\frac{-c_1 l_e-\dot{\chi}_L f_c-w_l}{c_2 f_e-\dot{\chi}_L l_c+V_L+w_f}\right\}+\chi_L \\
\theta_F^d &= \arcsin\left(\frac{c_3 h_e+V_L\sin\gamma_L+w_h}{V_{aF}^d}\right).
\end{aligned}
\tag{5.11}
$$

Equation (5.11) shows that the $\mathbf{g}_e=\mathbf{0}$ is G.A.S when the follower UAV tracks the desired states $\mathbf{u}^d$, which means that the states errors of the follower UAV, $\mathbf{x}_e^d:=[V_{ae}^d,\psi_e^d,\theta_e^d]^\top\in\mathbb{R}^3$ should converge to zero, i.e.,

$$
\begin{aligned}
V_{ae}^d &:= V_{aF}-V_{aF}^d, \quad |V_{ae}^d|\to 0, \\
\psi_e^d &:= \psi_F-\psi_F^d, \quad |\psi_e^d|\to 0, \\
\theta_e^d &:= \theta_F-\theta_F^d, \quad |\theta_e^d|\to 0.
\end{aligned}
\tag{5.12}
$$

doi:10.6342/NTU202500345

where $\psi_e^d \in [-\pi, \pi]$.

5.1.2 Controller Command Design

To guarantee the Equation (5.12) is satisfied, following the similiar process as obtaning the desired follower states, another Lyapunov candidate, W_2, is defined as

$$W_2(\mathbf{x}_e^d) = \frac{1}{2}\|\mathbf{x}_e^d\|_2^2. \tag{5.13}$$

The time derivative of Equation (5.13) becomes

$$\begin{aligned}\dot{W}_2 &= \mathbf{x}_e^{d\top}\dot{\mathbf{x}}_e^d \\ &= V_{ae}^d \dot{V}_{ae}^d + \psi_e^d \dot{\psi}_e^d + \theta_e^d \dot{\theta}_e^d \\ &= V_{ae}^d(\dot{V}_{aF} - \dot{V}_{aF}^d) + \psi_e^d(\dot{\psi}_F - \dot{\psi}_F^d) + \theta_e^d(\dot{\theta}_F - \dot{\theta}_F^d).\end{aligned} \tag{5.14}$$

From Assumption 3, we stated that there are the innerloop hold systems assumed to be first order systems as in Equation (4.6). Therefore, Equation (5.14) can be written as

$$\dot{W}_2 = V_{ae}^d(\tau_{V_a}(V_{aF}^c - V_{aF}) - \dot{V}_{aF}^d) + \psi_e^d(\tau_\psi(\psi_F^c - \psi_F) - \dot{\psi}_F^d) + \theta_e^d(\tau_\theta(\theta_F^c - \theta_F) - \dot{\theta}_F^d). \tag{5.15}$$

Next, we construct the following relationships:

$$\begin{aligned}\tau_{V_a}(V_{aF}^c - V_{aF}) - \dot{V}_{aF}^d &= -c_4 V_{ae}^d, \\ \tau_\psi(\psi_F^c - \psi_F) - \dot{\psi}_F^d &= -c_5 \psi_e^d, \\ \tau_\theta(\theta_F^c - \theta_F) - \dot{\theta}_F^d &= -c_6 \theta_e^d,\end{aligned} \tag{5.16}$$

where c_4, c_5, c_6 are positive constants. By subsituting Equation (5.16) into Equation (5.15),

doi:10.6342/NTU202500345

$\dot{W}_2$ can be further represented as

$$\dot{W}_2 = -c_4 {V_{a_e}^d}^2 - c_5 {\psi_e^d}^2 - c_6 {\theta_e^d}^2 < 0. \tag{5.17}$$

Because $W_2 > 0$ and is radially unbounded, and $\dot{W}_2 < 0$ in $\mathbb{R}^3 - \{\mathbf{0}\}$, which satisfy the requirement of Lyapunov's stability theorem [38: Khalil 2002]. As a result, $\mathbf{u}_e^d = \mathbf{0}$ is also globally asymptotically stable (G.A.S).

From the Equation (5.16), the control commands can then be derived trivially as

$$\begin{aligned} V_{aF}^c &= \frac{1}{\tau_{V_a}}(\dot{V}_{aF}^d - c_4 V_{a_e}^d) + V_{aF}, \\ \psi_F^c &= \frac{1}{\tau_\psi}(\dot{\psi}_F^d - c_5 \psi_e^d) + \psi_F, \\ \theta_F^c &= \frac{1}{\tau_\theta}(\dot{\theta}_F^d - c_6 \theta_e^d) + \theta_F, \end{aligned} \tag{5.18}$$

where the dynamics of desired follower UAV states can be calculated from the time derivative of the Equation (5.11) as

$$\begin{aligned} \dot{V}_{aF}^d &= \frac{\dot{a}a + \dot{b}b}{\sqrt{a^2 + b^2}}, \\ \dot{\psi}_F^d &= \frac{\dot{a}b - a\dot{b}}{a^2 + b^2} + \dot{\chi}_L, \\ \dot{\theta}_F^d &= \frac{\dot{c}V_{aF}^d - c\dot{V}_{aF}^d}{{V_{aF}^d}^2 \sqrt{{V_{aF}^d}^2 - c^2}}, \end{aligned} \tag{5.19}$$

where the auxiliary variables a, b, c are defined as

$$\begin{aligned} a &:= -c_1 l_e - \dot{\chi}_L f_c - w_l, \\ b &:= c_2 f_e - \dot{\chi}_L l_c + V_L + w_f, \\ c &:= c_3 h_e + V_L \sin\gamma_L + w_h. \end{aligned} \tag{5.20}$$

Under Assumption 6, $\dot{V}_L$, $\ddot{\chi}_L$ and $\dot{\gamma}$ can be regarded as zero. Then the dynamics of the

doi:10.6342/NTU202500345

auxiliary variables $\dot{a}, \dot{b}, \dot{c}$ can be further represented as

$$\begin{aligned} \dot{a} &= -c_1 \dot{l}_e - \dot{w}_l \\ \dot{b} &= c_2 \dot{f}_e + \dot{w}_f \\ \dot{c} &= c_3 \dot{h}_e + \dot{w}_h \end{aligned} \cdot \tag{5.21}$$

It is worth noting that Equation (5.18) can not be applied directly to the follower UAV due to the unknown wind velocity w_l, w_f, w_h in Equation (5.20) and wind accerlation $\dot{w}_l, \dot{w}_f, \dot{w}_h$ in Equation (5.21). To address this issue, a sliding mode observer to estimate the wind velocity and acceleration will be elaborated on Section 5.2.

5.2 Sliding Mode Wind Observer

This section provides the derivation of the estimated wind velocity and wind acceleration using first order differentiator which is a modification of super-twisting controller [21: Shtessel *et al.* 2014]. The concept of the designed sliding mode wind observer is referred to [20: Yang *et al.* 2021]. In [20: Yang *et al.* 2021], a second order differentiator is used to estimate the wind velocity and wind acceleration under inertial frame $\{I\}$. In this work, the wind velocity and wind acceleration should be estimated under the geometry frame $\{G\}$ instead. A intuitive way is to estimate the ${}^{I}\mathbf{V}_w$ and ${}^{I}\mathbf{V}_{w_a}$ first and then transform them into the geometry frame $\{G\}$ using the relation in Equation (4.3).

$${}^{G}\hat{\mathbf{V}}_w = {}^{I}_{G}\mathbf{R}\,{}^{I}\hat{\mathbf{V}}_w, \tag{5.22}$$

However, this method does not work for the transformation of wind acceleration between $\{I\}$ and $\{G\}$ because the dynamic of the $\{G\}$ relative to the $\{I\}$ is not considered in the observer designed in [20: Yang *et al.* 2021]. As a result, this thesis proposes a new sliding

doi:10.6342/NTU202500345

mode wind observer design to estimate the ${}^{G}\mathbf{V}_{w}$ and ${}^{G}\mathbf{V}_{w_a}$ under the geometry frame $\{G\}$ directly.

The proposed wind observers can be divided into two observers. The first one is wind velocity observer which estimates the wind velocity ${}^{G}\hat{\mathbf{V}}_{w}$ and formation error $\hat{\mathbf{g}}_{e}$ using the first order differentiator. The second one is wind acceleration observer which estimates the wind acceleration ${}^{G}\hat{\mathbf{V}}_{w_a}$ and second wind velocity ${}^{G}\hat{\mathbf{V}}_{w_2}$ using the estimated wind velocity ${}^{G}\hat{\mathbf{V}}_{w}$ from the first observer by applying another first order differentiator. The overall wind observer block diagram is shown in Figure 5.2.

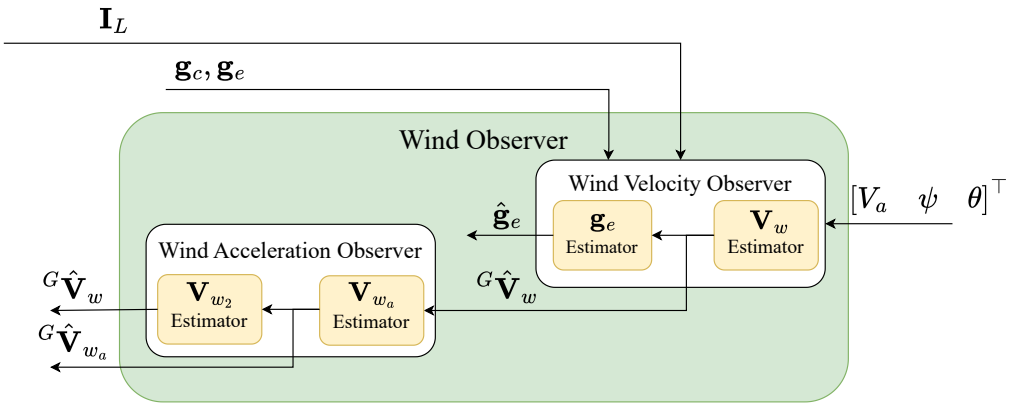

Figure 5.2: The proposed sliding mode wind observer block diagram. Including wind velocity observer and wind acceleration observer.

5.2.1 Wind Velocity Observer

In order to simplify the derivation of the following observers, we define

$$\begin{aligned}
\dot{l}_{e_0} &:= V_{aF} \sin(\psi_F - \chi_L) + \dot{\chi}_L(f_e + f_c), \\
\dot{f}_{e_0} &:= V_L - V_{aF} \cos(\psi_F - \chi_L) + \dot{\chi}_L(-l_e - l_c), \\
\dot{h}_{e_0} &:= V_L \sin\gamma_L - V_{aF} \sin\theta_F,
\end{aligned} \tag{5.23}$$

doi:10.6342/NTU202500345

the Equation (4.12) can be rewritten as Equation (5.24) for $* \in \{l, f, h\}$.

$$\dot{*}_e = \dot{*}_{e_0} + w_*. \tag{5.24}$$

Let the sliding variables be $\sigma_* = \hat{*}_e - *_e$ and consider an auxiliary system as $\dot{\hat{*}}_e = \nu$. The time derivative of the sliding variable is

$$\dot{\sigma}_* = -\dot{*}_e + \nu. \tag{5.25}$$

Substitute Equation (5.24) into Equation (5.25),

$$\begin{aligned} \dot{\sigma}_* &= -\dot{*}_e + \nu \\ &= -w_* + \nu - \dot{*}_{e_0} \\ &= -w_* + u_*, \end{aligned} \tag{5.26}$$

where $u_* := \nu - \dot{*}_{e_0}$, which can be regarded as the control input of the designed observer. A first order differentiator [21: Shtessel *et al.* 2014] can now be applied to Equation (5.26),

$$\begin{aligned} u_* &= -\lambda_1 |\sigma_*|^{\frac{1}{2}} \text{sign}(\sigma_*) + \hat{w}_*, \\ \dot{\hat{w}}_* &= -\lambda_0 \text{sign}(\sigma_*), \end{aligned} \tag{5.27}$$

The final wind velocity observer can be obtained by substituting the auxiliary system and control input back into Equation (5.27),

$$\begin{aligned} \dot{\hat{*}}_e &= \dot{*}_{e_0} - \lambda_1 |\sigma_*|^{\frac{1}{2}} \text{sign}(\sigma_*) + \hat{w}_*, \\ \dot{\hat{w}}_* &= -\lambda_0 \text{sign}(\sigma_*), \end{aligned} \tag{5.28}$$

where $\lambda_0 = 1.1 L_1$ and $\lambda_1 = 1.5 L_1$, which is selected and validated by rule of thumb [21:

doi:10.6342/NTU202500345

Shtessel *et al.* 2014]. L_1 is a Lipschitz constant satisfied with

$$L_1 \geq |\dot{w}_*|. \tag{5.29}$$

5.2.2 Wind Acceleration Observer

After deriving the wind velocity observer, the wind acceleration observer can be designed by applying the same procedure. However, the real wind velocity ${}^G\mathbf{V}_w$ can not be directly measurable; therefore, the estimated wind velocity ${}^G\hat{\mathbf{V}}_w$ from the wind velocity observer is used instead. The wind acceleration system is defined as

$$\dot{\hat{w}}_* = a_*, \tag{5.30}$$

and let the sliding variable be $\sigma_{a_*} = \hat{w}_{*_2} - \hat{w}_*$, the wind acceleration observer can be designed as

$$\begin{aligned} \dot{\hat{w}}_{*_2} &= -\lambda_3 |\sigma_{a_*}|^{\frac{1}{2}} \text{sign}(\sigma_{a_*}) + \hat{a}_*, \\ \dot{\hat{a}}_* &= -\lambda_2 \text{sign}(\sigma_{a_*}), \end{aligned} \tag{5.31}$$

where $\lambda_2 = 1.1L_2$, $\lambda_3 = 1.5L_2$, and L_2 is a Lipschitz constant satisfied with

$$L_2 \geq |\dot{a}_*|. \tag{5.32}$$

An intuitive explanation of why the Lipschitz condition, Equation (5.29) and Equation (5.32), are needed is that if L_1 and L_2 are not big enough, the true wind acceleration and wind jerk will go beyond the observer's capability to estimate.

It is worth mentioning that although both ${}^G\hat{\mathbf{V}}_w$ and ${}^G\hat{\mathbf{V}}_{w_2}$ give us the estimated wind velocity, their properties are quiet different. Because ${}^G\hat{\mathbf{V}}_{w_2}$ is estimated from ${}^G\hat{\mathbf{V}}_w$, the

doi:10.6342/NTU202500345

convergence time of ${}^{G}\hat{\mathbf{V}}_{w_2}$ must be longer than ${}^{G}\hat{\mathbf{V}}_{w}$. On the other hand, ${}^{G}\hat{\mathbf{V}}_{w_2}$ is smoother than ${}^{G}\hat{\mathbf{V}}_{w}$ due to the integration of ${}^{G}\hat{\mathbf{V}}_{w_a}$. The more detailed comparison and discussion will left to be shown in the Chapter 6.

5.3 LBFC-SMWO

The proposed LBFC-SMWO can be obtained by substituting the estimated wind velocity and wind acceleration from the wind observer, Equation (5.28) and Equation (5.31), into the auxiliary variables, Equation (5.20) and Equation (5.21), which is included in the control commands, Equation (5.18). The overall block diagram of the proposed LBFC-SMWO is shown in Figure 5.3.

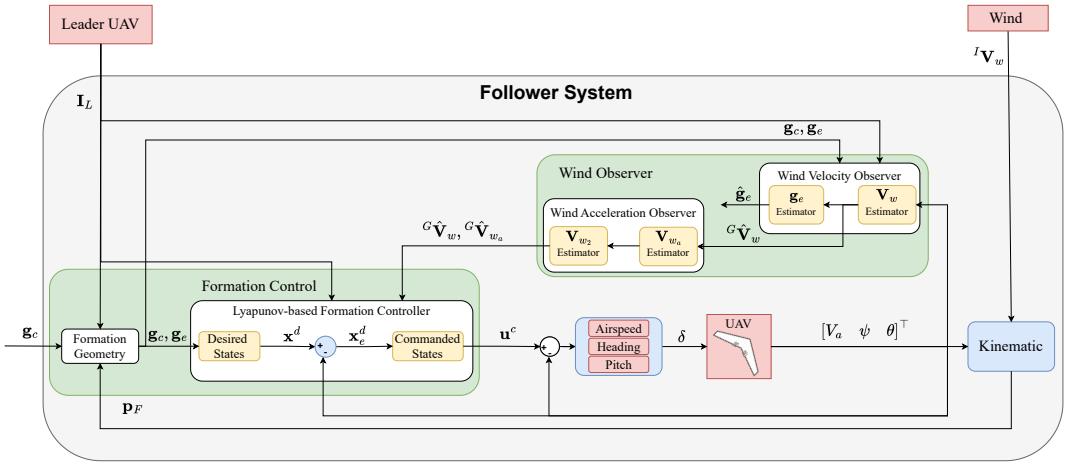

Figure 5.3: The block diagram of the proposed LBFC-SMWO in the follower UAV system.

5.4 Stability Issues

The stability of the proposed LBFC and LBFC-SMWO has not been proved in this thesis. Equation (5.7) and Equation (5.17) show that the formation error and the states error of the follower UAV will converge to zero asymptotically. It remains to show that existing a Lyapunov candidate $W = W_1 + W_2$ satifying the following inequalities [38:

doi:10.6342/NTU202500345

Khalil 2002] to guarantee the stability of the proposed LBFC.

$$W > 0, \tag{5.33}$$

$$\dot{W} < 0.$$

After the stability of the LBFC is proved, the stability of the LBFC-SMWO should be analyzed by considering the SMWO's dynamics.

doi:10.6342/NTU202500345

Chapter 6

Simulations

In this chaper, the effectiveness of the proposed Lyapunov-based formation controller and sliding mode wind observer are validated through two simulation methods, model-in-the-loop (MIL) and software-in-the-loop (SITL), respectively. In the MIL simulation, the proposed LBFC-SMWO are implemented in MATLAB/Simulink@R2023b with continuous system. The perfect inner-loop controller for airspeed, heading angle, and pitch angle are designed according to Equation (4.6), and the inverse time constant of each controller are set to be $\tau_{V_a} = \tau_\psi = \tau_\theta = 0.5$. As for the SITL simulation, the open-source PX4 autopilot [19: Meier *et al.* 2015] has provided off-the-shelf SITL simulation package, which is easy to be integrated with the proposed algorithm and validated the performance in a more realistic environment.

6.1 Performance Indices

To evaluate the performance of the proposed LBFC-SMWO numerically, the following two performance indices are adopted:

- Integral Absolute Error (IAE): The IAE [42: Dorf and Bishop 2017] is defined as

$$\text{IAE} := \sum_{i=0}^{t_r} |e_i|, \tag{6.1}$$

  where e_i is the error between the reference and the actual value at time i and t_r is the total time to reach steady state. The IAE is used to evaluate the transient state performance of the system.

doi:10.6342/NTU202500345

- Root Mean Square Error (RMSE): The RMSE is defined as

$$\text{RMSE} := \sqrt{\frac{1}{t_f - t_r} \sum_{i=t_r}^{t_f} e_i^2}, \tag{6.2}$$

where t_f is the final time of the simulation. The RMSE is used to evaluate the steady state performance of the system.

6.2 MIL Simulation

6.2.1 SMWO Performance Evaluation

The proposed SMWO performance is evaluated from three aspects:

- The relation of the wind velocity estimation between which from the wind observer and the acceleration observer, i.e., $\hat{\mathbf{V}}_w$ and $\hat{\mathbf{V}}_{w_2}$.
- The influence of the initial formation error to the estimation performance.
- The effect of the different observer gains, L_1 and L_2, to the estimation results.

To better observing the wind estimation results, we consider a formation flight with only one follower and one virtual leader which will not be affected by the wind. In other words, a virtual leader can be considered as a reference trajectory for the follower to follow. The virtual leader's trajectory expressed in inertial frame $\{I\}$ is

$$\mathbf{p}_L(t) = \begin{bmatrix} V_{L_h} t & 0 & -90 + V_{L_v} t \end{bmatrix}^\top, \quad t \in [0, t_f] s, \tag{6.3}$$

where $t_f = 30$ is the final time of the simulation, $V_{L_h} = \sqrt{V_L^2 - V_{L_v}^2}$ m/s, $V_{L_v} = -1$ m/s and $V_L = 18$ m/s represents the components of virtual leader's ground speed in horizontal and vertical, respectively. The required virtual leader's information for SMWO can be

doi:10.6342/NTU202500345

represented as

$$\mathbf{I}_L(t) = \begin{bmatrix} \mathbf{p}_L^\top(t) & 0 & 0 & V_{L_v} & V_L \end{bmatrix}^\top. \tag{6.4}$$

The steady wind profile combined with constant and sinusoidal parts is

$$\mathbf{V}_w(t) = \mathbf{V}_{w_{sc}} + \mathbf{V}_{w_{ss}} = \begin{bmatrix} 2(1-e^{-2t}) + \sin(0.2t) \\ -\sin(0.2t) \\ 0.7\sin(0.2t) \end{bmatrix}, \quad t \in [0, 30]s. \tag{6.5}$$

The formation configurations $\mathbf{g}_c = \begin{bmatrix} 0 & 0 & 0 \end{bmatrix}^\top$. The LBFC controller gains and the initial conditions for the virtual leader and the follower are listed in Table 6.1 and Table 6.2, separately.

Table 6.1: The LBFC gains for the the SMWO performance evaluation.

Parameter	c_1	c_2	c_3	c_4	c_5	c_6
Value	1.0	1.0	1.0	3.0	3.0	3.0

Table 6.2: Initial conditions of the leader and the follower for the SMWO performance evaluation.

Parameter	**Value**	**Parameter**	**Value**	**Unit**
x_{L_0}	0	x_{F_0}	10	m
y_{L_0}	0	y_{L_0}	-10	m
z_{L_0}	-90	z_{L_0}	-100	m
V_{L_0}	18	V_{F_0}	18	m/s
ϕ_{L_0}	0	ϕ_{F_0}	0	rad
γ_{L_0}	0.055	θ_{F_0}	0	rad
χ_{L_0}	0	ψ_{F_0}	$\frac{\pi}{18}$	rad

Notice that the difference of the initial position between the leader and follower is for better observing the transient state of the wind estimation. This part will be discussed in Section 6.2.1.2.

doi:10.6342/NTU202500345

6.2.1.1 Comparison of the Estimated Wind Velocity from Wind Velocity Observer and Acceleration Observer

Figure 6.1 shows the result of the wind velocity estimation from wind observer and wind acceleration observer with fixed observer gains $L_1 = 1$ and different $L_2 = 0.1, 1.0, 10$. By observing Figure 6.1(a), Figure 6.1(b), and Figure 6.1(c), the $\mathbf{V}_{w_2}$ is indeed smoother than $\mathbf{V}_w$ due to the integration from the discontinuous acceleration estimation. At the same time, $\mathbf{V}_{w_2}$ also converges slower than $\mathbf{V}_w$ because the estimation of $\mathbf{V}_{w_2}$ is based on the estimation of $\mathbf{V}_w$. By increasing the value of the observer gain L_2, the convergence speed of $\mathbf{V}_{w_2}$ can be improved and almost align with $\mathbf{V}_w$. However, an over-large observer gain L_2, or more precisely say that an inappropriate ratio of L_1 and L_2 will cause some problems for the wind acceleration estimation. These problems will be revealed in Section 6.2.1.3.

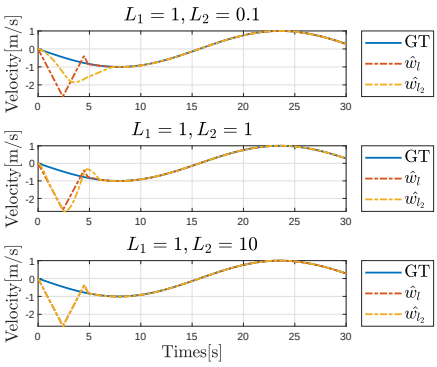

(a) $\hat{w}_l$ vs. $\hat{w}_{l_2}$.

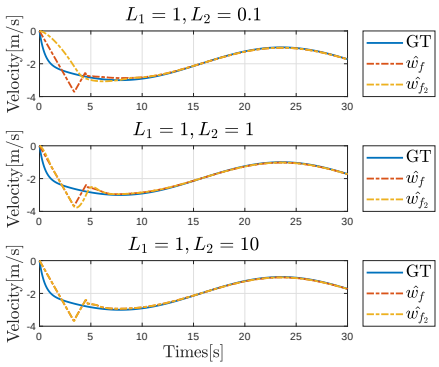

(b) $\hat{w}_f$ vs. $\hat{w}_{f_2}$.

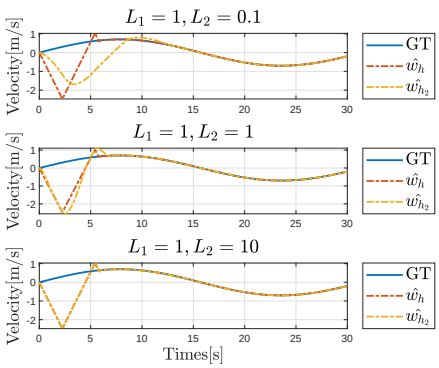

(c) $\hat{w}_h$ vs. $\hat{w}_{h_2}$.

Figure 6.1: The comparison of the estimated wind velocity from wind observer $\hat{\mathbf{V}}_w$ and acceleration observer $\hat{\mathbf{V}}_{w_2}$. GT means the ground truth of the wind velocity.

doi:10.6342/NTU202500345

6.2.1.2 Initial Formation Error Influence on SMWO

To investigate how the initial formation error affects the transient of the wind velocity estimation, the observer gains are first fixed as $L_1 = 1$ and $L_2 = 0.1$; the initial formation error $\mathbf{g}_{e_0}$ are set to be $[-10, -10, -10]^\top$, $[0, 0, 0]^\top$, and $[10, 10, 10]^\top$, respectively. The relation between the initial formation error and the initial position of the follower UAV are listed in Table 6.3.

Table 6.3: Relation between the initial formation error and the initial position of the follower UAV.

$l_{e_0} = f_{e_0} = h_{e_0}$	x_{F_0}	y_{F_0}	z_{F_0}
-10	10	-10	-100
0	0	0	-90
10	-10	10	-80

Figure 6.2 shows the results of $\hat{\mathbf{V}}_w$ and $\hat{\mathbf{V}}_{w_2}$ with different initial formation errors. When the initial formation error is -10 or 10, the initial transient state of the estimation goes the opposite direction with respect to the ground truth value, which can be explained by Equation (5.28). Take the case when the initial formation error is -10 as an example, the initial sliding variable σ_{*_0} is 10 because the initial estimation of the formation error $\hat{*}_{e_0}$ are always set to be 0. As a result, the $\dot{\hat{w}}_*$ will keep being negative and the $\hat{w}_*$ will keep decreasing untill the formation error estimation catch up the real value. The observation when the initial formation error is 10 can be explained by the same token.

It is worth noting that when the initial formation error is 0, the estimation of the wind velocity should be always align with the ground truth value, or precisely speaking, zigzag move along with the ground truth value. However, the $\hat{w}_f$ and $\hat{w}_{f_2}$ do not show this behavior. This is because an exponential term dominating the wind profile at the begining of the simulation, which makes the wind acceleration is too large to follow the Lipschitz contraints in Equation (5.29). To verify this, the observer gains are increased

doi:10.6342/NTU202500345

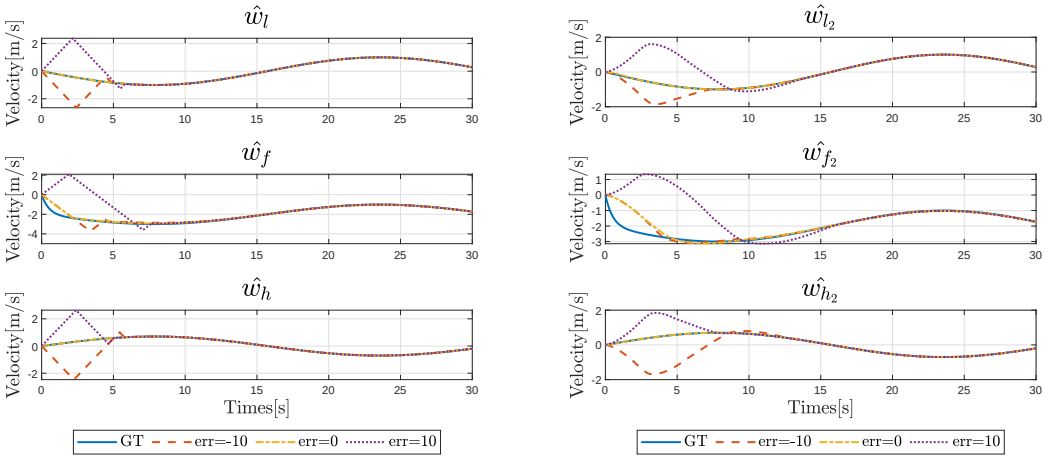

(a) $\hat{\mathbf{V}}_w$. **(b) $\hat{\mathbf{V}}_{w_2}$.**

Figure 6.2: The influence of initial formation error on wind velocity estimation process. The observer gains are $L_1 = 1$ and $L_2 = 0.1$. err represents the initial formation error.

to $L_1 = 10$ and $L_2 = 0.1$, and the results are shown in Figure 6.3. In this case, the $\hat{w}_f$ is exactly aligned with the ground truth value at the beginning, and the $\hat{w}_{f_2}$ remains the same behavior as before because the observer gain L_2 remains unchanged and violates the Equation (5.32).

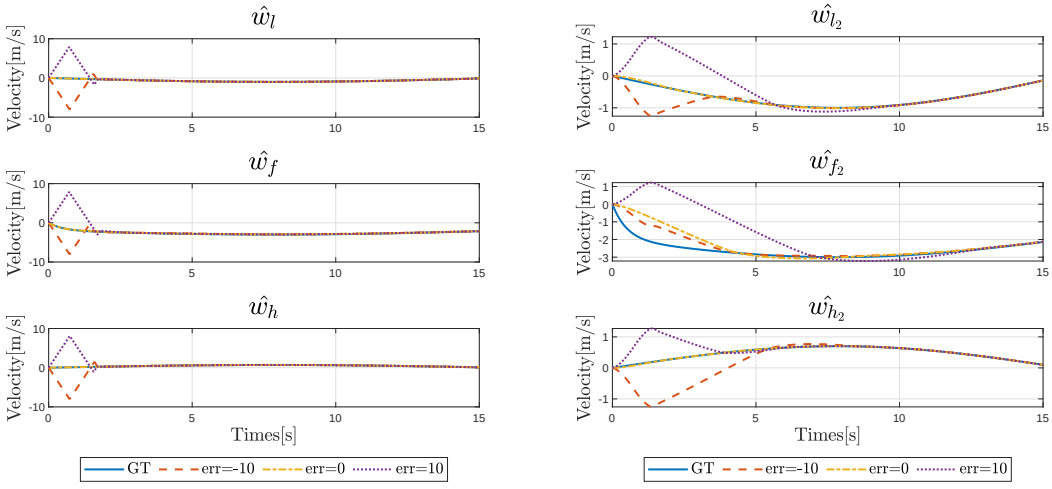

(a) $\hat{\mathbf{V}}_w$. **(b) $\hat{\mathbf{V}}_{w_2}$.**

Figure 6.3: The influence of initial formation error on wind velocity estimation process. The observer gains are $L_1 = 10$ and $L_2 = 0.1$. Zoom in the first 15 s.

6.2.1.3 Observer Gain Influence on SMWO

doi:10.6342/NTU202500345

The relation between the different observer gains L_1, L_2 and the estimation performance of wind velocity and wind acceleration are discussed in this section. The initial formation error is set to be $[-10, -10, -10]^\top$ for the better observations of the transient state of the estimation. L_1 and L_2 are considered to be 0.1, 1, 10. The wind velocity estimation $\mathbf{V}_{w_2}$ results are shown in Figure 6.4, and the wind acceleration estimation $\mathbf{V}_{w_a}$ results are shown in Figure 6.5. At the beginning, from the wind profile Equation (6.5), we knows that the L_1 should be larger than 0.2 and L_2 should be larger than 0.04 to satisfy the Lipschitz constraints Equation (5.29) and Equation (5.32). As a result, when $L_1 = 0.1$, the estimation value fails to converge to the ground truth value.

On the other hand, by the discussion in Section 6.2.1.1, the larger the L_2 is, the faster the convergence speed of the wind velocity estimation $\mathbf{V}_{w_2}$ is. However, too large L_2 will cause the wind acceleration estimation $\mathbf{V}_{w_a}$ to converge to the undesired transient state of the $\mathbf{V}_w$, which can be especially observed from the case when $L_1 = 1$ and $L_2 = 10$ in Figure 6.5(a), Figure 6.5(c), and Figure 6.5(e). Overall, the larger the observer gains are, the faster the convergence speed of the estimation is, the larger the overshoot of the estimation is, and the bigger the zigzag amplitude of the estimation is as well. The estimation results of different observer gains are concluded in Table 6.4.

Table 6.4: The performance of wind velocity and wind acceleration estimation with different observer gains, L_1 and L_2.

		L_1		
		0.1	1	10
L_2	0.1	L_1 not satisfy Lipschitz constraints.	**Balance**.	Converging speed: slow.
	1	L_1 not satisfy Lipschitz constraints.	Balance. Accel. estimates transient state.	**Balance**.
	10	L_1 not satisfy Lipschitz constraints.	Accel. estimates transient state.	Max oscillation: large.

Balance represents the moderate converging speed and maximum overshoot of the

doi:10.6342/NTU202500345

estimation. From Table 6.4, the best observer gains ratio, L_1 over L_2, can be concluded as 10. It is worth noting that how large the observer gains should be are determined by the property of the wind profile, i.e., the observer gains should obey the Lipschitz constraints, and that's why the best observer gains ratio is proposed instead of the best observer gains.

6.2.2 LBFC-SMWO Performance Evaluation

The proposed LBFC-SMWO is evaluated from two different formation flight trajectories, the straight line and the circular orbit, because other kinds of different trajecotories,i.e., bow-tie shape, can be decomposed into several pieces of these two basic trajectories. Without loss of generality, a formation flight with one follower and one virtual leader is considered. The LBFC-SMWO performance will be focused on analyzing the follower's system response through IAE and RMSE. The steady wind profile of the constant $\mathbf{V}_{w_{sc}}$ and sinusoidal $\mathbf{V}_{w_{ss}}$ parts are

$$\begin{aligned} \mathbf{V}_w &= \mathbf{V}_{w_{sc}} + \mathbf{V}_{w_{ss}}, \\ \mathbf{V}_{w_{sc}} &= \begin{bmatrix} M(1-e^{-2t})\cos(D) & M(1-e^{-2t})\sin(D) & 0 \end{bmatrix}^\top, \\ \mathbf{V}_{w_{ss}} &= \begin{bmatrix} 1\sin(0.2t) & -1\sin(0.2t) & 0.7\sin(0.2t) \end{bmatrix}^\top, \end{aligned} \tag{6.6}$$

where M means the magnitude of the constant steady wind and D represents the direction of the constant steady wind. The formation configurations are set to $\mathbf{g}_c = \begin{bmatrix} -7 & 14 & 0 \end{bmatrix}^\top$. The LBFC gains and the SMWO gains are listed in Table 6.5.

6.2.2.1 Formation Flight in Straight Line Trajectory

In the straight line formation flight, the virtual leader fly straight along with $\frac{\pi}{4}$ radians

doi:10.6342/NTU202500345

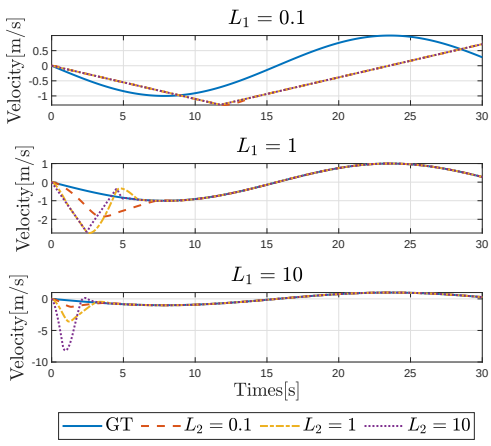

(a) $\hat{w}_{l_2}$.

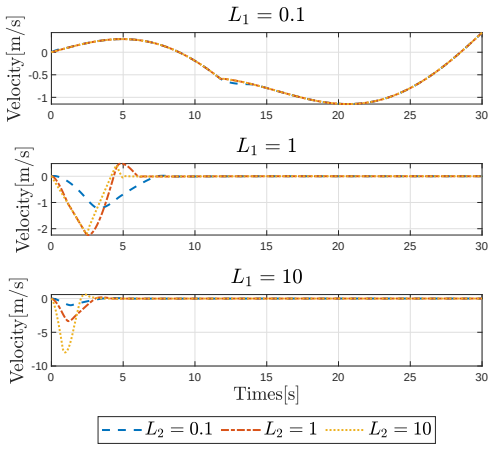

(b) $\hat{w}_{l_2}$ **estimation error.**

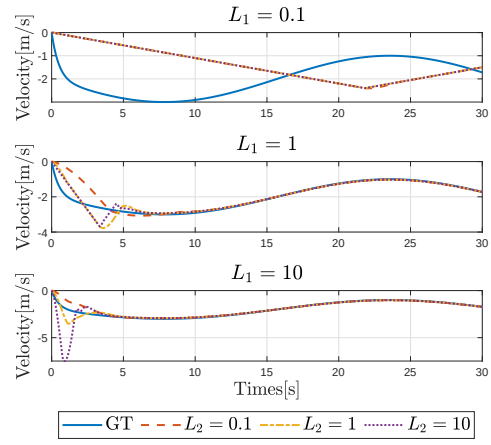

(c) $\hat{w}_{f_2}$.

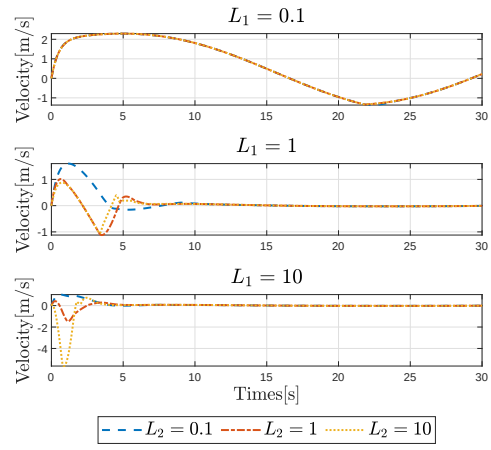

(d) $\hat{w}_{f_2}$ **estimation error.**

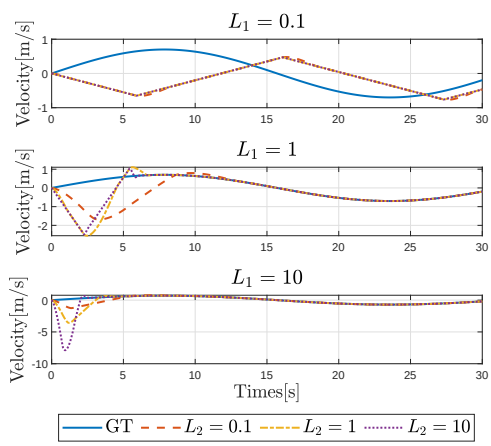

(e) $\hat{w}_{h_2}$.

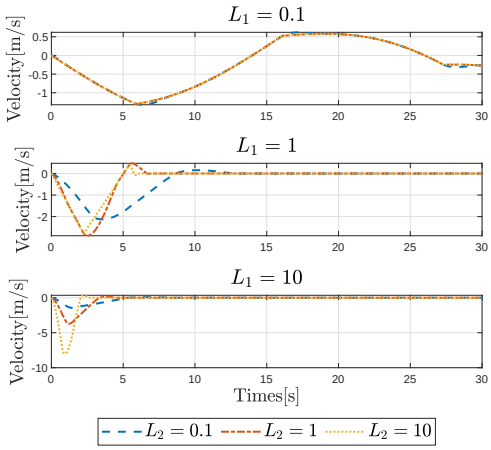

(f) $\hat{w}_{h_2}$ **estimation error.**

Figure 6.4: The influence of different observer gains, L_1 and L_2, on wind velocity estimation $\hat{\mathbf{V}}_{w_2}$.

doi:10.6342/NTU202500345

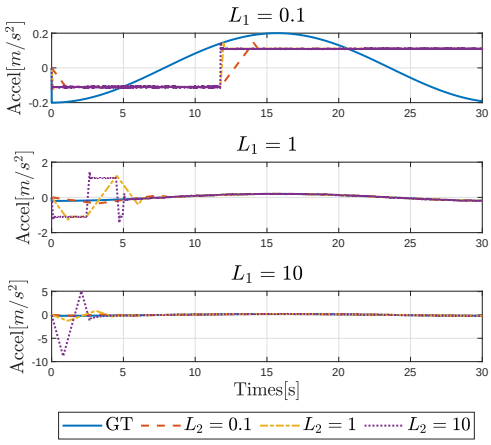

(a) $\hat{a}_l$.

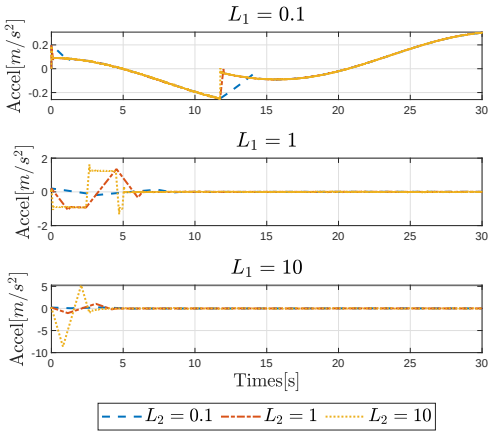

(b) $\hat{a}_l$ estimation error.

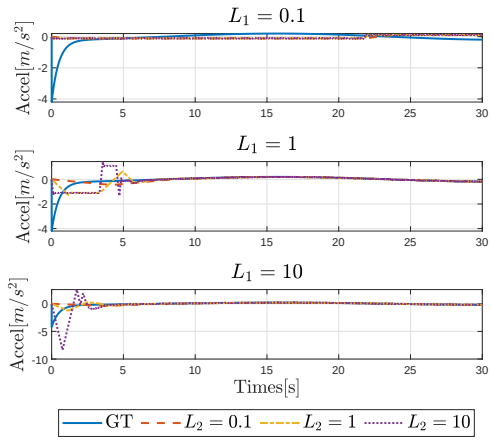

(c) $\hat{a}_f$.

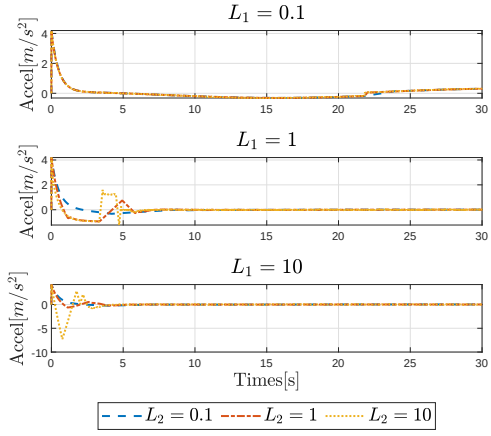

(d) $\hat{a}_f$ estimation error.

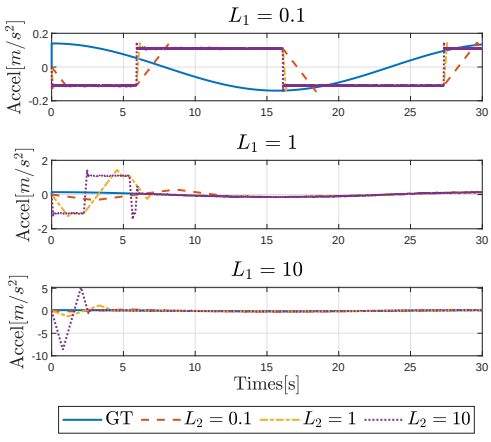

(e) $\hat{a}_h$.

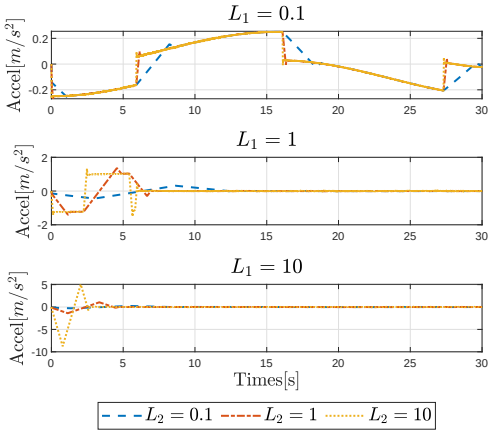

(f) $\hat{a}_h$ estimation error.

Figure 6.5: The influence of different observer gains, L_1 and L_2, on wind acceleration estimation $\hat{\mathbf{V}}_{w_a}$.

doi:10.6342/NTU202500345

Table 6.5: The LBFC gains and SMWO gains for the LBFC-SMWO performance evaluation.

Parameter	c_1	c_2	c_3	c_4	c_5	c_6
Value	0.2	0.2	1.0	0.4	0.4	3.0
Parameter	L_1	L_2				
Value	1.0	0.1				

in x-y plane of the inertial frame $\{I\}$ with a constant ground speed $V_L = 18$m/s and ascending speed $V_{L_v} = -1$m/s. The virtual leader's trajectory can be expressed as

$$\mathbf{p}_L(t) = \begin{bmatrix} V_{L_h}\cos(\frac{\pi}{4})t & V_{L_h}\sin(\frac{\pi}{4})t & -90 + V_{L_v}t \end{bmatrix}^\top, \quad t \in [0, t_f]s, \tag{6.7}$$

where $t_f = 70$. The initial conditions of the virtual leader and the follower are listed in Table 6.6 and Figure 6.6 shows the schematic of the straight line formation flight.

Table 6.6: The initial conditions of the leader and the follower for LBFC-SMWO performance evaluation in straight line trajectory.

Parameter	**Value**	**Parameter**	**Value**	**Unit**
x_{L_0}	0	x_{F_0}	-10	m
y_{L_0}	0	y_{F_0}	-10	m
z_{L_0}	-90	z_{F_0}	-80	m
V_{L_0}	18	V_{F_0}	18	m/s
ϕ_{L_0}	0	ϕ_{F_0}	0	rad
γ_{L_0}	0.055	θ_{F_0}	0	rad
χ_{L_0}	$\frac{\pi}{4}$	ψ_{F_0}	0	rad

To better unstanding how much influence of different wind profiles may have on the formation flight performance, two situations, with wind and without wind are discussed. Firstly, we compared the LBFC performance with wind compensation and without wind compensation even under no wind environment. Secondly, under wind environment, different cases of the wind settings including wind direction, constant wind magnitude, wind property and whether applying wind compensation or not are considered. All the cases are listed in Table 6.7.

doi:10.6342/NTU202500345

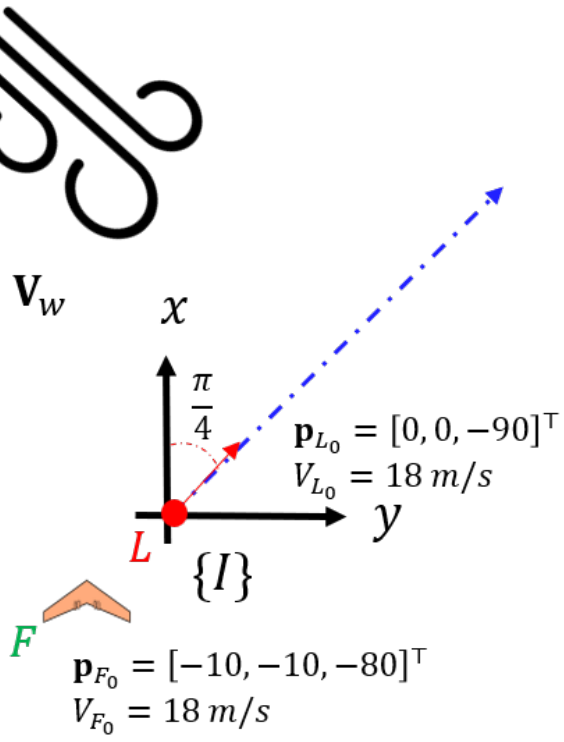

Figure 6.6: The schematic of the straight line formation flight.

Table 6.7: The cases of the different wind settings for formation flight performance evaluation.

	Environment	Wind			
		Direction	$\mathbf{V}_{w_{sc}}$ Magnitude	Property	Compensation
Cases	w/o wind	-	-	-	Cx
		-	-	-	Cv
	w/ wind	D+135	M2	Pc	Cx
		D-135	M8	Ps	Cv

doi:10.6342/NTU202500345

In Table 6.7, D means the wind direction, D+135 means the wind direction is 135 degrees in inertial frame $\{I\}$; M means the wind magnitude, M2 means the wind magnitude of the steady constant wind $\mathbf{V}_{w_{sc}}$ is 2 m/s; P means the wind property, Pc means the wind profile is only steady constant wind $\mathbf{V}_{w_{sc}}$ and Ps means the wind profile contains both steady constant wind $\mathbf{V}_{w_{sc}}$ and sinusoidal wind $\mathbf{V}_{w_{ss}}$; C means the compensation, Cv means the wind compensation is turned on and Cx means the wind compensation is turned off. For example, the case with a steady constant wind blowing to the direction of 135 degrees in inertial frame $\{I\}$ with a magnitude of 2 m/s and wind compensation on will be represented as D+135M2PcCv.

The trajectory of the straight line formation flight under no wind environment is shown in Figure 6.7. Figure 6.8 shows the formation error comparison between with wind compensation and without wind compensation. From Figure 6.8, under no wind environment, the formation error converges in 20 s in both cases. However, the case with wind compensation has larger error value than without wind compensation instead. This situation can be also observed from the states and states error in Figure 6.9.

In Figure 6.9(d), the states error of θ_e^d and $V_{a_e}^d$ have an undesired overshoot and undershoot compared to the case without wind compensation in Figure 6.9(b), which may result from the transient state of the wind velocity estimation and the wind acceleration estimation. In Figure 6.10, the wind estimation takes around 10 s to converge to the ground truth value, which induced the larger states error and formation error in the transient states.

For the formation flight of the straight line trajectory under the wind environment, we want to discuss how the different wind settings would pose influence on the formation

doi:10.6342/NTU202500345

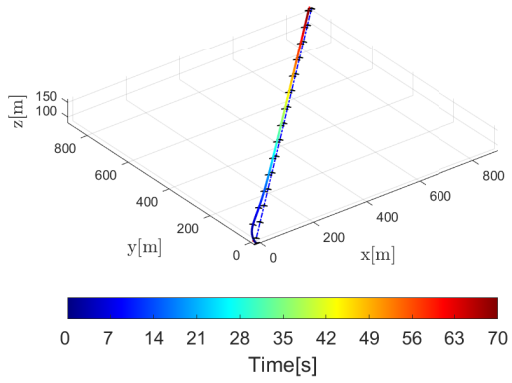

(a) Without wind compensation.

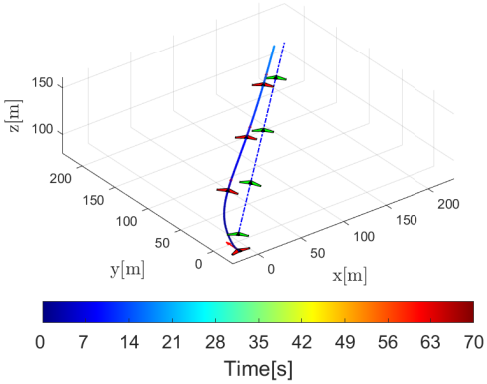

(b) Without wind compensation. Zoom in transient state.

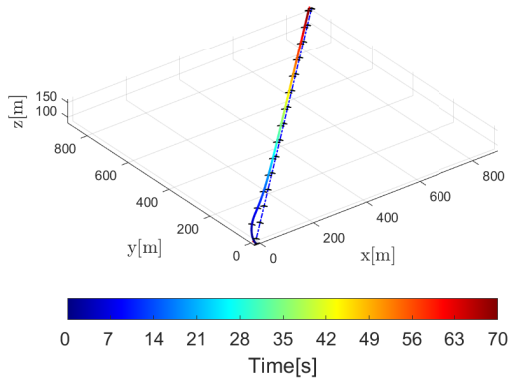

(c) With wind compensation.

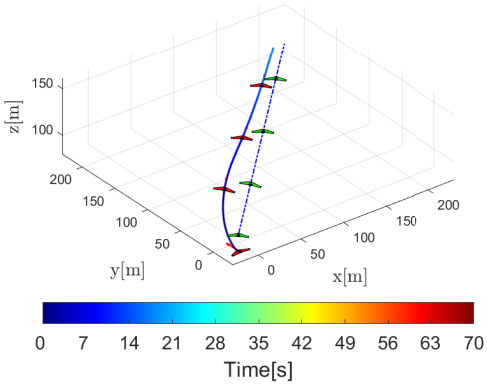

(d) With wind compensation. Zoom in transient state.

Figure 6.7: The 3D visualization of the straight line trajectory of the formation flight under no wind environment. The green fixed-wing UAV represents the leader and the red fixed-wing UAV represents the follower, which are plotted out each 5 seconds. The blue dot-dashed line represents the referenced trajectory of the leader. The red arrow means the airspeed direction of the follower.

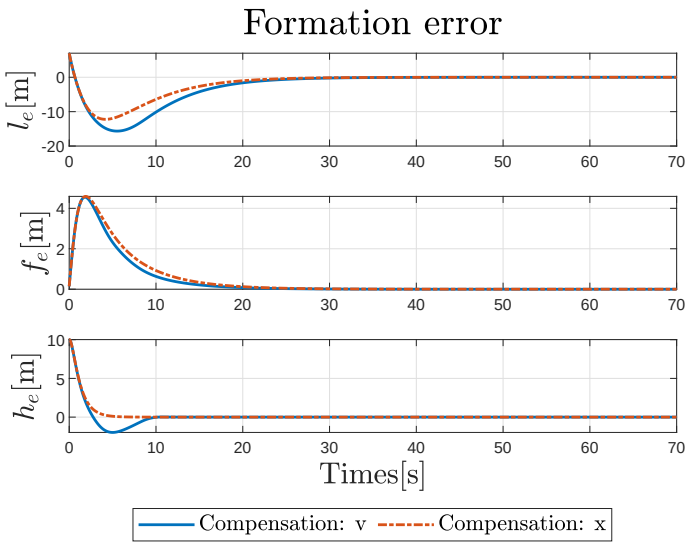

Figure 6.8: The comparison of the formation error between the case with wind compensation and without wind compensation under no wind environment.

doi:10.6342/NTU202500345

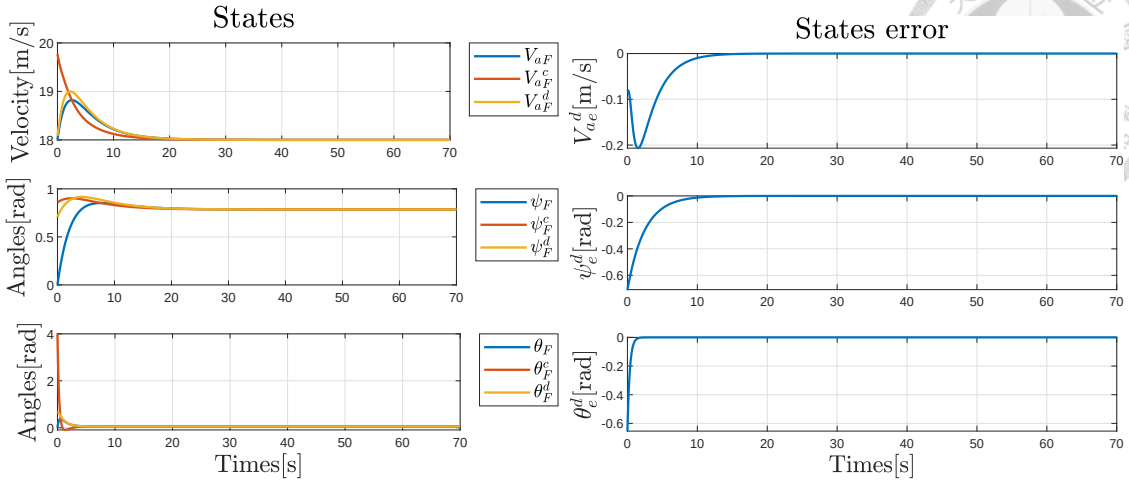

(a) The states, the commanded inputs and the desired states without wind compensation.

(b) The states error under the case without wind compensation.

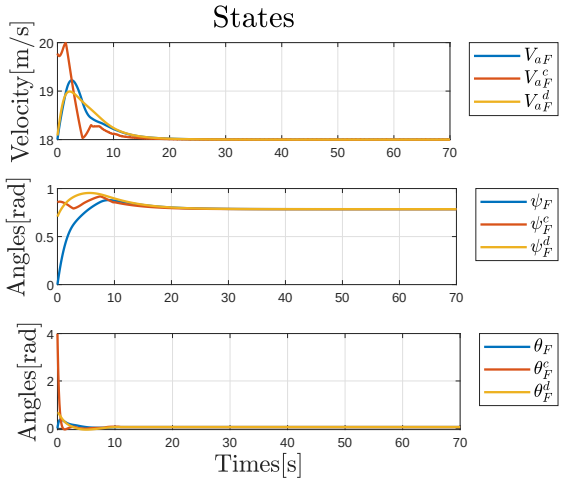

(c) The states, the commanded inputs and the desired states with wind compensation.

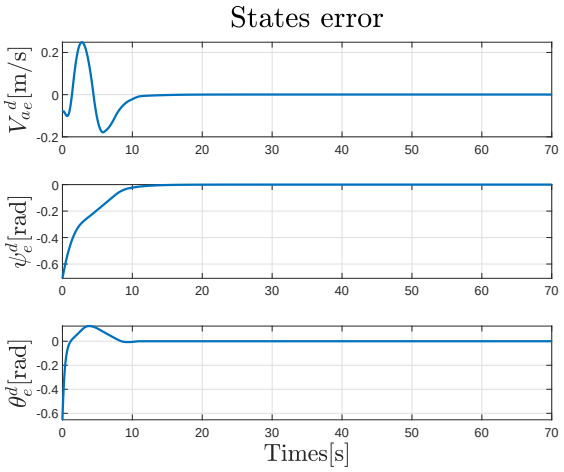

(d) The states error under the case with wind compensation.

Figure 6.9: The states and states error of the follower UAV of the straight line formation trajectory under no wind environment.

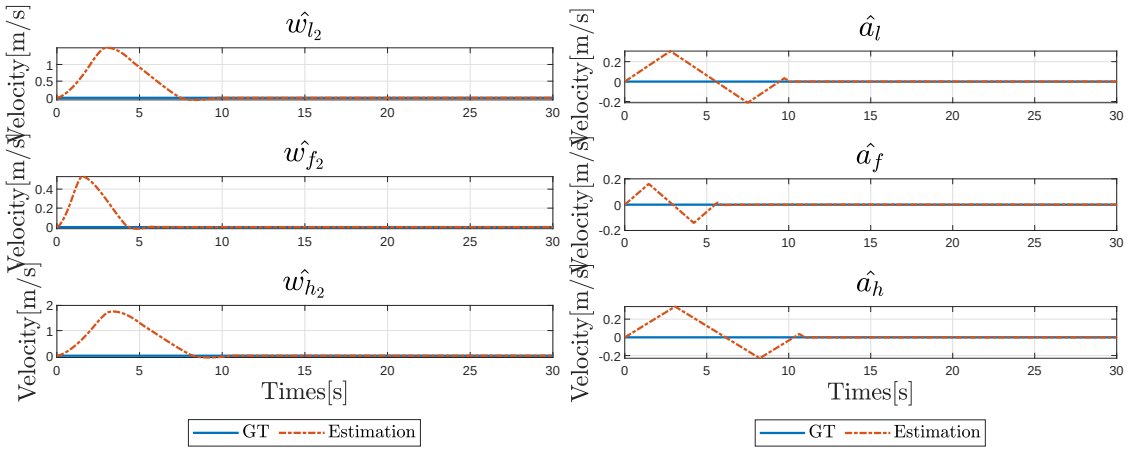

(a) Wind velocity estimation.

(b) Wind acceleration estimation.

Figure 6.10: The wind estimations under no wind environment. Zoom in the first 30 s.

doi:10.6342/NTU202500345

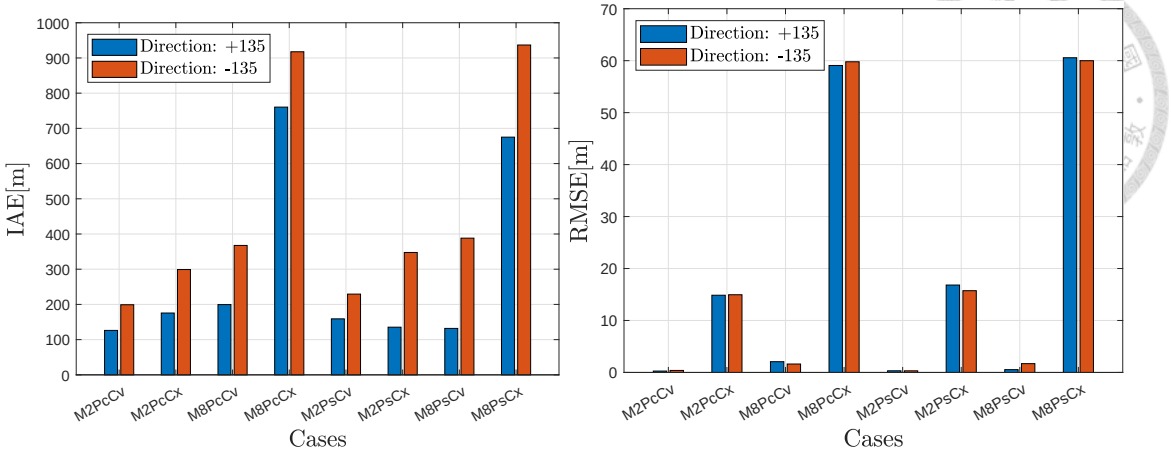

(a) The IAE. **(b) The RMSE.**

Figure 6.11: The comparison of the formation flight of the IAE and RMSE under different wind directions.

flight performance, which is evaluated by IAE and RMSE. The transient state is from 0 s to 20 s, i.e., $t_r = 20$, which is selected manually, and the steady state is from 20 s to 70 s, i.e., $t_f = 70$.

First of all, different wind directions, D+135 and D-135, are considered. Figure 6.11 shows the results of the IAE and RMSE of the formation flight. In Figure 6.11(a), all the cases with D+135 has a smaller IAE than the cases with D-135. This is because the virtual leader is flying to the direction of $\frac{\pi}{4}$ radians in the inertial frame $\{I\}$ and D+135 will benefit the follower to follow the virtual leader. Conversely, the D-135 degrees will hinder the follower to follow the virtual leader. The influence of the different wind direction will fade out after entering the steady state. Figure 6.11(b) shows that the RMSE in no matter D+135 or D-135 cases are pretty much the same.

Second of all, the different wind magnitudes, M2 and M8, are considered. From Figure 6.12, both the IAE and RMSE of the cases with M2 are smaller than the cases with M8. This is trivial for the cases without the wind compensation, but for the cases with wind compensation, D135PcCv, D135PsCv, D-135PcCv, and D-135PsCv, in Figure

doi:10.6342/NTU202500345

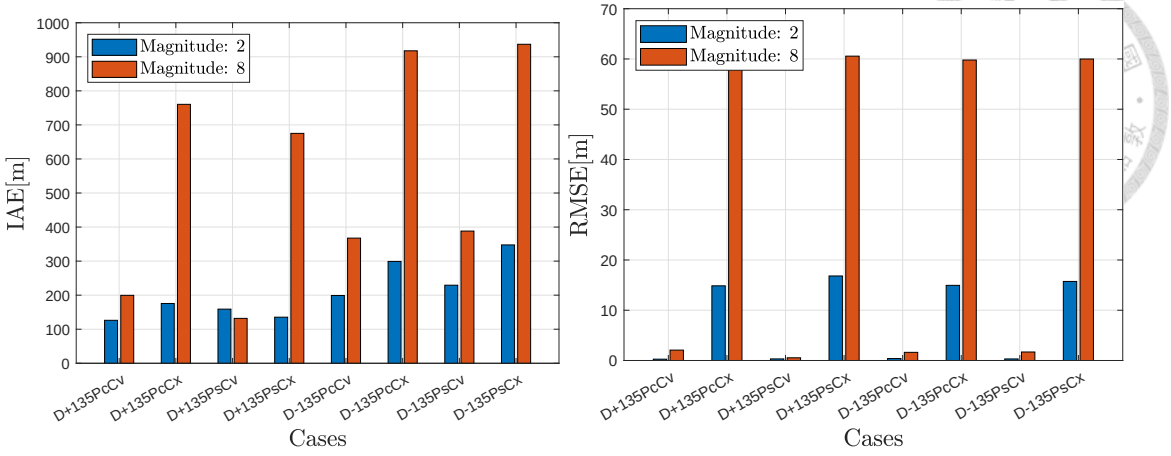

(a) The IAE. **(b) The RMSE.**

Figure 6.12: The comparison of the formation flight of the IAE and RMSE under different wind magnitude.

6.12(b) show that the RMSE can be tremendously reduced by the wind compensation in both M2 and M8 cases.

Thirdly, the different wind properties, Pc and Ps, are considered. The results of the IAE and RMSE are shown in Figure 6.13. In Figure 6.13(a), the difference of the influences from Pc or Ps cannot be discriminated. As for the RMSE, the cases D+135M2Cx, D+135M8Cx, D-135M2Cx, and D-135M8Cx, in Figure 6.13(b) show that the cases with Ps have larger RMSE than the cases with Pc. However, under the wind compensation cases D+135M2PcCv, D+135M8PcCv, D-135M2PcCv, and D-135M8PcCv, the RMSE can be a lot reduced for both Pc and Ps cases and the difference between Pc and Ps cases are not that significant. Here a brief conclusion can be drawn that with the LBFC-SMWO, the formation error can be reduced under the time-variant or time-invariant wind environment.

Lastly, the influence of whether with wind compensation or not is discussed. Figure 6.14 shows that both the IAE and RMSE are dramatically reduced by the wind compensation when the wind magnitude is 8. However, when the wind magnitude is 2,i.e.,

doi:10.6342/NTU202500345

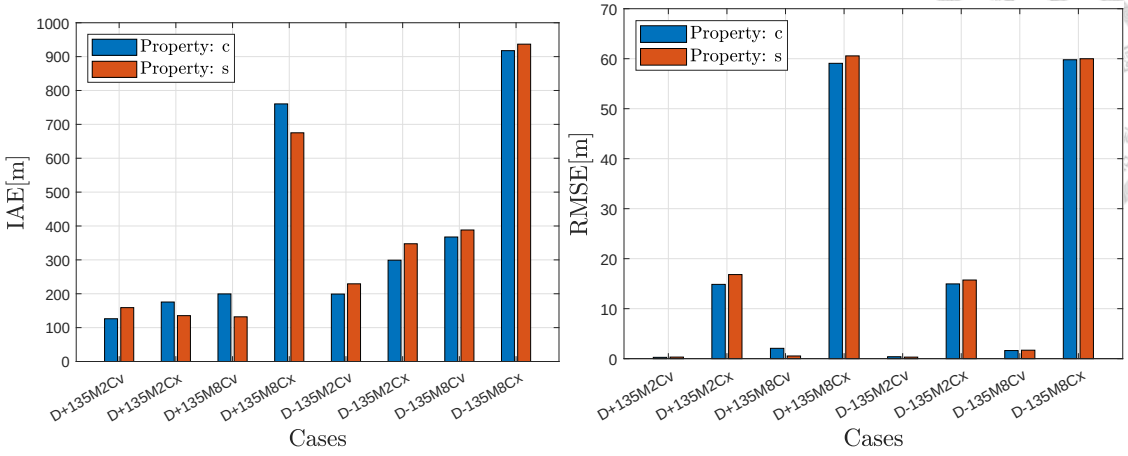

(a) The IAE. **(b) The RMSE.**

Figure 6.13: The comparison of the formation flight of the IAE and RMSE under different wind property.

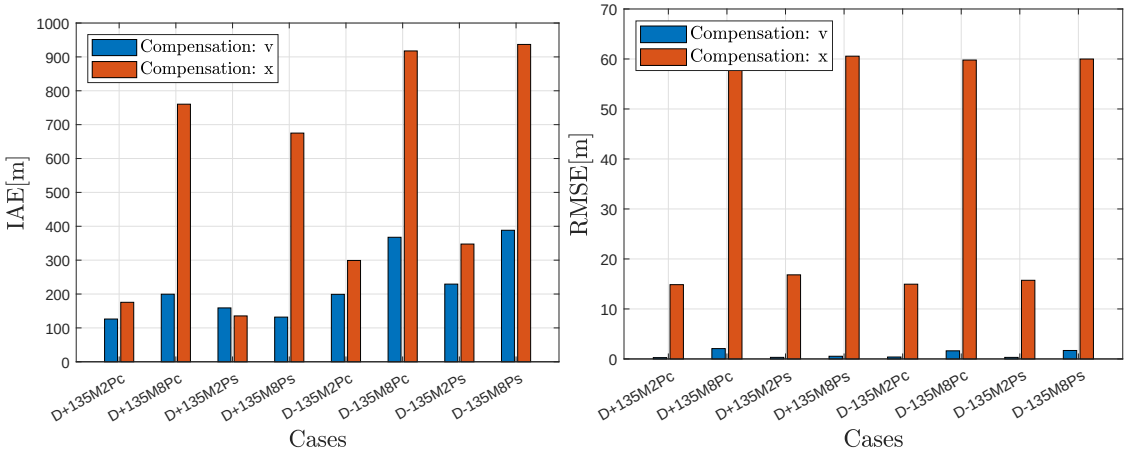

(a) The IAE. **(b) The RMSE.**

Figure 6.14: The comparison of the formation flight of the IAE and RMSE under whether with wind compensation.

D+135M2Ps in Figure 6.14(a), the IAE will be a lot affected by the compensation of the transient states of the wind estimation, causing the error under the wind compensation is larger than without wind compensation instead. The results of the straight line formation flight performance evaluation from IAE and RMSE under different wind settings are listed in Table 6.8.

6.2.2.2 Formation Flight in Circular Orbit Trajectory

In the circular orbit formation flight, the virtual leader flies in a circular orbit tra-

doi:10.6342/NTU202500345

Table 6.8: The results of the formation flight performance evaluation under different wind settings in the straight line trajectory. The RMSE is calculated from the squared root of the sum of the squared of the RMSE_le, RMSE_fe, and RMSE_he.

Wind	Dir.	135			
	Prop.	c			
	Mag.	2		8	
	Com.	v	x	v	x
Cases		D+135M2PcCv	D+135M2PcCx	D+135M8PcCv	D+135M8PcCx
IAE		**126.2011**	175.5890	**199.5060**	760.4023
RMSE		**0.2651**	14.8597	**2.0686**	59.0756
RMSE_le		**0.2631**	14.8591	**2.0676**	59.0486
RMSE_fe		**0.0327**	0.1325	**0.0654**	1.7849
RMSE_he		**0.0003**	0.0077	**0.0041**	0.0952
Wind	Dir.	135			
	Prop.	s			
	Mag.	2		8	
	Com.	v	x	v	x
Cases		D+135M2PsCv	D+135M2PsCx	D+135M8PsCv	D+135M8PsCx
IAE		159.0133	**135.3816**	**131.8863**	675.0948
RMSE		**0.3157**	16.8203	**0.5371**	60.5621
RMSE_le		**0.3147**	16.8066	**0.5369**	60.5313
RMSE_fe		**0.0256**	0.1924	**0.0144**	1.8081
RMSE_he		**0.0010**	0.6519	**0.0008**	0.6769
Wind	Dir.	-135			
	Prop.	c			
	Mag.	2		8	
	Com.	v	x	v	x
Cases		D-135M2PcCv	D-135M2PcCx	D-135M8PcCv	D-135M8PcCx
IAE		**199.0827**	299.0857	**367.5379**	917.5854
RMSE		**0.3868**	14.9530	**1.6221**	59.7878
RMSE_le		0.3843	**0.2186**	0.4525	**0.2139**
RMSE_fe		**0.0434**	14.9514	**1.5577**	59.7873
RMSE_he		**0.0002**	0.0433	**0.0065**	0.1338
Wind	Dir.	-135			
	Prop.	s			
	Mag.	2		8	
	Com.	v	x	v	x
Cases		D-135M2PsCv	D-135M2PsCx	D-135M8PsCv	D-135M8PsCx
IAE		**229.2925**	347.5453	**388.2147**	936.7830
RMSE		**0.3105**	15.7312	**1.6926**	59.9923
RMSE_le		**0.3098**	4.8118	**0.4501**	4.8335
RMSE_fe		**0.0208**	14.9625	**1.6317**	59.7931
RMSE_he		**0.0010**	0.6652	**0.0033**	0.7002

doi:10.6342/NTU202500345

jectory with a radius of R, a ascending speed $V_{L_v} = -1$ m/s and the ground speed $V_g = 18$ m/s. The virtual leader's trajectory can be expressed as

$$\mathbf{p}_L(t) = \begin{bmatrix} R\cos(\omega t) & R\sin(\omega t) & -90 + V_{L_v} t \end{bmatrix}^\top, \quad t \in [0, t_f]s, \tag{6.8}$$

where $\omega = \frac{V_{L_h}}{R}$ is the angular velocity and $t_f = 100$. The initial conditions of the virtual leader and the follower are listed in Table 6.9 and Figure 6.15 shows the schematic of the circular orbit formation flight.

Table 6.9: The initial conditions of the leader and the follower for LBFC performance evaluation in the circular orbit trajectory.

Parameter	Value	Parameter	Value	Unit
x_{L_0}	R	x_{F_0}	0	m
y_{L_0}	0	y_{F_0}	0	m
z_{L_0}	-90	z_{F_0}	-90	m
V_{L_0}	18	V_{F_0}	18	m/s
ϕ_{L_0}	0	ϕ_{F_0}	0	rad
γ_{L_0}	0.055	θ_{F_0}	0	rad
χ_{L_0}	$\pi/2$	ψ_{F_0}	0	rad

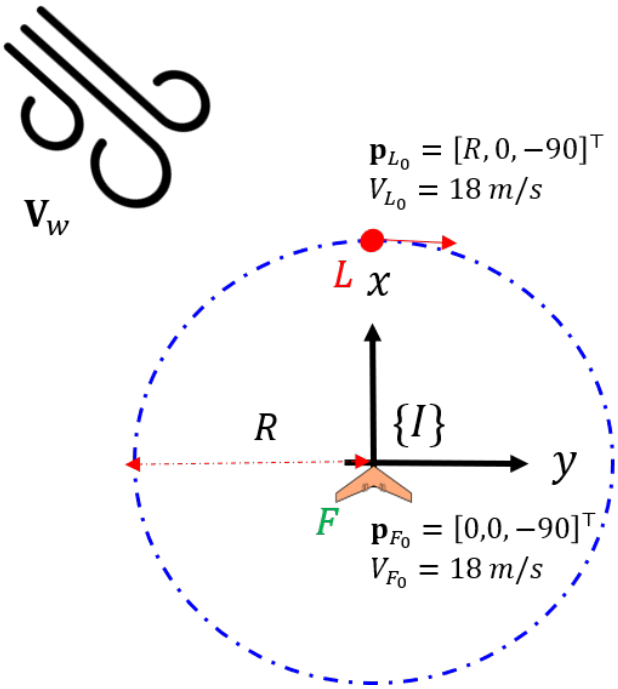

Figure 6.15: The schematic of the circular orbit formation flight.

doi:10.6342/NTU202500345

In the circular orbit formation flight, different orbit radius R are considered to evaluate the performance of the LBFC-SMWO under a fixed wind direction, magnitude, and property. The cases of the different orbit radius for evaluation are listed in Table 6.10. In

Table 6.10: The cases of the different orbit radius for formation flight performance evaluation in the circular orbit trajectory.

	Radius	Wind			
		Direction	Magnitude	Property	Compensation
Cases	R50	D+135	M2	Ps	Cx
	R200				
	R300				Cv

Table 6.10, R means the radius of the circular orbit, R50 means the radius of the circular orbit is 50 m, and the other definition of the wind settings are the same as in Table 6.7.

The formation error of the cases for R50Cx and R50Cv are shown in Figure 6.16. For the lateral error l_e and forward error f_e, both cases do not converge to zero in the steady state, which can be revealed by the unconverging wind estimation in Figure 6.17. This

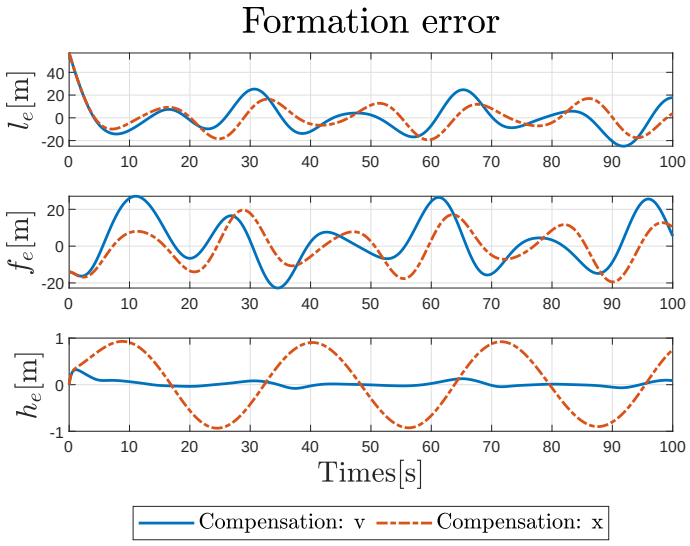

Figure 6.16: The formation error of the circular orbit formation flight with the radius of 50 m.

is due to the fact that the derivative of the wind velocity and acceleration in geometry frame $\{G\}$ will be larger when the trajectory radius is smaller, which will need larger observer gains to catch up the variation. On the other hand, the vertical component of

doi:10.6342/NTU202500345

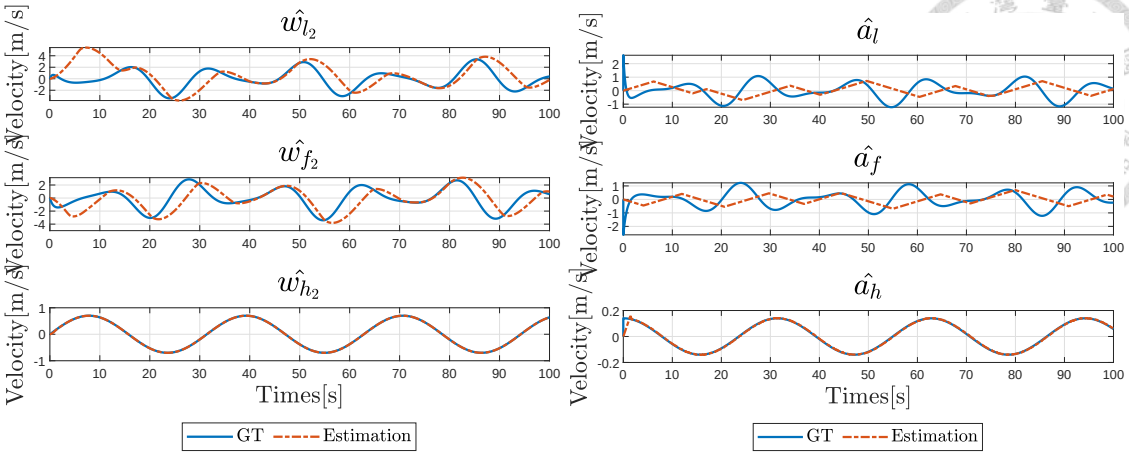

(a) The wind velocity estimation. **(b) The wind acceleration estimation.**

Figure 6.17: The wind estimations of the circular orbit formation flight with the radius of 50 m. The groundtruth wind is in the geometry frame $\{G\}$.

the wind will not be affected along with the trajectory radius, which is why the vertical error h_e converges to zero in R50Cv but not in R50Cx. For cases R200 and R300, the wind estimation all catch up the rate of the variation of the ground truth wind as shown in Figure 6.18 due to the large enough trajectory radius.

The formation flight trajecotories of the cases R200 and R300 are shown in Figure 6.19. It is worth noting that the follower UAV almost collides with the leader UAV at around 15 s and 10 s in Figure 6.19(a), Figure 6.19(c) and Figure 6.19(b), Figure 6.19(d). This is an inter-agent collision problem which is not considered in this work; however, it should be carefully dealt with in the future. The formation error of the cases R200 and R300 are shown in Figure 6.20, which shows that the influence of the wind is still mitigated by the compensation when entering the steady state as discussed in the straight line trajectory cases. However, due to the larger intial formation error, the error in the transient state is enhanced by the transient state of the wind estimation, which can be also revealed by the first 40 s from Figure 6.19(b) and Figure 6.19(d). The results of the circular orbit formation flight performance evaluation from IAE and RMSE under different orbit radius are listed in Table 6.11.

doi:10.6342/NTU202500345

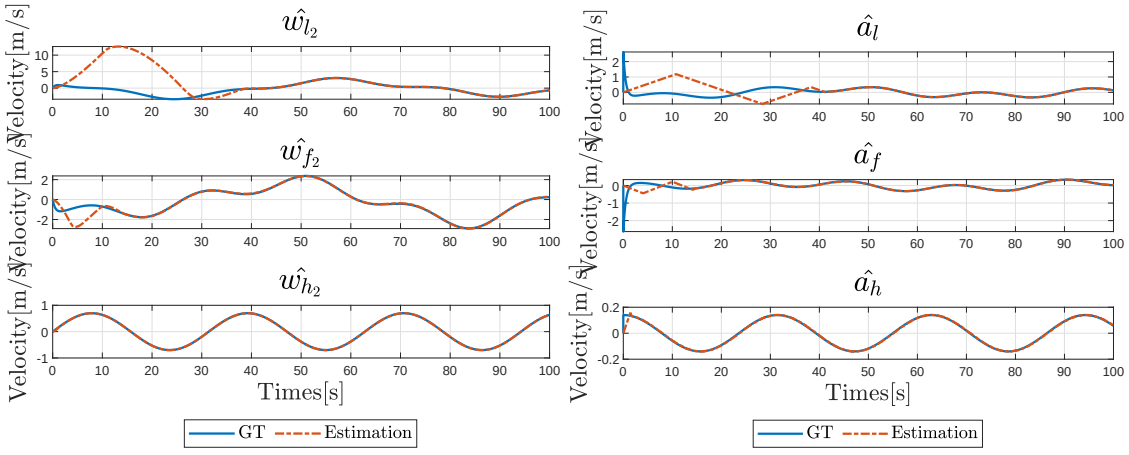

(a) The wind velocity estimation (R200).

(b) The wind acceleration estimation (R200).

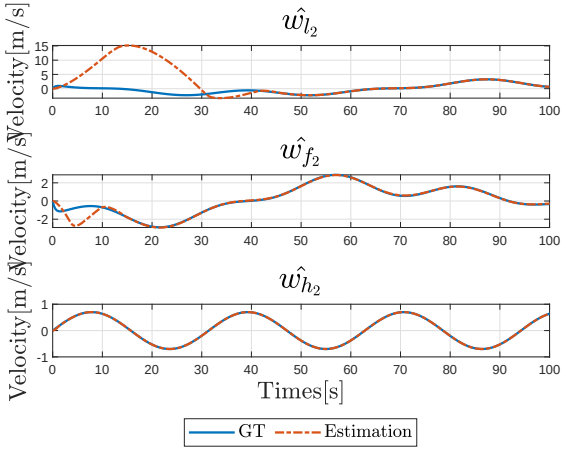

(c) The wind velocity estimation (R300).

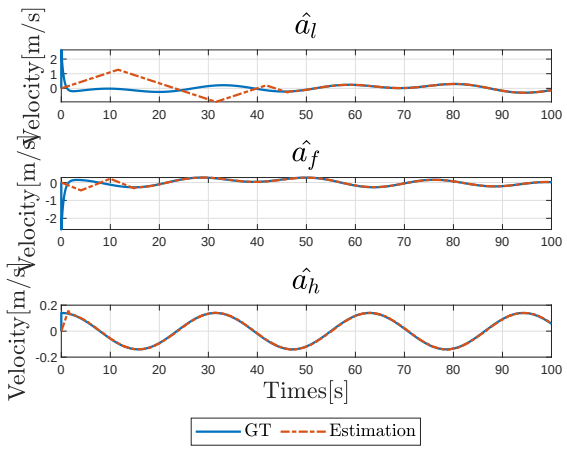

(d) The wind acceleration estimation (R300).

Figure 6.18: The wind estimations of the circular orbit formation flight with the radius of 200 m and 300 m. The groundtruth wind is in the geometry frame $\{G\}$.

doi:10.6342/NTU202500345

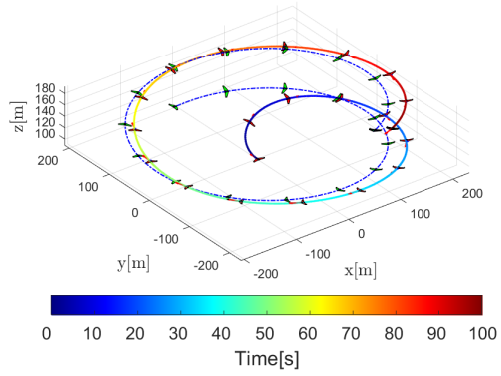

(a) Without wind compensation (R200).

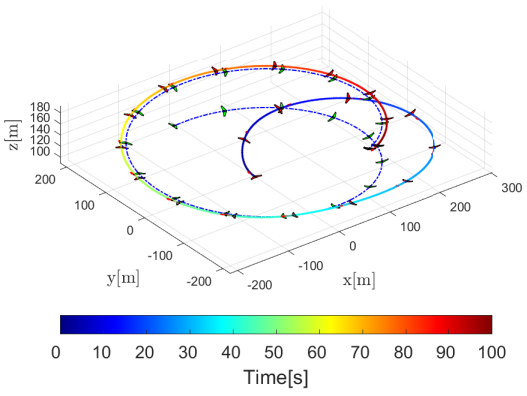

(b) With wind compensation (R200).

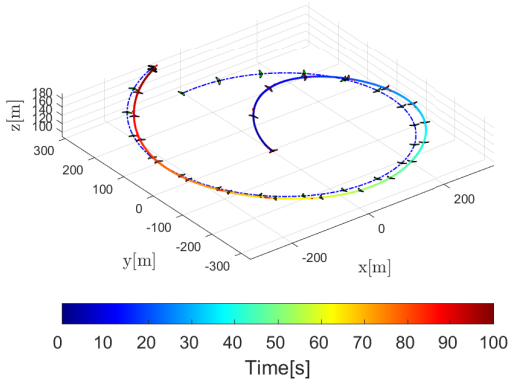

(c) Without wind compensation (R300).

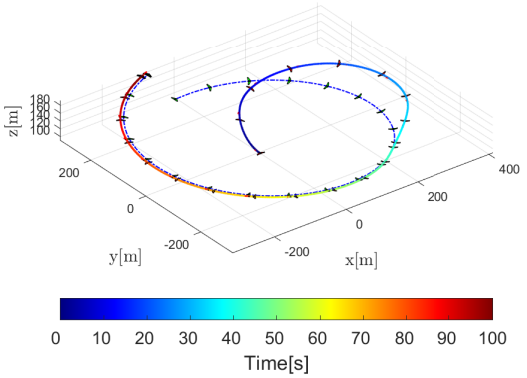

(d) With wind compensation (R300).

Figure 6.19: The trajectory of the circular orbit formation flight with the radius of 200 m and 300 m.

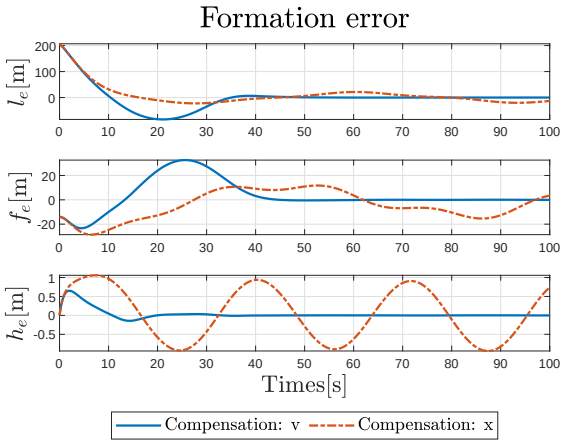

(a) The formation error of the circular orbit formation flight with the radius of 200 m.

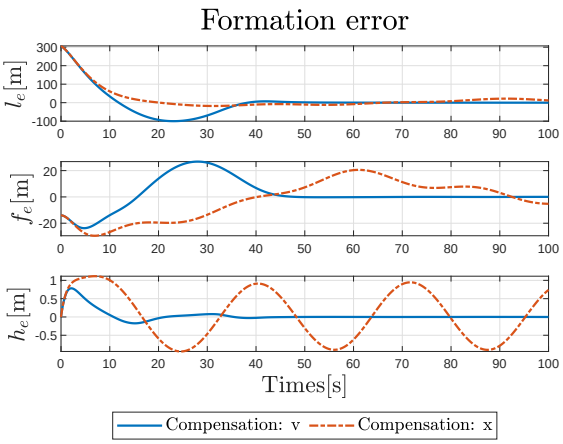

(b) The formation error of the circular orbit formation flight with the radius of 300 m.

Figure 6.20: The formation error of the circular orbit formation flight with the radius of 200 m and 300 m.

doi:10.6342/NTU202500345

Table 6.11: The results of the formation flight performance evaluation under different orbit radius in the circular orbit trajectory. The RMSE is calculated from the squared root of the sum of the squared of the RMSE_le, RMSE_fe, and RMSE_he.

Rad.	50		200		300	
Com.	v	x	v	x	v	x
Cases	R50Cv	R50Cx	R200Cv	R200Cx	R300Cv	R300Cx
IAE	783.5661	**635.3324**	2588.3270	**1796.7158**	3584.8097	**2605.7188**
RMSE	16.7882	**13.9664**	**1.4585**	15.8050	**2.3618**	15.8937
RMSE_le	11.6894	**9.8608**	**1.3831**	12.9451	**2.0969**	11.8227
RMSE_fe	12.0499	**9.8701**	**0.4630**	9.0451	**1.0869**	10.6033
RMSE_he	**0.0466**	0.6358	**0.0013**	0.6383	**0.0040**	0.6353

6.3 SITL Simulation

In the software-in-the-loop (SITL) simulation, a more realistic simulation environment including the sensor noises, control saturations, and the information exchanges delay will be included to evaluate the performance of the LBFC-SMWO. An open-source PX4 simulation package [43: GazeboSimulation 2024] is adopted to provide the off-the-shelf SITL environment. The innerloop controller in SITL is ran by the customized PX4 autopilot v1.15 [1] [44: Autopilot 2024], [19: Meier *et al.* 2015], while the Gazebo sim Garden [45: GazeboGarden 2024] is used as a physical simulator to simulate the fixed-wing UAV dynamics and a ground control station (GCS) QGroundControl [46: QGC 2024] is used to monitor the UAV's states. The overall SITL simulation architecture is shown in Figure 6.21. The PX4 autopilot also provides upper level API to control the vehicle's attitude, however, only θ and ϕ can be controlled in fixed-wing airframe. As a result, in order to meet the LBFC requirements, a ψ controller is designed with P control based on Assumption 2 by utilizing the built-in ϕ controller. On the other hand, the PX4 autopilot calculates the airspeed value by Bernoulli's equation [47: Wikipedia 2024]; however, in the simulation, it does not adopt the real wind value to calculate the accurate differential

[1] The customized PX4 autopilot is available at https://github.com/TigerWuu/Formation-PX4

doi:10.6342/NTU202500345

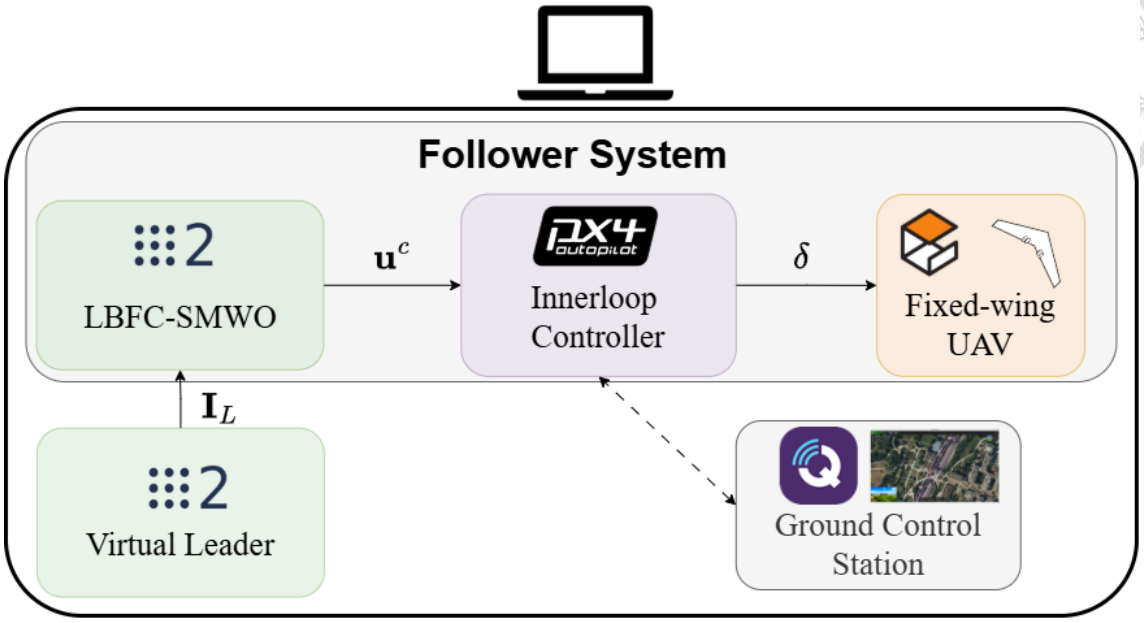

Figure 6.21: The overall SITL simulation architecture.

pressure and uses the x-axis velocity in the fixed-wing body frame instead. This problem is also solved in the customized PX4 autopilot [2] to obtain a more accurate wind estimation value. The wind profile in the Gazebo sim is generated from the customized wind plugin [3] modified from *wind_effect* plugin in [48: Gazebosim 2024].

The proposed LBFC-SMWO algorithm [4] is implemented in C++ and the information exchange between the algorithms and PX4 autopilot is organized through ROS2 humble [49: ROS2 2024] and μXRCE−DDS protocol. The whole SITL simulation are ran on the desktop computer equipped with Intel i9-11900K CPU and Nvidia RTX 2060 GPU. The information flow chart of the implemented LBFC-SMWO algorithm and PX4 autopilot are shown in Figure 6.22.

6.3.1 Fixed-wing System Overview

[2]The airspeed sensing problem has been issued and concretely described in https://github.com/PX4/PX4-Autopilot/issues/23756

[3]The customized wind plugin will publish the true wind value into ROS2 topic. It is for better visualizing the estimation results.

[4]The proposed LBFC-SMWO source code is available at https:// github.com/ TigerWuu/ PX4_formation_sim

doi:10.6342/NTU202500345

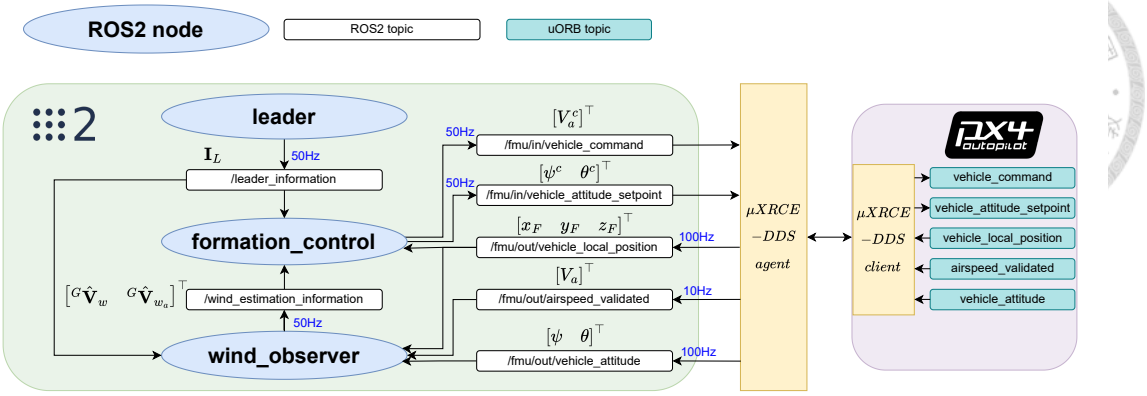

Figure 6.22: The information flow chart of the implemented LBFC-SMWO algorithm and PX4 autopilot in SITL simulation. *uORB* is a publish-subscribe message API implemented in PX4 autopilot for the information exchange. The infomation transmission frequency is also shown in the figure.

The selected airframe is *Standard VTOL* [50: GazeboVehicles 2024], however, only fixed-wing mode will be used for the LBFC-SMWO performance evaluation. The limitation of the V_a, ψ, θ are as follows:

- 12 m/s $\leq V_a \leq 28$ m/s
- $-\pi$ rad $\leq \psi \leq \pi$ rad
- $-\frac{1}{6}$ rad $\leq \theta \leq \frac{1}{6}$ rad

From Equation (5.18), the inverse time constant τ_{V_a}, τ_ψ, and τ_θ are necessary for the LBFC algorithm, whereas the inverse time constant of the innerloop system in SITL cannot be obtained directly. As a result, we collect the step response data of the V_a, ψ, θ innerloop systems from SITL simulation first, which is shown in Figure 6.23 and then do the time-domain system identification through the MATLAB function *tfest* [51: MathWorks 2022] with 1 pole and 0 zero. The identified transfer functions of the innerloop system are shown in Equation (6.9).

$$G_{V_a} = \frac{0.1861}{s + 0.1918}, \quad G_\psi = \frac{0.08939}{s + 0.08405}, \quad G_\theta = \frac{2.079}{s + 2.012}. \tag{6.9}$$

doi:10.6342/NTU202500345

The inverse time constant can be obtained through Equation (6.9) as $\tau_{V_a} = 0.1918$, $\tau_{\psi} = 0.08405$, and $\tau_{\theta} = 2.012$ [42: Dorf and Bishop 2017].

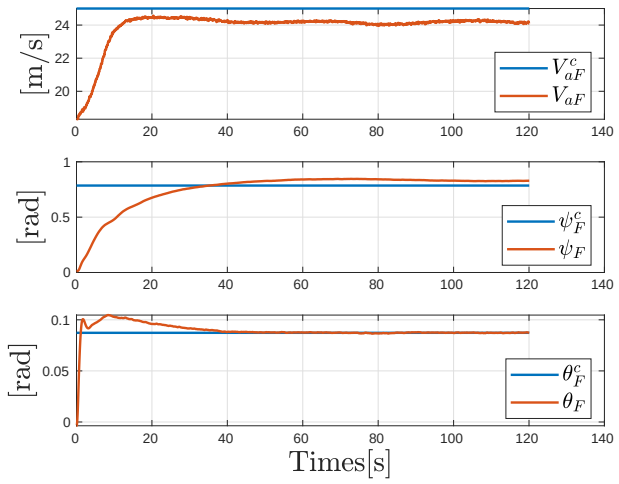

Figure 6.23: The step response of the innerloop system in SITL simulation.

6.3.2 Three UAVs Formation Flight

In the three UAVs formation flight, the simulation procedures will follow Figure 6.24. There are four timestamps in the simulation procedures:

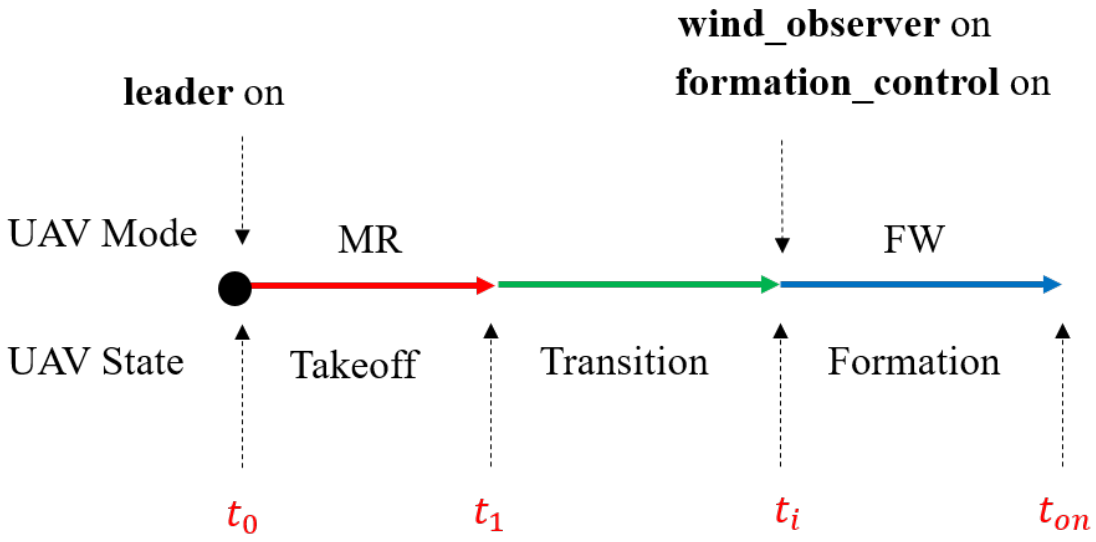

Figure 6.24: The simulation procedures of the formation flight in SITL simulation.

1. t_0: the virtual leader UAV starts to fly along with the desired trajectory and the

doi:10.6342/NTU202500345

follower UAVs start takeoff to 10 meters height above the ground in the multirotor (MR) mode.

2. t_1: The virtual leader UAV keeps flying and the follower UAVs start transition to the fixed-wing (FW) mode.

3. t_i: The virtual leader UAV keeps flying and the follower UAVs start to execute the formation flight.

4. t_{on}: The follower UAVs start to receive the wind estimation value to compensate the wind effect.

At t_0, the three UAVs are initialized on the ground as shown in Figure 6.25. F_1 are located at $\begin{bmatrix} 0 & 0 & 0 \end{bmatrix}^\top$, F_2 are located at $\begin{bmatrix} -3 & -3 & 0 \end{bmatrix}^\top$, and F_3 are located at $\begin{bmatrix} -3 & 3 & 0 \end{bmatrix}^\top$ in the inertial frame $\{I\}$.

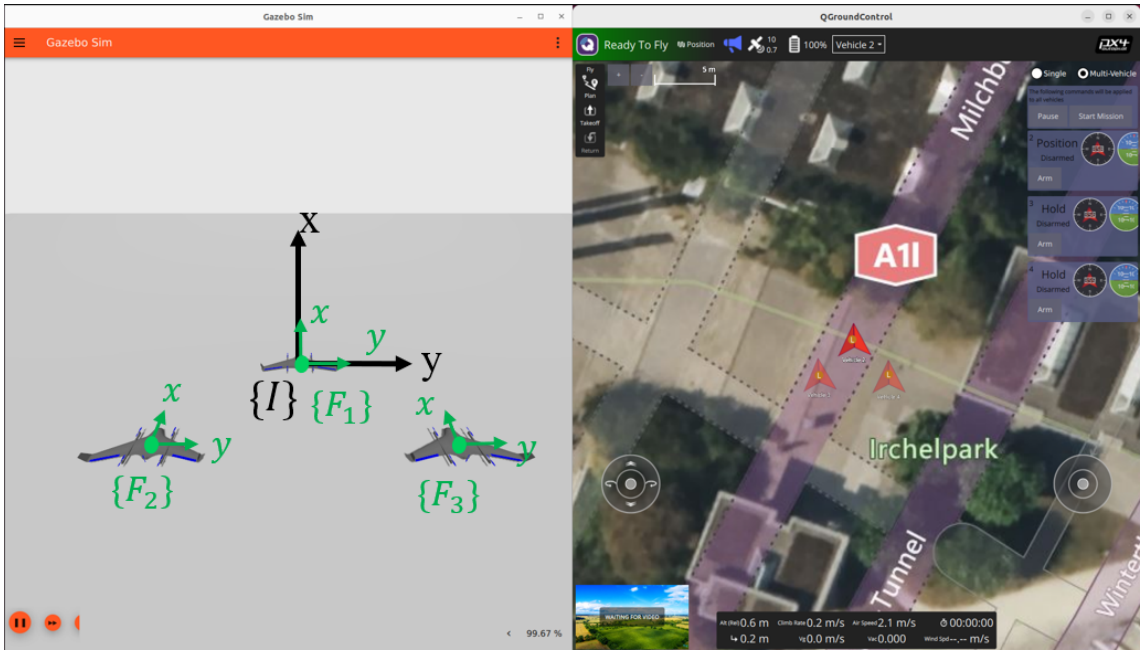

Figure 6.25: The initial conditions of the three UAVs at t_0.

At t_i, the follower UAVs has transitioned to the fixed-wing mode and start executing the formation flight. The initial airspeed $V_{aF_0} = 10$ m/s, the altitude $z_{F0} = -10$ m, and

doi:10.6342/NTU202500345

the heading angle $\psi_{F0} = \frac{\pi}{2}$ radians. The schematic of the formation flight at t_i is shown in Figure 6.26.

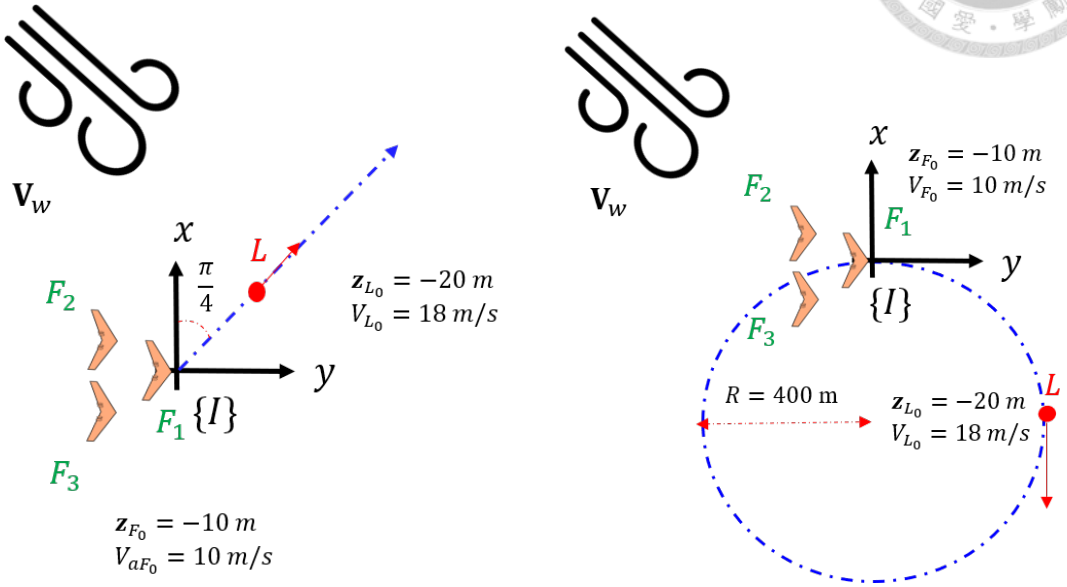

(a) The straight line formation flight at t_i. (b) The circular orbit formation flight at t_i.

Figure 6.26: The schematic of the three UAVs formation flight at t_i.

The steady wind profile of the constant wind $\mathbf{V}_{w_{sc}}$ and the sinusoidal wind $\mathbf{V}_{w_{ss}}$ generated from the wind plugin are

$$\begin{aligned} \mathbf{V}_w &= \mathbf{V}_{w_{sc}} + \mathbf{V}_{w_{ss}}, \\ \mathbf{V}_{w_{sc}} &= \begin{bmatrix} 2\cos(\frac{3\pi}{4}) & 2\sin(\frac{3\pi}{4}) & -0.7 \end{bmatrix}^\top, \\ \mathbf{V}_{w_{ss}} &= \begin{bmatrix} 1\sin(0.2t) & 1\sin(0.2t) & 0 \end{bmatrix}^\top. \end{aligned} \tag{6.10}$$

The desired formation configuration of the three UAVs is shown in Table 6.12.

Table 6.12: The desired formation configuration of the three UAVs in SITL simulation.

	l_c	f_c	h_c
F_1	0	0	0
F_2	-7	14	0
F_3	7	14	0

The controller and observer gains are listed in Table 6.13.

doi:10.6342/NTU202500345

Table 6.13: LBFC gains and SMWO gains for LBFC-SMWO performance evaluation

Parameter	c_1	c_2	c_3	c_4	c_5	c_6
Value	0.08	0.08	1.0	0.25	0.2	1.5
Parameter	L_1	L_2				
Value	1.0	0.1				

6.3.2.1 Straight Line Trajectory

In the straight line formation flight, the virtual leader fly straight along with $\frac{\pi}{4}$ radians in x-y plane of the inertial frame $\{I\}$ with a constant ground speed $V_L = 18$ m/s and constant altitude $z_L = -20$ m. The virtual leader's trajectory can be expressed as

$$\mathbf{p}_L(t) = \begin{bmatrix} V_L \cos(\frac{\pi}{4})t & V_L \sin(\frac{\pi}{4})t & -20 \end{bmatrix}^\top. \tag{6.11}$$

The formation trajectory of the three UAVs in the straight line formation flight is shown in Figure 6.27.

Figure 6.28 shows that the l_e is greatly reduced after the compensation of the wind estimation. In Figure 6.28(a), only the l_e oscillates around 50 m due to the wind influence. The wind estimation values and the groundtruth can be seen in Figure 6.29, which shows that only w_l is not zero because the wind direction is perpendicular to the flight direction. After the wind compensation, Figure 6.28(b) shows the l_e is mitigated, yet the oscillation still exists. Figure 6.30 also shows that the the states error starts to oscillates in high frequency after the wind compensation, however, ψ_e^d still does not converge to zero. Both the formation error and the states error do not converge to zero after the wind compensation may due to the modeling error, that is, the inverse time constant of the system identification is not that accurate or a time delay in the wind estimation value. Figure 6.29 shows that the wind estimation value is not exactly aligned with the groundtruth wind value, and this may result from the airspeed sensor is only 10 Hz, which is slower than the other sensors

doi:10.6342/NTU202500345

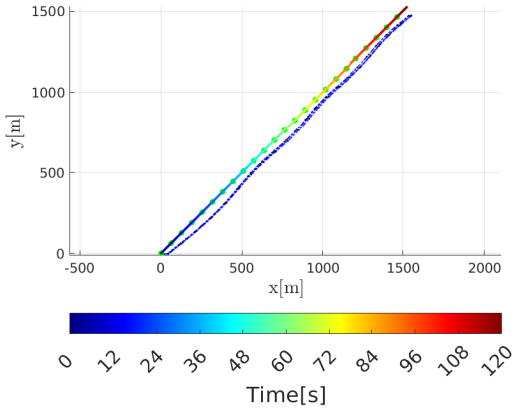

(a) Without wind compensation.

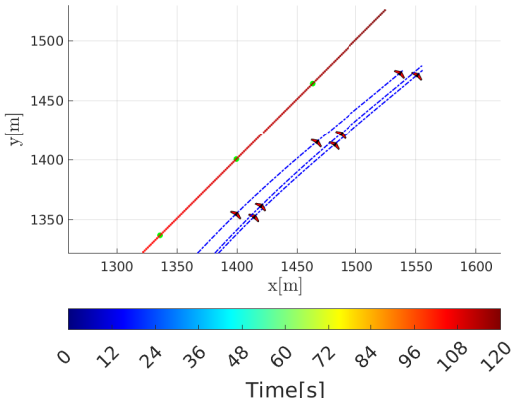

(b) Without wind compensation. Zoom in.

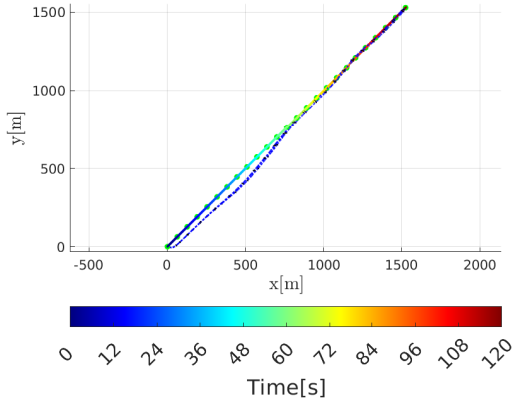

(c) With wind compensation.

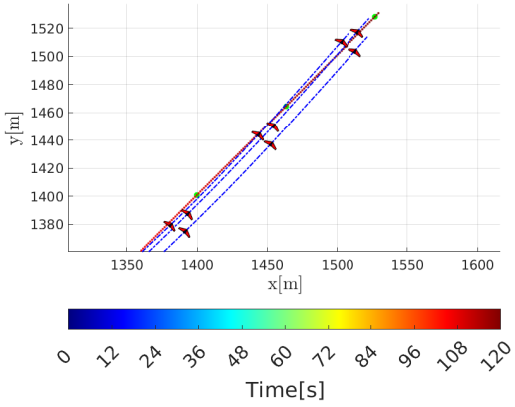

(d) With wind compensation. Zoom in.

Figure 6.27: The 3D visualization of the straight line trajectory of the three UAVs formation flight. The green dot represents the virtual leader and the red fixed-wing UAV represents the followers, which are plotted out each 5 seconds. The blue dot-dashed line represents the actual trajectories of the three followers.

doi:10.6342/NTU202500345

from Figure 6.22.

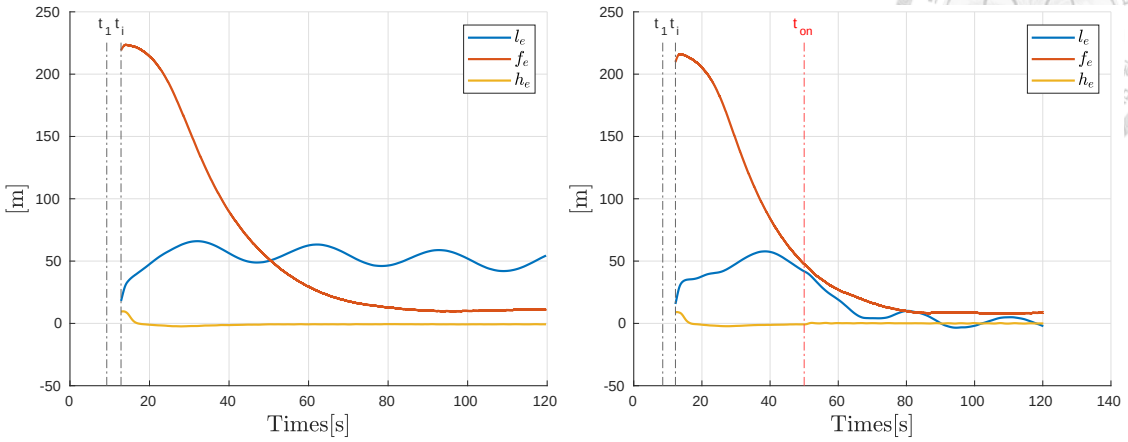

(a) Without wind compensation. **(b) With wind compensation.**

Figure 6.28: The formation error of the straight line formation flight. Only the F_1 is shown here.

6.3.2.2 Circular Orbit Trajectory

In the circular orbit formation flight, the virtual leader flies in a circular orbit trajectory with a radius of 400 m, the constant ground speed $V_g = 18$ m/s, and a constant altitude $z_L = -20$ m. The virtual leader's trajectory can be expressed as

$$\mathbf{p}_L(t) = \begin{bmatrix} 400\cos(\omega t) & 400\sin(\omega t) & -20 \end{bmatrix}^\top, \tag{6.12}$$

The formation trajectory of the three UAVs in the circular orbit formation flight is shown in Figure 6.31.

As compared to the straight line formation flight, both the l_e and f_e are reduced after the wind compensation as shown in Figure 6.32 because the variant flight direction along with the circular orbit cause the variant wind direction in the geometry frame $\{G\}$. The wind estimations are shown in Figure 6.33 and the states error are shown in Figure 6.34.

doi:10.6342/NTU202500345

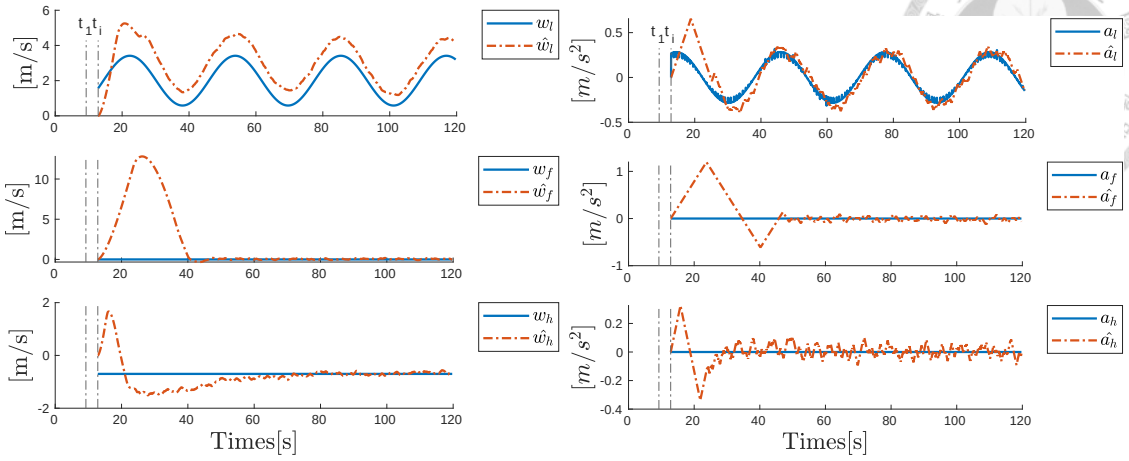

(a) Wind velocity estimation without wind compensation.

(b) Wind acceleration estimation without wind compensation.

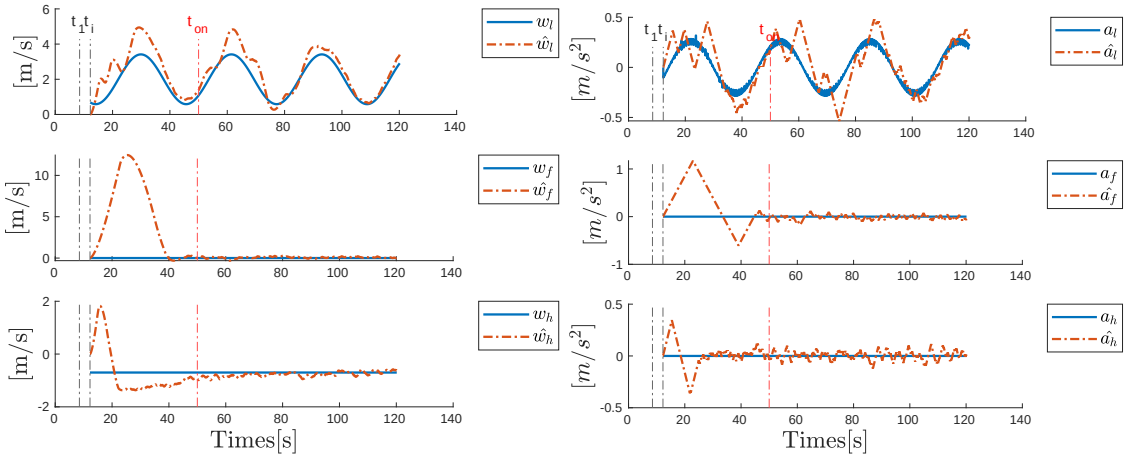

(c) Wind velocity estimation with wind compensation.

(d) Wind acceleration estimation with wind compensation.

Figure 6.29: The wind estimation of the straight line formation flight. Only the F_1 is shown here.

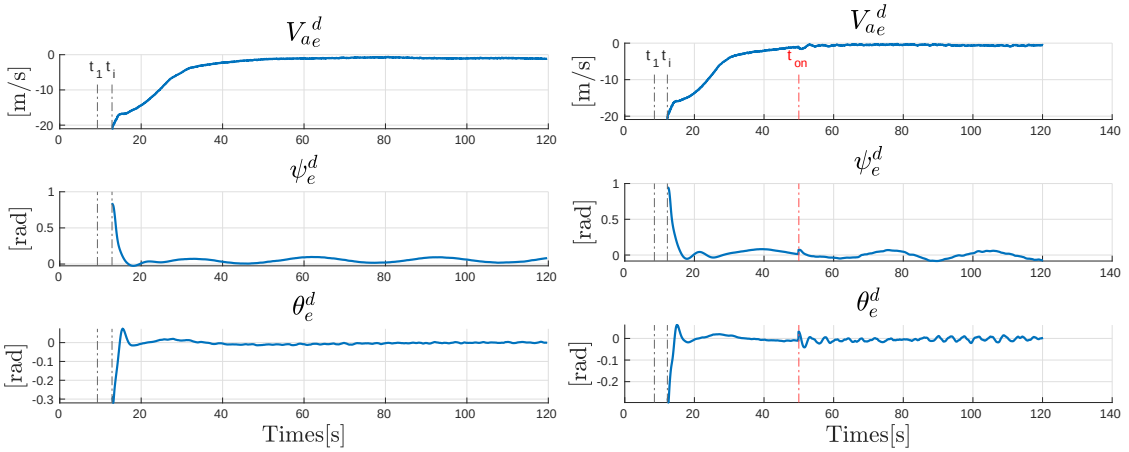

(a) The states error without wind compensation.

(b) The states error with wind compensation.

Figure 6.30: The states error of the straight line formation flight. Only the F_1 is shown here.

doi:10.6342/NTU202500345

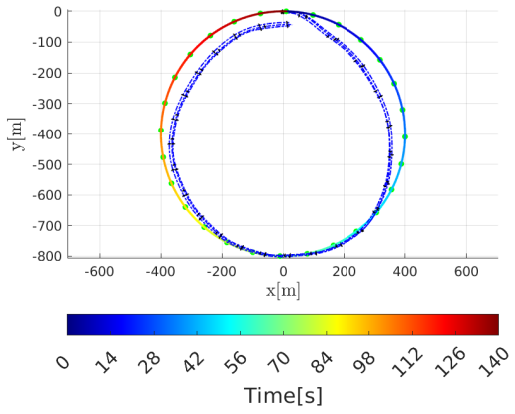

(a) Without wind compensation.

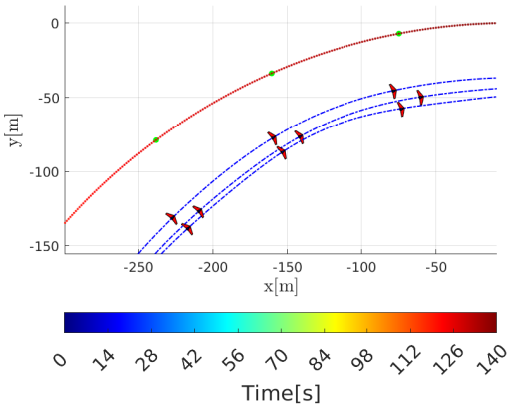

(b) Without wind compensation. Zoom in.

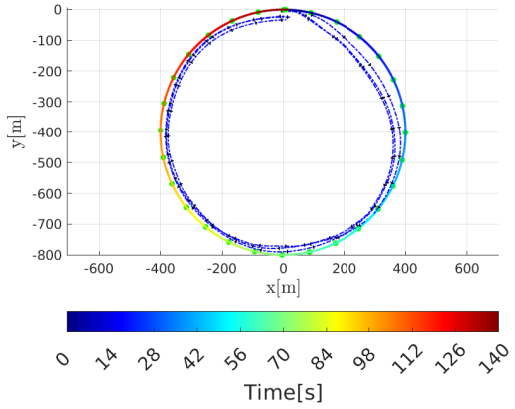

(c) With wind compensation.

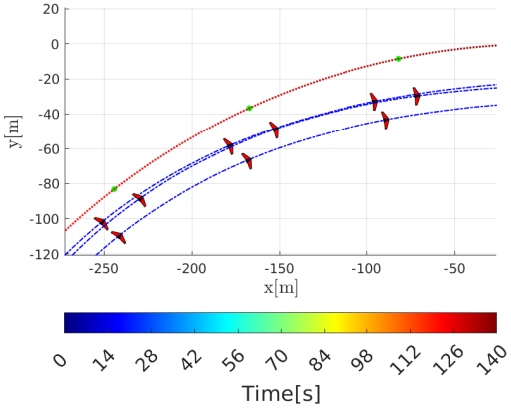

(d) With wind compensation. Zoom in.

Figure 6.31: The 3D visualization of the circular orbit trajectory of the three UAVs formation flight. The green dot represents the virtual leader and the red fixed-wing UAV represents the followers, which are plotted out each 5 seconds. The blue dot-dashed line represents the actual trajectories of the three followers.

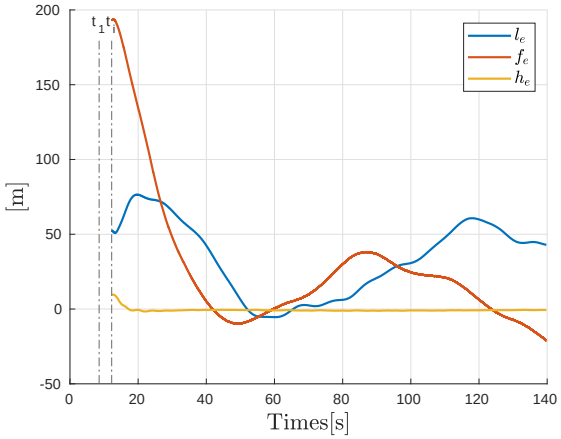

(a) Without wind compensation.

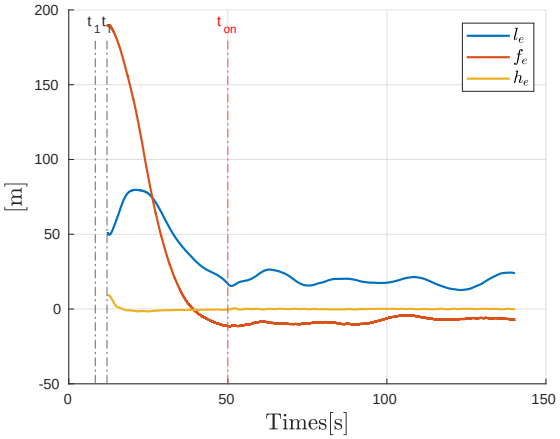

(b) With wind compensation.

Figure 6.32: The formation error of the circular orbit formation flight. Only the F_1 is shown here.

doi:10.6342/NTU202500345

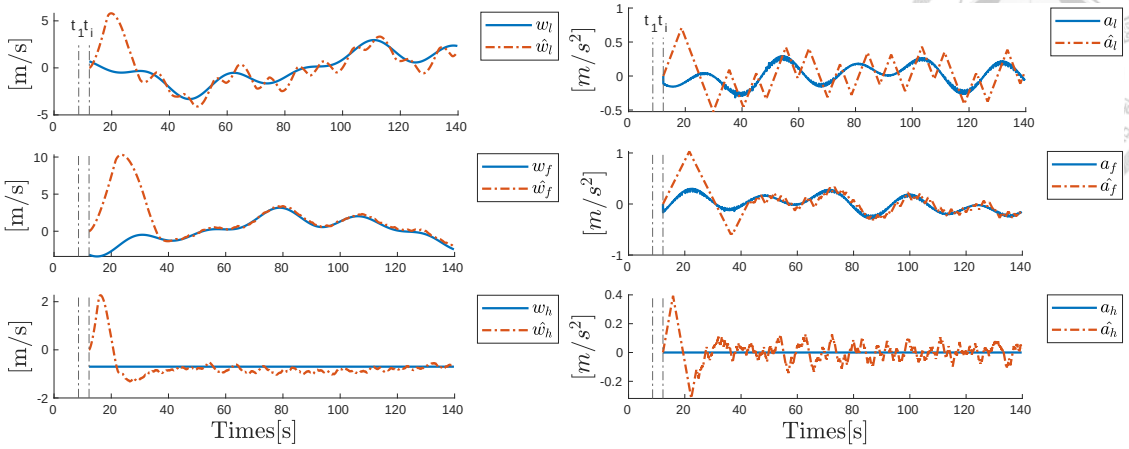

(a) Wind velocity estimation without wind compensation. **(b) Wind acceleration estimation without wind compensation.**

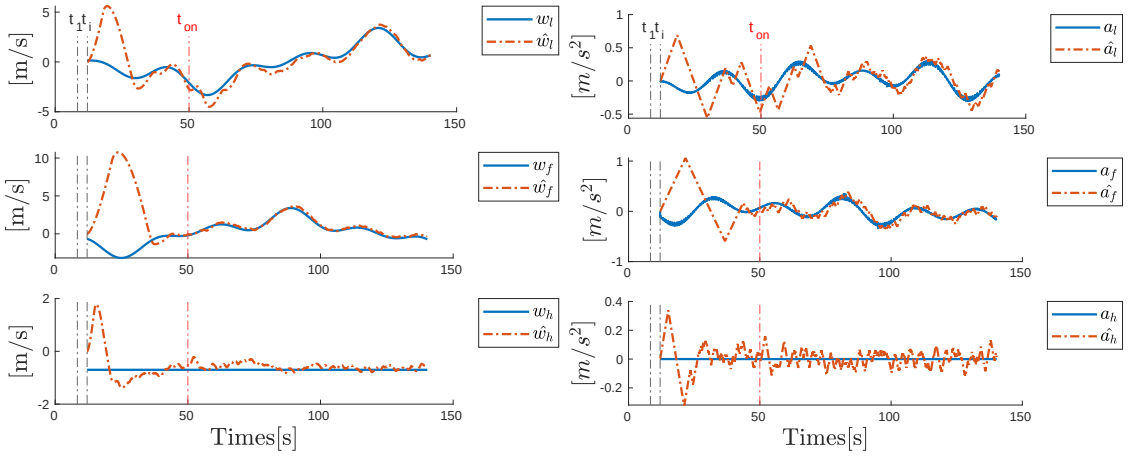

(c) Wind velocity estimation with wind compensation. **(d) Wind acceleration estimation with wind compensation.**

Figure 6.33: The wind estimation of the circular orbit formation flight. Only the F_1 is shown here.

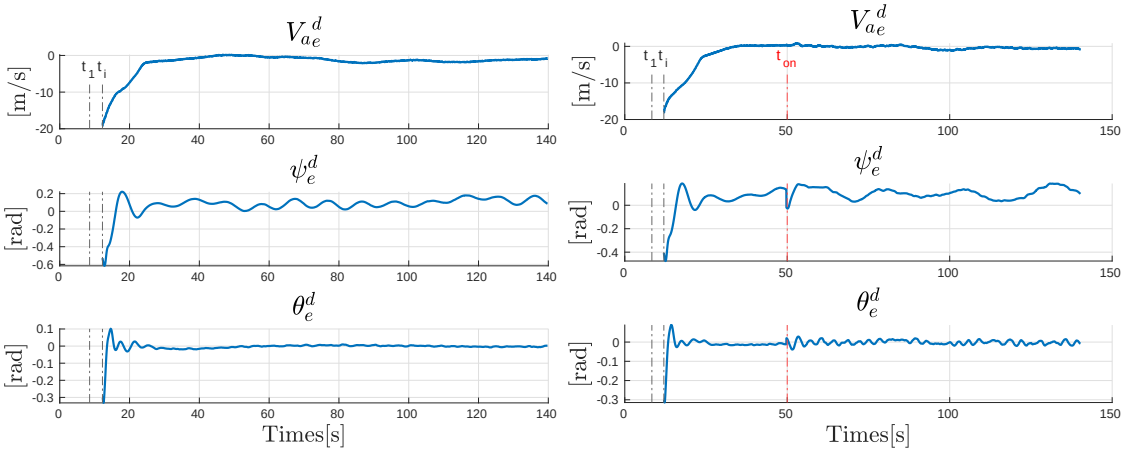

(a) The states error without wind compensation. **(b) The states error with wind compensation.**

Figure 6.34: The states error of the circular orbit formation flight. Only the F_1 is shown here.

doi:10.6342/NTU202500345

Chapter 7

Conclusions and Future Works

7.1 Conclusions

In this thesis, a Lyapunov-based foromation controller with sliding mode wind observer algorithm is proposed for the fixed-wing UAVs formation flight under the variant wind field environment. The proposed formation controller can not only handle the 2D formation flight but also the 3D formation flight. The proposed wind observer estimate the bounded variant wind velocity and acceleration in the geometry frame $\{G\}$, which make it easily be incorporated into the proposed formation controller.

On the other hand, the proposed algorithm are validated not only in the ideal MIL simulation but also in the more realistic SITL simulation provided by the off-the-shelf PX4 Autopilot. Although the proposed algorithm performs worse in the SITL simulation than in the MIL simulation due to the more realistic conditions such as the sensor noises, time delays, and the UAV model uncertainties. The simulation results still show that the formation error can be mitigated after the wind compensation. Besides, the success of the integration of the proposed algorithm into SITL simulation shows the potential of the proposed algorithm to be implemented in the real fixed-wing UAVs with the PX4 Autopilot and Pixhawk hardware [52: Pixhawk 2024] in the future.

7.2 Future Works

The proposed LBFC-SMWO algorithm can be further improved in the following aspects:

doi:10.6342/NTU202500345

- To apply the proposed algorithm in a close formation flight system to mitigate the energy consumption by utilizing the upwash effect from the leader UAV. The specific formation configuration [11: Mirzaeinia *et al.* 2019], [12: Zhang and Liu 2018] and the wake vortex from leader UAV should be considered.

- The inter-agent collision avoidance algorithm should be incorporated into the proposed algorithm to avoid the collision between the UAVs.

- The rigorous proof of the stability of the proposed LBFC and LBFC-SMWO algorithm should be conducted.

After the improvement of the proposed algorithm, the real flight test would be conducted to validate the proposed algorithm in the real fixed-wing UAVs.

doi:10.6342/NTU202500345

References

[1: Zhou *et al.* 2020]

Yongkun Zhou, Bin Rao, and Wei Wang, "UAV Swarm Intelligence: Recent Advances and Future Trends," *IEEE Access*, vol. 8, pp. 183 856–183 878, 2020, ISSN: 2169-3536. DOI: 10.1109/ACCESS.2020.3028865.

[2: Shakhatreh *et al.* 2019]

Hazim Shakhatreh, Ahmad H. Sawalmeh, Ala Al-Fuqaha, Zuochao Dou, Eyad Almaita, Issa Khalil, Noor Shamsiah Othman, Abdallah Khreishah, and Mohsen Guizani, "Unmanned Aerial Vehicles (UAVs): A Survey on Civil Applications and Key Research Challenges," *IEEE Access*, vol. 7, pp. 48 572–48 634, 2019, ISSN: 2169-3536. DOI: 10.1109/ACCESS.2019.2909530.

[3: Skydio 2024]

Skydio. "How Drones Are Used for Search and Rescue | Skydio." (2024), [Online]. Available: https://www.skydio.com/blog/how-to-use-drones-for-search-and-rescue/ (visited on 10/10/2024).

[4: Koetsier 2023]

John Koetsier. "Wing Drone Delivery in 2024: 'Capable Of Handling Tens Of Millions Of Deliveries For Millions Of Consumers'," Forbes. (2023), [Online]. Available: https://www.forbes.com/sites/johnkoetsier/2023/03/11/wing-drone-delivery-in-2024-capable-of-handling-tens-of-millions-of-deliveries-for-millions-of-consumers/ (visited on 10/10/2024).

[5: Zipline 2023]

Zipline. "FAA Clears Way for Autonomous Aviation in the U.S.; Unlocks Major Drone Delivery Expansion with Zipline Decision | Zipline Instant Delivery & Logistics," Zipline. (2023), [Online]. Available: https://www.flyzipline.com/newsroom/news/announcements/faa-authorizes-zipline-to-fly-bvlos (visited on 10/10/2024).

[6: Egypt 2023]

Daily News Egypt. "Amazon Prime Air to launch drone delivery in three new lo-

doi:10.6342/NTU202500345

cations," Dailynewsegypt. (Oct. 23, 2023), [Online]. Available: https://www.dailynewsegypt.com/2023/10/23/amazon-prime-air-to-launch-drone-delivery-in-three-new-locations/ (visited on 10/10/2024).

[7: MiTAC 2019]

MiTAC. "Coast guard using drones to monitor Taiwan's seas," 神通資訊科技股份有限公司. (Apr. 15, 2019), [Online]. Available: https://www.mitac.com.tw/en/coast-guard-using-drones-to-monitor-taiwans-seas/ (visited on 10/10/2024).

[8: 李文正 2024]

李文正. "陸 4 艘執法船出現了！海巡署曝「與國防部等友軍」有掌握：請漁民放心 - 社會," 李文正. (Feb. 19, 2024), [Online]. Available: https://www.chinatimes.com/realtimenews/20240219002829-260402?chdtv (visited on 10/10/2024).

[9: NAO 2023]

NAO. "NAO-112-12 海洋委員會海巡署旋翼型無人飛行載具試辦計畫執行情形專案審計報告," 中華民國審計部全球資訊網. (Dec. 15, 2023), [Online]. Available: https://www.audit.gov.tw (visited on 10/10/2024).

[10: Boon *et al.* 2017]

Marinus A. Boon, A. P. Drijfhout, and Solomon Tesfamichael, "COMPARISON OF A FIXED-WING AND MULTI-ROTOR UAV FOR ENVIRONMENTAL MAPPING APPLICATIONS: A CASE STUDY," *The International Archives of the Photogrammetry, Remote Sensing and Spatial Information Sciences*, vol. XLII-2/W6, pp. 47–54, Aug. 23, 2017, ISSN: 2194-9034. DOI: 10.5194/isprs-archives-XLII-2-W6-47-2017.

[11: Mirzaeinia *et al.* 2019]

Amir Mirzaeinia, Mostafa Hassanalian, Kooktae Lee, and Mehdi Mirzaeinia, "Energy conservation of V-shaped swarming fixed-wing drones through position reconfiguration," *Aerospace Science and Technology*, vol. 94, p. 105 398, Nov. 2019, ISSN: 12709638. DOI: 10.1016/j.ast.2019.105398.

doi:10.6342/NTU202500345

[12: Zhang and Liu 2018]

Qingrui Zhang and Hugh H.T. Liu, "Aerodynamic model-based robust adaptive control for close formation flight," *Aerospace Science and Technology*, vol. 79, pp. 5–16, Aug. 2018, ISSN: 12709638. DOI: 10.1016/j.ast.2018.05.029.

[13: Saeed *et al.* 2018]

Adnan S. Saeed, Ahmad Bani Younes, Chenxiao Cai, and Guowei Cai, "A survey of hybrid Unmanned Aerial Vehicles," *Progress in Aerospace Sciences*, vol. 98, pp. 91–105, Apr. 2018, ISSN: 03760421. DOI: 10.1016/j.paerosci.2018.03.007.

[14: Nelson *et al.* 2007]

Derek R. Nelson, D. Blake Barber, Timothy W. McLain, and Randal W. Beard, "Vector Field Path Following for Miniature Air Vehicles," *IEEE Transactions on Robotics*, vol. 23, no. 3, pp. 519–529, Jun. 2007, ISSN: 1552-3098. DOI: 10.1109/TRO.2007.898976.

[15: Anderson *et al.* 2005]

Erik P. Anderson, Randal W. Beard, and Timothy W. McLain, "Real-time dynamic trajectory smoothing for unmanned air vehicles," *IEEE Transactions on Control Systems Technology*, vol. 13, no. 3, pp. 471–477, May 2005, ISSN: 1558-0865. DOI: 10.1109/TCST.2004.839555.

[16: Beard and McLain 2012]

Randal W. Beard and Timothy W. McLain, *Small Unmanned Aircraft: Theory and Practice*. Princeton University Press, Feb. 26, 2012, ISBN: 978-1-4008-4060-1. DOI: 10.1515/9781400840601.

[17: Yu *et al.* 2018]

Wanming Yu, Defu Lin, and Tao Song, "Adaptive Control for UAV Close Formation Flight against Disturbances," in *2018 3rd International Conference on Robotics and Automation Engineering (ICRAE)*, Guangzhou: IEEE, Nov. 2018, pp. 196–201, ISBN: 978-1-5386-9594-4. DOI: 10.1109/ICRAE.2018.8586779.

doi:10.6342/NTU202500345

[18: Zhang *et al.* 2021]

Jialong Zhang, Pu Zhang, and Jianguo Yan, "Distributed Adaptive Finite-Time Compensation Control for UAV Swarm With Uncertain Disturbances," *IEEE Transactions on Circuits and Systems I: Regular Papers*, vol. 68, no. 2, pp. 829–841, Feb. 2021, ISSN: 1549-8328, 1558-0806. DOI: 10.1109/TCSI.2020.3034979.

[19: Meier *et al.* 2015]

Lorenz Meier, Dominik Honegger, and Marc Pollefeys, "PX4: A node-based multithreaded open source robotics framework for deeply embedded platforms," in *2015 IEEE International Conference on Robotics and Automation (ICRA)*, Seattle, WA, USA: IEEE, May 2015, pp. 6235–6240, ISBN: 978-1-4799-6923-4. DOI: 10.1109/ICRA.2015.7140074.

[20: Yang *et al.* 2021]

Jun Yang, Cunjia Liu, Matthew Coombes, Yunda Yan, and Wen-Hua Chen, "Optimal Path Following for Small Fixed-Wing UAVs Under Wind Disturbances," *IEEE Transactions on Control Systems Technology*, vol. 29, no. 3, pp. 996–1008, May 2021, ISSN: 1063-6536, 1558-0865, 2374-0159. DOI: 10.1109/TCST.2020.2980727.

[21: Shtessel *et al.* 2014]

Yuri Shtessel, Christopher Edwards, Leonid Fridman, and Arie Levant, *Sliding Mode Control and Observation* (Control Engineering). New York, NY: Springer New York, 2014, ISBN: 978-0-8176-4892-3 978-0-8176-4893-0. DOI: 10.1007/978-0-8176-4893-0.

[22: Ouyang *et al.* 2023]

Quan Ouyang, Zhaoxiang Wu, Yuhua Cong, and Zhisheng Wang, "Formation control of unmanned aerial vehicle swarms: A comprehensive review," *Asian Journal of Control*, vol. 25, no. 1, pp. 570–593, Jan. 2023, ISSN: 1561-8625, 1934-6093. DOI: 10.1002/asjc.2806.

[23: Do *et al.* 2021]

Hai Do, Hoang Hua, Minh Nguyen, Cuong Nguyen, Hoa Nguyen, Hoa Nguyen,

doi:10.6342/NTU202500345

and Nga Nguyen, "Formation Control Algorithms for Multiple-UAVs: A Comprehensive Survey," *EAI Endorsed Transactions on Industrial Networks and Intelligent Systems*, vol. 8, no. 27, p. 170 230, Jun. 23, 2021, ISSN: 2410-0218. DOI: 10.4108/eai.10-6-2021.170230.

[24: Liu *et al.* 2015]

Zhixiang Liu, Xiang Yu, Chi Yuan, and Youmin Zhang, "Leader-follower formation control of unmanned aerial vehicles with fault tolerant and collision avoidance capabilities," in *2015 International Conference on Unmanned Aircraft Systems (ICUAS)*, Denver, CO, USA: IEEE, Jun. 2015, pp. 1025–1030, ISBN: 978-1-4799-6010-1. DOI: 10.1109/ICUAS.2015.7152392.

[25: Gu *et al.* 2006]

Yu Gu, Brad Seanor, Giampiero Campa, Marcello R. Napolitano, Larry Rowe, Srikanth Gururajan, and Sheng Wan, "Design and Flight Testing Evaluation of Formation Control Laws," *IEEE Transactions on Control Systems Technology*, vol. 14, no. 6, pp. 1105–1112, Nov. 2006, ISSN: 1063-6536. DOI: 10.1109/TCST.2006.880203.

[26: Zhang and Liu 2019]

Qingrui Zhang and Hugh H. T. Liu. "Robust Cooperative Formation Control of Fixed-Wing Unmanned Aerial Vehicles." arXiv: 1905.01028 [cs]. (May 6, 2019), [Online]. Available: http://arxiv.org/abs/1905.01028 (visited on 09/08/2024), pre-published.

[27: Kuriki and Namerikawa 2013]

Yasuhiro Kuriki and Toru Namerikawa, "Control of Formation Configuration Using Leader-Follower Structure," *Journal of System Design and Dynamics*, vol. 7, no. 3, pp. 254–264, 2013, ISSN: 1881-3046. DOI: 10.1299/jsdd.7.254.

[28: Zhi *et al.* 2022]

Yongran Zhi, Lei Liu, Bin Guan, Bo Wang, Zhongtao Cheng, and Huijin Fan, "Distributed robust adaptive formation control of fixed-wing UAVs with unknown un-

doi:10.6342/NTU202500345

certainties and disturbances," *Aerospace Science and Technology*, vol. 126, p. 107 600, Jul. 2022, ISSN: 12709638. DOI: 10.1016/j.ast.2022.107600.

[29: Bautista and De Marina 2024]

Jesús Bautista and Héctor García De Marina, "Behavioral-based circular formation control for robot swarms," in *2024 IEEE International Conference on Robotics and Automation (ICRA)*, Yokohama, Japan: IEEE, May 13, 2024, pp. 8989–8995, ISBN: 9798350384574. DOI: 10.1109/ICRA57147.2024.10610826.

[30: Wang *et al.* 2023]

Ximan Wang, Simone Baldi, Xuewei Feng, Changwei Wu, Hongwei Xie, and Bart De Schutter, "A Fixed-Wing UAV Formation Algorithm Based on Vector Field Guidance," *IEEE Transactions on Automation Science and Engineering*, vol. 20, no. 1, pp. 179–192, Jan. 2023, ISSN: 1545-5955, 1558-3783. DOI: 10.1109/TASE.2022.3144672.

[31: Wilson *et al.* 2014]

Daniel B. Wilson, Ali H. Goktogan, and Salah Sukkarieh, "A vision based relative navigation framework for formation flight," in *2014 IEEE International Conference on Robotics and Automation (ICRA)*, Hong Kong, China: IEEE, May 2014, pp. 4988–4995, ISBN: 978-1-4799-3685-4. DOI: 10.1109/ICRA.2014.6907590.

[32: Tian *et al.* 2021]

Pengzhi Tian, Haiyang Chao, Matthew Rhudy, Jason Gross, and Huixuan Wu, "Wind sensing and estimation using small fixed-wing unmanned aerial vehicles: A survey," *Journal of Aerospace Information Systems*, vol. 18, no. 3, pp. 132–143, 2021, ISSN: 1542-9423. DOI: 10.2514/1.I010885.

[33: Ardupilot 2024]

Ardupilot. "Windspeed Estimation and Baro Compensation —Copter documentation." (2024), [Online]. Available: https://ardupilot.org/copter/docs/airspeed-estimation.html (visited on 10/10/2024).

[34: PX4 2019]

PX4. "Using the ECL EKF | PX4 Guide (main)." (2019), [Online]. Available: https:

doi:10.6342/NTU202500345

//docs.px4.io/main/en/advanced_config/tuning_the_ecl_ekf.html#what-are-the-advantages-and-disadvantages-of-the-ecl-ekf-over-other-estimators (visited on 10/10/2024).

[35: AviationHunt 2024]

AviationHunt. "Different Types of Airspeed: IAS, TAS, CAS, EAS, GS - AviationHunt." (Oct. 23, 2024), [Online]. Available: https://www.aviationhunt.com/types-of-airspeed/ (visited on 12/18/2024).

[36: Beard 2024]

Randal W. Beard, *Byu-magicc/mavsim_public*, Nov. 8, 2024. [Online]. Available: https://github.com/byu-magicc/mavsim_public (visited on 11/09/2024).

[37: MAFarooqi 2022]

NCS - 25a - Relative degree, MAFarooqi, director, Nov. 3, 2022. [Online]. Available: https://www.youtube.com/watch?v=0xXMuavWFsI (visited on 11/10/2024).

[38: Khalil 2002]

Hassan K. Khalil, *Nonlinear Systems*, 3rd ed. Upper Saddle River, N.J: Prentice Hall, 2002, 750 pp., ISBN: 978-0-13-067389-3.

[39: Filippov 1988]

Aleksei F. Filippov, *Differential Equations with Discontinuous Righthand Sides* (Mathematics and Its Applications), Felix M. Arscott, Ed., red. by M. Hazewinkel. Dordrecht: Springer Netherlands, 1988, vol. 18, ISBN: 978-90-481-8449-1 978-94-015-7793-9. DOI: 10.1007/978-94-015-7793-9.

[40: MAFarooqi 2023]

NCS - 34a - Sliding Mode Control - Basic Concept, MAFarooqi, director, Dec. 1, 2023. [Online]. Available: https://www.youtube.com/watch?v=AQ9BJEJ8nKw (visited on 12/19/2024).

[41: Perruquetti 2010]

W Perruquetti, "From 1rst order to Higher order Sliding modes," Sep. 2010.

doi:10.6342/NTU202500345

[42: Dorf and Bishop 2017]

Richard C. Dorf and Robert H. Bishop, *Modern Control Systems*, Thirteenth edition, global edition. Harlow, England London New York Boston San Francisco Toronto Sydney Dubai Singapore Hong Kong Tokyo Seoul Taipei New Delhi Cape Town São Paulo Mexico City Madrid Amsterdam Munich Paris Milan: Pearson, 2017, 1025 pp., ISBN: 978-0-13-440762-3 978-1-292-15297-4.

[43: GazeboSimulation 2024]

GazeboSimulation. "Gazebo Simulation | PX4 Guide (main)." (2024), [Online]. Available: https://docs.px4.io/main/en/sim_gazebo_gz/ (visited on 11/30/2024).

[44: Autopilot 2024]

PX4 Autopilot, *PX4/PX4-Autopilot*, Nov. 30, 2024. [Online]. Available: https://github.com/PX4/PX4-Autopilot (visited on 11/30/2024).

[45: GazeboGarden 2024]

GazeboGarden. "Getting Started with Gazebo? —Gazebo garden documentation." (2024), [Online]. Available: https://gazebosim.org/docs/garden/getstarted/# (visited on 11/23/2024).

[46: QGC 2024]

QGC. "QGroundControl User Guide | QGC Guide (master)." (2024), [Online]. Available: https://docs.qgroundcontrol.com/master/en/qgc-user-guide/index.html (visited on 11/30/2024).

[47: Wikipedia 2024]

Wikipedia, *Pitot tube*, in *Wikipedia*, Sep. 23, 2024.

[48: Gazebosim 2024]

Gazebosim. "Gazebosim/gz-sim: Open source robotics simulator. The latest version of Gazebo." (2024), [Online]. Available: https://github.com/gazebosim/gz-sim/tree/gz-sim9 (visited on 11/30/2024).

[49: ROS2 2024]

ROS2. "ROS 2 Documentation —ROS 2 Documentation: Humble documentation."

doi:10.6342/NTU202500345

(2024), [Online]. Available: https://docs.ros.org/en/humble/index.html (visited on 11/30/2024).

[50: GazeboVehicles 2024]

GazeboVehicles. "Gazebo Vehicles | PX4 User Guide (main)." (2024), [Online]. Available: https://docs.px4.io/main/en/sim_gazebo_gz/vehicles.html (visited on 12/14/2024).

[51: MathWorks 2022]

MathWorks, "Estimate transfer function model documentation," 2022. [Online]. Available: https://www.mathworks.com/help/ident/ref/tfest.html (visited on 12/23/2024).

[52: Pixhawk 2024]

Pixhawk. "Pixhawk Standard Autopilots | PX4 Guide (main)." (2024), [Online]. Available: https://docs.px4.io/main/en/flight_controller/autopilot_pixhawk_standard.html (visited on 12/19/2024).

doi:10.6342/NTU202500345